UiT The Arctic University of Norway

Faculty of science and technology

Department of geosciences

Morphology and structural, stratigraphic setting of volcanic deposits at Skoll high on the Vøring Plateau

Rasmus Andersen

Geo 3900 - Master thesis in geology May 2024

Photo Courtesy of the United States Geological Survey

Abstract

The voluminous igneous complexes that are present in the sedimentary basins of the volcanic rifted Vøring Margin have recently gained attention due to their promising potential for carbon sequestration. Although there have been major improvements in the field of intra- and subbasalt imaging and subbasalt sequences over the past decade, (Planke et al., 2017) the emplacement mechanism, stratigraphical setting, structural setting and postdepositional deformation of these are not fully understood. The work of this thesis has utilized high resolution 3D seismic data, 2D seismic data, and well data to study the volcanic deposits at Skoll High on the outer Vøring Margin with regards to their origin, emplacement, and post-depositional deformation.

The results include interpretation of Seaward Dipping Reflectors (SDR's), landwards flows, lava delta, inner flows, pseudocraters, fissures, subaerial drainage channels, gas or fluid migration structures, bench collapse, and lava delta collapse. Several of these interpretations have been compared to similar field examples from around the world.

From these interpretations as well as previous studies, a geological model is proposed, comprising 4 stages: 1 Uplift, intrusions, sill emplacement, and the creation of the Vøring escarpment due to rifting, 2 emplacement of SDR's, landwards flows, inner flows, and the creation of a lava delta, 3 regression, collapse of lava delta, and pseudocrater formation due to mixing of surface water and lava flows, 4 trangression, erosion of the high, and formation of a widespread drainage network.

The storage potential for CO2 sequestration at Skoll High has been calculated as 67,5 Gt worth of CO2, but due to the nature of this calculation, it might only be used as a preliminary estimate. More knowledge about how CO2 behaves when injected into basalts, and further data offering insight into the 3D structure of the basalt sequences is needed to improve this estimate.

Acknowledgements

A wonderful period of studying in Tromsø is coming to an end and before it’s all over, an expression of gratitude for the people that have had an impact on the completion of my thesis must be given. First, I will have to thank my main supervisor, Professor Stefan Büntz for his invaluable advice from start to finish. Your door was always open for questions, and you were always eager to help, which just goes to show that you really care. For that I am very thankful, and it has motivated me and helped me to push forward. Also, a great many thanks to my co-supervisor Associate Professor Andreia Plaza-Faverola. Your critical questions and creative ideas have helped me to reflect and find perspectives, that I would have never thought of otherwise. Also, the Department of Geoscience acknowledges the Norwegian repository for petroleum data for access to 3D seismic data cube CVX1101.

A very profound thanks to all the people from the office: Thanks to Georgia-Marie, Anniken, Teitur, Isaiah and Iver for popping by to “bother” me for a while, thanks to Vilde and Luke for making me laugh till my stomach hurts, thanks to the rest of the gang for wonderfully distracting breaks, and especially thanks to Teitur for many interesting and fruitful discussions, as well as a wholesome time in (and outside) the office together.

A thanks must also go to the great people of TSI Ultimate for being amazing individuals and keeping me sane in the darks months of winter.

Gratitude also goes to my friends Sofie and Frederik, for regular conversations that has given me piece of mind, and helped me tackle life in general.

The last thanks goes to my family for showing interest and support, and also for a giving me a firm and reliable foundation, that has made it possible for me to study a master degree here in the first place.

Table of Contents

1 Introduction

The goal of this thesis is to use 3D seismic data and borehole logs to study and interpret the volcanic deposits in the outer Vøring Margin at the Skoll High. The basalt sequences and structures therein will be imaged and compared with contemporary volcanic structures, to give a better understanding of the geological development of the Norwegian margin. Furthermore, the potential storage of CO_2 in the basalts at Skoll High will be assessed.
The Vøring Margin has been thoroughly studied for the last 50 years due to its prospectivity, and because it is a classic example of a volcanic rifted margin (Ottesen et al., 2009, Planke et al., 2021 a). It is showing wedges of Seaward Dipping Reflectors (SDR's), intrusions of high velocity (>7km/s) lower crustal bodies and massive sill and dyke intrusive complexes along with intrusions in the middle and upper continental crust, making up the plumbing system of the North Atlantic Igneous Province (NAIP) (Planke et al., 2000, Abdelamak et al., 2016, Zastrozhnov et al., 2020). The NAIP has a volume estimated to be $6 - 10 \cdot 10^6\ km^3$, covering an area of $1{,}3 \cdot 10^6\ km^2$ approximately equivalent to five times the size of the UK (Walker et al., 2022). The NAIP is a specific example of the broader term: Large Igneous Province (LIP) and the NAIP is one of the best studied LIPs in the world because it is a natural laboratory for investigating volcanic margin formation, breakup-processes, tectonomagmatic processes and the rift to drift transition (Mjelde et al., 2003, Ren et al., 2003, Zastrozhnov et al., 2018, Walker et al., 2022). One of the major issues has been to image beneath the massive basalt flows on the outer Vøring Margin. Our understanding has therefore improved significantly with the International Ocean Discovery Program (IODP), Ocean Drilling Project (ODP), Deep Sea Drilling Project (DSDP), and with the improvement of the multichannel seismic data, both in terms of processing and acquisition technologies. (Ren et al., 2003, Planke et al., 2017, Planke et al., 2021 a).
Despite this, there is still a lot of knowledge to be gained from the igneous segments on the Skoll High. They were emplaced as part of the breakup associated with the formation of the Atlantic Sea about 56 million years ago (Skogseid et al., 1992), and the flows have a length of up to 100 km (Zastrozhnov et al., 2020). They overstepped the Vøring Escarpment and formed a lava delta as they reached into the sea (see Figure 1.1).
LIP's are on the scale of hundreds of kilometers, and the seismic facies observed on the Norwegian Margin is on the scale of tens of kilometers, but if one starts looking on the scale

of kilometres and beneath, structures related to lava emplacement can be found, which might improve the current knowledge of how the igneous part of the Vøring Margin developed (Single & Jerram 2004). These structures could be lava flows, different lava flow surface morphologies, sills, hydrothermal vent complexes, and these have previously been identified by authors correlating the offshore observations with well-known onshore examples (Jerram et al., 2009, Nelson et al., 2009a, Nelson et al., 2009b, Angkasa et al., 2017, Planke et al., 2017). Known examples come in abundance as the emplacement of lavas is a well-studied phenomenon (Hon et al., 1994, Single & Jerram 2004, Ball et al., 2008, Hamilton et al., 2010, Millet et al., 2016, Gregg, 2017). Due to the vastness of this field, the topics presented here will be restricted to the features that are relevant due to their recognizability on the seismic data, such as lava flow characteristics, compression ridges, pseudocraters, tumuli and inflated lava lobes.

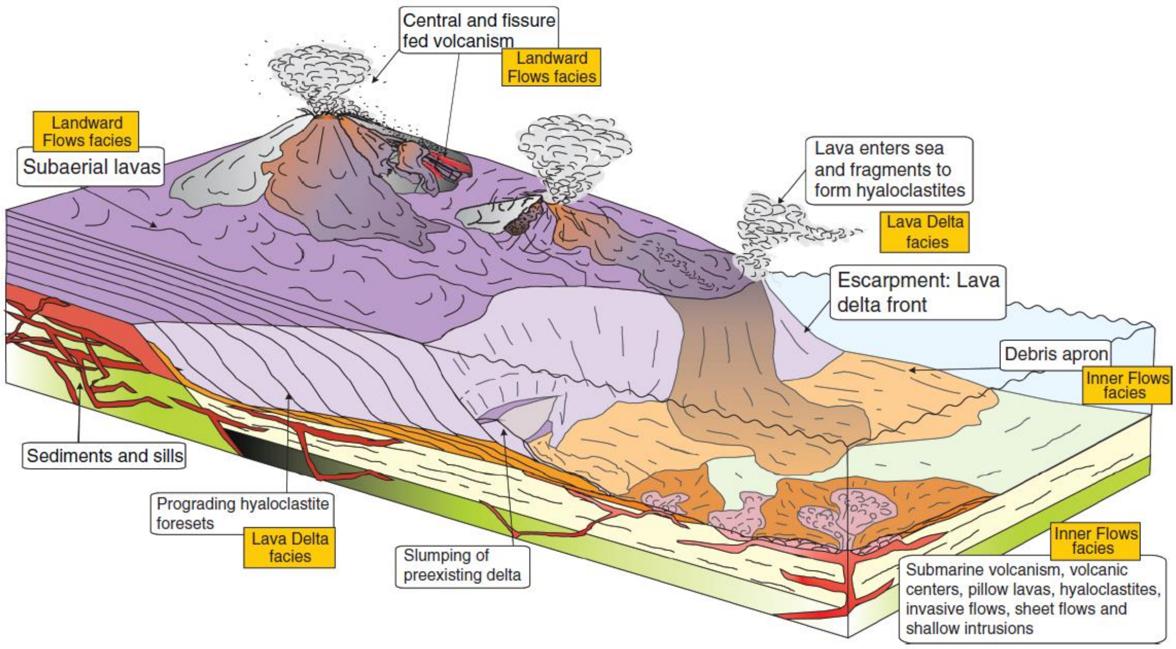

Figure 1.1. Conceptual model of Skoll High and the area southeast of the Vøring Escarpment (see Figure 2.1). From Planke et al., 2017.

During the many years of research on the Vøring Margin, there has been several topics leading to disagreements between authors. A major topic of discussion has been the origin and primary driver for the break-up, and this is linked with the interpretation of the lower crustal high velocity bodies. LIP’s have been suggested to be initiated by meteor impacts, mantle plumes and various lithosphere-controlled processes and specifically the excess magmatism on the NAIP has been suggested to originate from small scale convection at the

base of the lithosphere or mantle source heterogeneity (Mutter et al., 1988, Jones et al., 2002, Foulger et al., 2020, Lu & Huismans 2021, Planke et al., 2021 a)
Specifically connected to the period of break-up, there has been some contention as to whether the margin should be characterized as an Iberian-type magma poor margin, or as a volcanic rifted margin (Ren et al., 1998, Peron-Pinvidic & Osmundsen 2018, Gernigon et al., 2015, Zastrozhnov et al., 2018). There is today a consensus that the North Atlantic Igneous Province originates from a plume, and that the Norwegian Margin is a volcanic passive margin, but the full picture is still a bit blurry (Zastrozhnov et al., 2020). Especially with regards to the formation, emplacement, and environmental impact of the breakup volcanism. It is known that LIP formation has an impact on the climate, and that there is a certain correlation between LIP's, mass extinctions, and global warming, but the exact effects and details about this correlation is still unknown (Jones et al., 2016, Planke et al., 2021a).
On this note, the IPCC rapport from 2018 (IPCC, 2018) clearly states that if we are to avoid irreversible and self-accelerating positive feedback mechanisms with regard to the climate, we have to stay below an increase of 2°C and preferably 1,5°C before 2100. To do this we not only have to reduce emissions significantly, but we also must capture some of the carbon already emitted. More specifically we need to remove 10Gt/year by 2050 and 20 Gt/year by 2100, and CO2 capture and storage (CCS) is a very useful and relevant tool in reaching this goal. The injection has already been going on in saline aquifers since 1996 (Sleipner CCS Project) in Norway, but the rate of injection is on the tens of Mt/year scale, which is insignificant compared to the 40Gt/year that we emit worldwide (Kelemen et al., 2019).
A contributing solution to the traditional CO2 storage could be CO2 injection into basalts. It is a readily and widespread resource, and it has proved to be a feasible method that mineralizes CO2 rapidly (in a few years), which makes it a relatively safe storage option (Oelkers et al., 2008, Gislason & Oelkers, 2014). Worldwide mid-oceanic ridge basalt has an enormous storage potential (Snæbjørnsdottir et al., 2014), but in recent times the Norwegian volcanic rifted margin has attracted attention in this regard (Planke et al.,2021a, Planke et al., 2021b).

1.1 CO2 Storage

Sequestration of CO2 into basalts has proven to be a feasible method by pilot projects in Iceland and Wallula, USA (Matter et al., 2011, McGrail et al., 2011). What is special about this method is the rate of mineralization of the injected CO2. When injecting CO2 by conventional methods, it takes thousands of years before it is mineralized and thereby safely stored (Gislason & Oelkers, 2014, Matter et al., 2016). When the CO2 is injected into basalts, it mineralizes in a few years, because it is reacting with Mg, Ca, and Fe to form magnesite, carbonate, and siderite (Oelkers et al., 2008).

When storing CO2 this way, there are several key parameters to consider, described by Snæbjornsdottir et al., 2014. The most obvious is the availability of Mg, Ca, and Fe and a high reaction rate with the CO2. The availability of these minerals is ensured by injecting into basalt, and the reaction rate is enhanced by high mineral-fluid interfacial surface area, permeability, porosity, CO2 partial pressure, and temperature. There is, however, an upper limit in temperature at about 300 °C, because the stability of carbonate minerals decreases above this temperature, meaning that the maximum depth is often determined by the geothermal gradient. Porosity and permeability decrease with increasing age, burial, and alteration. If following the example of the CarbFix project in Iceland, high amounts of water are needed to dissolve the CO2 during injection. This makes the CO2 lose its buoyancy and increases the reaction rate with the basalt. In Iceland they needed 22 times as much water as CO2 for the injection (Matter et al., 2011), but the high water-demand should not be an issue when injecting in the ocean. This method needs a pressure of 25 bars to dissolve the CO2 during injection, so the minimum depth is some 350 m under the water table, but this is also not a problem when injecting offshore. The main target when injecting into basalts is the flow tops, because this is usually where the best porosity and permeability is found.

Recent studies have investigated the possibility of sequestrating CO2 in the volcanic units on the NAIP and found that it could be a feasible option in the future (Planke et al., 2021c, Rosenqvist et al., 2023). McGrail et al., 2006 proposed that a porosity of 15% and a thickness over 10 m is needed for injection into basalts. In the ODP 642E on the Vøring Margin, there was found 122 lava flows down to ca. 900 m with unclogged vesicular flow crusts, and an aquifer of 100 m thickness within the basalt sequence (Planke, 1994). Rosenqvist et al., 2023 used the Faroe Islands Basalt Group as an analogue for the conditions in the offshore part of the NAIP and found that there are occurrences of flow crust with little to no secondary mineralization in the pores. The porosity is varying a lot (from <1% to 45%) as is the permeability (from negligible to 88 D), both depending on the degree of alteration and secondary mineralization.

1.2 Volcanic emplacement and structures

There are many parameters deciding how a basaltic lava flow behaves, like effusion rate, temperature, cooling rate, crystal content, underlying topography, viscosity, vesicle distribution, and gas content, but the simplest description would be whether it is a pahoehoe or ‘a’ā flow. These terms are defined in Hawaii, which means that it can sometimes be hard to determine flows elsewhere, as these types are relative and dependent on the specific location, but some general characteristics can be drawn up. Pahoehoe lava has a low viscosity, low shear rate, and forms a smooth continuous crust. Typical features are pipe-like vesicles along the base, a massive interior zone, and a vesicular or glassy crust (Walker, 1971). Pahoehoe flows can form channels and tubes but are commonly observed to propagate as lobes (Gregg, 2017).

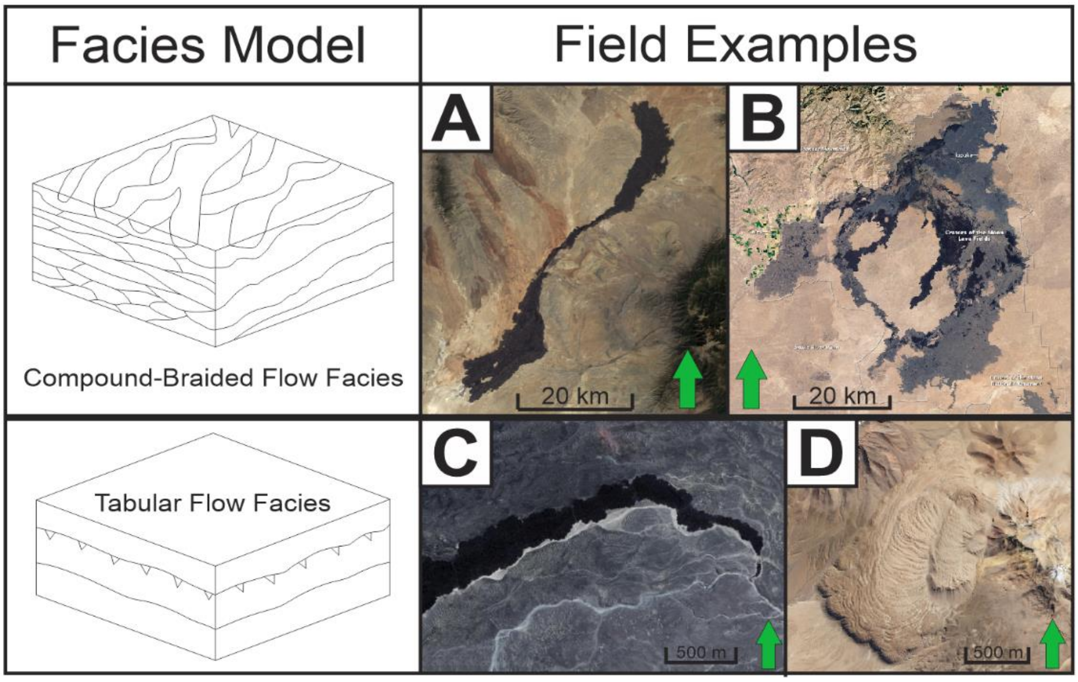

Figure 1.2. Model and field examples of compound-braided and tabular flow facies. The figure is redrawn and modified from Nelson et al., 2009a. A show the Carrizozo lava flow and the picture can be found at https://earthobservatory.nasa.gov/images/39550/carrizozo-lava-flow (accessed march 2024) and is from Google Earth. B shows the Craters of the Moon Lava Fields and the picture is from https://www.usgs.gov/media/images/young-lava-flow-craters-moon-national-monument (accessed march 2024) with courtesy of the U.S. Geological Survey/photo by Robert Simmon. C shows a flow from Harrat Khaybar Volcanic Field and picture is from Nemeth & Moufti 2023. D shows the Chao dacite from the Altiplano-Puna Volcanic Complex and the picture is from https://earthobservatory.nasa.gov/images/82424/the-shapes-that-lavas-take-part-1 (accessed march 2024) with courtesy of the NASA Earth Observatory/photo by Robert Simmon.

As a lobe propagates, it will form enough crust to retain the lobe.From this point the lobe will start to inflate and at a certain point, a new lobe will extrude from the old lobe. Inflation is a very important factor for the reach of pahoehoe flows, as the inflated flows tend to lose less heat than flows fed by tubes or channels. (Hon et al., 1994).

‘A’ā flows have a high viscosity, high shear rate, and tend to form spiny, rubbly crust. This is because the higher shear rate is tearing the crust apart, creating clinkers or chunks of broken crust on top of the flow.
As the flow is advancing, these fragments will fall off on the front of the flow and be incorporated in the bottom of the flow. The resulting unit is a massive interior sandwiched between a rubbly top and bottom. A flow generally starts as a pahoehoe flow with a smooth hummocky surface, showing tumuli, pressure ridges, and ropy structures. Tumuli and pressure ridges are created by the same mechanisms as inflation, only on a smaller scale. Small topographic obstacles or solidification of the crust will retard the flow, causing the lava to flow vertically rather than horizontally (Gregg, 2017).
A morphology that is a consequence of this inflation is the lava rise pits observed by Walker, 1991 on the coastal flats of Kilauea. They found that these pits are formed, because a small section of the lava surface failed to elevate with the rest of the flow. This could happen if a flow did not cover an area due to a higher topography or simply due to holes in between flows. Lava rise pits are similar to tumuli in size and occurrence and they usually show a widening downwards with an overhang at the top. Since they form by inflation of the surrounding lava, their depth would be the same as the flow thickness (Hon et al., 1994)
Another phenomenon that might create pits on a lava flow surface is rootless cones, that has been observed all over the world and on Mars (Hamilton et al., 2010, Reynolds et al., 2015, Noguchi et al., 2016). They are also known as pseudocraters or littoral cones in the literature, and they form from explosive lava-water interactions. When lava flows over an area with water-saturated sediments, it creates explosive activity. These explosions eject clasts of lava and sediment, which is deposited as pyroclastic density currents radially on the active lava flow, leaving behind a hole. After these initial deposits lava will well up from the hole for hours to days building the cone-shape that can be observed post formation. The cones can be from 2-40 m in height and 5-450 m in bottom diameter (Fagents & Thordarsson, 2007).

The effusion rate also has an important effect on the morphology of the resulting lava flow. A high effusion rate will tend to form simple sheet/tabular flows, and a low effusion rate will tend to form compound braided flows (Walker, 1971, Hallworth et al., 1987, Figure 1.2). Pahoehoe flows is often of the compound braided type, and ‘a’ā flows often show features of the simple sheet/tabular type. Compound braided flows are divisible into minor flow units and are formed when the flow is repeatedly halting until the next outbreak through the solidifying temporary lava front. This makes them able to go very far as can be seen on the scales in Figure 1.2. Simple sheet/tabular flows show, as the name suggests, simple laminar units on top of each other, and it is formed when the lava propagates as a single continuous flow. They tend to show lobate crenulated margins as seen in Figure 1.2 (Walker, 1971, Hon et al., 1994, Single & Jerram, 2004). Another important factor to determine lava flow morphology is the slope. A steep slope will tend to favor channelized lava flows, and shallow slopes will tend to favor sheet flows in basaltic pahoehoe lavas with high effusion rates (Hon et al., 1994, Gregg, 2017).

Ropes or compression ridges on the surface of a basaltic pahoehoe flow form as the flow is cooling. They form perpendicularly to the flow while the crust is viscous enough to maintain the folds and ductile enough to not fracture. This window is determined by temperature, ductility contrast, crystallinity, and strain rate (Gregg et al., 1998, Ball et al., 2008). Ball et al., 2008 found that the ropy structures develop on pahoehoe lavas in temperatures between 700 °C and 800 °C. When the temperature drops below 700 °C, brittle deformation starts, and the flow will stop advancing at 600-650 °C.

1.3 North Atlantic Large Igneous Province

The Vøring Margin is part of the North Atlantic Igneous Province and categorized as a volcanic margin, which means it’s a continental margin where marginal highs with overlying volcanic material are present. Certain magmatic products are always present in these volcanic rifted margins, and they are: 1) wedges of SDR’s on either side of the ocean-continent boundary, 2) widespread sill and hydrothermal complexes, 3) High velocity lower crustal bodies located along the ocean-continent boundary and 4) Subaerial lava flows, lava deltas, and volcaniclastic sediments from before or during rifting (Planke et al., 2021a) (see

Figure 1.3).

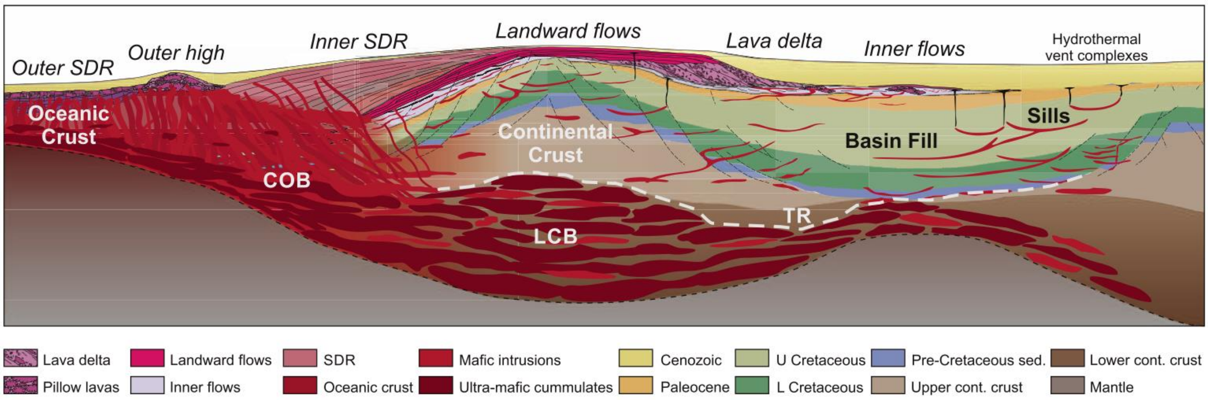

Figure 1.3. Schematic profile across the central part of the mid-Norwegian Margin showing the volcanic units and intrusive magmatic complexes. SDR – Seaward Dipping Reflectors; COB – Continent Ocean Boundary; LCB – Lower Crustal Body; TR – T Reflection. Modified by Planke et al., 2021 b from Millet et al., 2022, Zastrozhnov et al., 2020 and Abdelamak et al., 2017.

Even though there are many examples of volcanic margins around the world, the Vøring Margin is by far the most intensely studied of its kind, and it has contributed to the general understanding of LIP´s. (Berndt et al., 2019).

Many times during the history of the earth there has been periods of magmatic activity, where large amounts of magma has been emplaced during a relative short amount of time in one or several pulses, that are not part of the normal processes that happen on plate-boundaries. When these rough criteria are met, it can be called a Large Igneous Province (LIP), and they can exist as both continental and oceanic varieties. They often have an early onset phase, a main phase with a climax of the eruption (typically lasting < 0.5 million years) followed by a waning phase. Some examples such as the North Atlantic Igneous Province show more than one pulse (Svensen 2019). They are important because they are related to extinction events, break-up of continents and environmental changes (Saunders et al., 2005, Ganino & Arndt, 2009, Storey et al., 2013, Ernst, 2014a, Yang et al., 2020, Berndt et al., 2019).

There is no current definition of Large Igneous Provinces that is universally accepted. The term was first used by Coffin & Eldholm 1994. They defined it as “massive crustal emplacements of predominantly mafic extrusive and intrusive rock and originated via other processes than normal seafloor-spreading” (page 1 in Coffin & Eldholm). The basis they had for this definition was only Mesozoic and Cenozoic “continental flood basalt provinces, volcanic passive margins and similar large-volume oceanic volcanism of intraplate origin such as oceanic plateaus, submarine ridges, seamount groups, and ocean-basin flood basalts" (page 1 in Ernst, 2014a). These where then divided into those that were transient in origin (1-5 million years), and those that were persistent, lasting up to several hundreds of million years. The persistent types include seamount groups and submarine ridges, and these were excluded from the LIP term by Bryan and Ernst, 2008, so that only the events with significant regional to global effects was included (Ernst, 2014a). Their definition of the LIP term was "Magmatic provinces with areal extents >0.1Mkm^2, igneous volumes >0.1Mkm^3 and maximum lifespans of about 50 million years that have intraplate tectonic settings or geochemical affinities, and area characterized by igneous pulses of short duration (1-5 million years), during which a large proportion (>75%) of the total igneous volume has been emplaced" (page 6 in Bryan and Ernst 2008), and this is more widely used today.

1.3.1 Plumbing system

The origin of LIP´s has been widely discussed and many hypotheses has been presented, but the most widespread and accepted explanation is that of a mantle plume (Campbell et al., 2005, Ali et al., 2010, Ernst, 2014b, Liu et al., 2017). The temperature difference between the outer core of the earth and the mantle is several hundred degrees, meaning that plumes of relatively warmer, less dense, and more viscous material will build up and rise from this boundary from time to time. The plume head must be of a considerable size (~1000km in diameter) to have enough uplift to overcome the viscosity from the mantle that is impeding its ascension. Before any eruptions happen, there is an uplift of about 1000m with the circular shape of the plume. When it reaches the lithosphere, it flattens out to a disc-shape with a diameter of 2000 km - 2400 km (Campbell et al., 2005). Then the formation of the plumbing system of the LIP will begin. Every LIP has a unique plumbing system unlike the others, but a general model has been provided by Ernst et al., 2019 (see Figure 1.4). When the plume has reached the lithosphere three instances can happen. The plume material can start to melt and migrate upwards, like it happened in the Siberian Traps LIP, or the thermal flux from the plume material will start to heat the mantle above it, creating zones of melting that will then migrate upwards, like it happened in the Central Atlantic LIP.

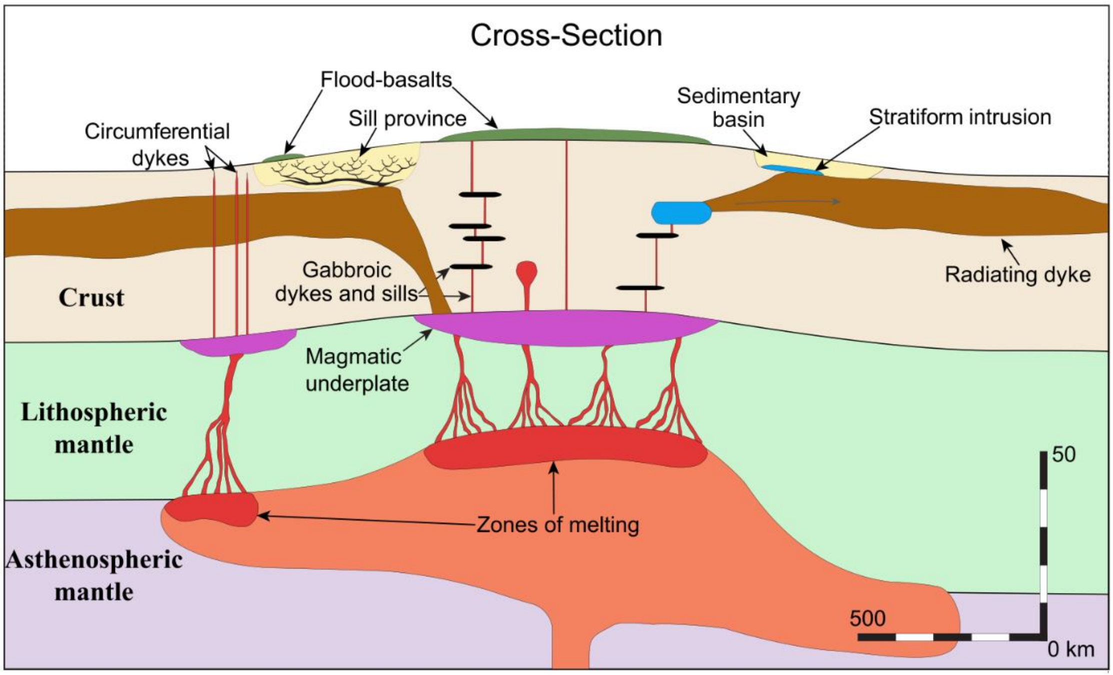

Figure 1.4. General framework of the plumbing system in continental LIP's, shown in a cross section. Magmatic underplating is purple, Mafic-ultramafic intrusions are blue, mafic sills are black, radiating mafic dykes are brown, circumferential mafic dykes are red, and flood basalts are green. The thicker lithosphere on the right prevents mafic magmatism and circumferential dykes on that side. Modified from Ernst et al., 2019.

The third option and perhaps the most common is a mix of the two. When the melts reach the crust, they will accumulate because of their higher density than the crust above, forming magmatic underplating (Bryan et al., 2010). Below the Vøring Margin, there is a high velocity lower crustal body with velocities over 7 km/s, that is commonly interpreted as magmatic underplating (Gernigon et al., 2003, Planke et al., 2021a). Magmas will rise from this underplating to create a 3D plumbing system outward from the source. This can happen in many different geometries, but fan-shaped or radial dyke swarms and sill complexes are typical (Ernst, 2014c). Dykes change from migrating vertically to laterally the longer they travel, and they may travel as much as several thousands of km. The sills can be fed directly underneath by the magmas ascending from the lower crust boundary or they can be fed vertically or laterally from dykes. When entering a sedimentary basin (as in the case of the Vøring Margin) they tend to form as saucer-shaped structures and in some cases, they may be the cause of hydrothermal vent complexes. It may seem like the whole plumbing system is rather constricted to the initial plume ascent, but this is not the case for several reasons. After the plume has reached the lithosphere, it may migrate laterally for up to 1000 km, and the plumbing system itself may also migrate quite a distance laterally before it reaches the surface. As already stated, the dykes themselves might travel as much as thousands of km; these in turn can feed a dyke swarm, which might also reach a couple of hundred km, so the constriction is more so to the sedimentary basin that is intruded (Ernst et al., 2019).

1.3.2 Lava delta

When initial flood basalt volcanism happens in a sedimentary basin environment, it forms shallow intrusions, hydrovolcanic deposits by the interaction between magma and wet sediment, and subaerial lava flows located on the basin highs and margins. The lava flows will gradually cover the topographical features, starting with the troughs and depressions on its way. If the lava flow reaches the sea, the water will make it fragment and create a foreset bedded lava delta made by hyaloclastites and locally massive flows. Research on these features is important for paleoenvironmental studies, hazard mitigation and hydrocarbon exploration (Wright et al., 2012, Smellie et al., 2013, Bosman et al., 2014, Planke et al., 2017, Soule et al.,2021, Eidesgaard et al., 2023). They are the volcanic version of the tripartite structured Gilbert-type sedimentary deltas. The topset is consisting of subaerial lavas and is overlying the subaqueously deposited foreset beds of hyaloclastites. These two units are separated by a zone called the passage zone. It marks the area where lava is entering the sea and therefore marks the water level at the time of deposition. The degree of fragmentation of the lava when submerged in the water is different depending on the type of lava, and consequently the delta structure will also vary. Pahoehoe-lavas are relatively porous, permeable, and has higher vesicularity compared to 'A'A lavas that are more massive. More importantly, the 'A'A lavas are thicker and tends to form an insulating crust. This means that 'A'A lavas will cool slower and travel further under water before it freezes in place. Pahoehoe lavas will brecciate and fragment completely, shortly after entering the water, creating steep delta front and well developed foresets. 'A'A-fed lava deltas will more often show chaotic internal structure than well-developed foresets (Skilling et al., 2002, Smellie et al., 2013, Bosman et al., 2014).

These deposits have a low strength and because of the high energy in the coastal environment slumping happens, regional escarpments occur, and the deposits will often get eroded and redeposited as volcanic sediments in gravity mass flows (Planke et al., 2017). These events are called bench collapses when they occur as explosive, catastrophic events. The "benches" are unstable parts of the delta formed upon the remnants of an earlier collapse. When they collapse, they transport material down the slope and create a minor escarpment on the coastline as shown on Figure 1.5

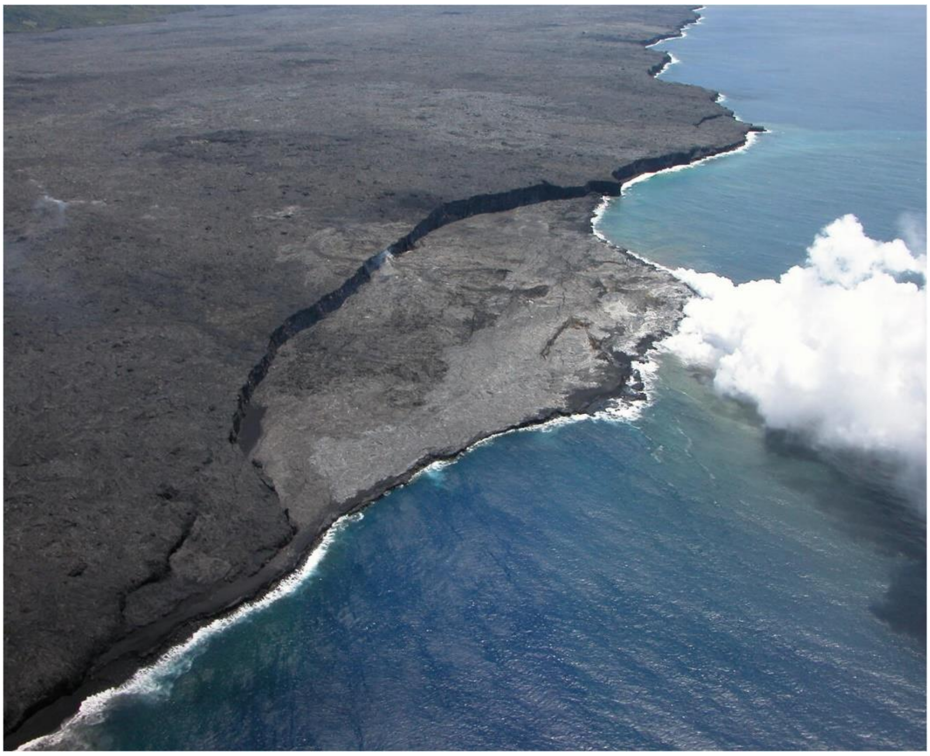

Figure 1.5. Lava delta at East Lae'apuki on the southcoast of Kilauea Volcano in Hawaii showing two bench collapses. Photo is from the USGS website: https://www.usgs.gov/media/images/active-lava-delta-se-coast-kilauea-hawaii (accessed march 2024)

All the different facies can be seen on Figure 1.3 where inner flows, landwards flows, lava delta, and seawards dipping reflectors are all presented. The Inner Flow unit appears on seismic as hummocky reflections with a chaotic internal structure, and it has a general sheet-like outline. It represents an aggradational bottom set of the lava delta and consists of fragmented basalt, volcaniclastic rocks, pillow lavas, shallow intrusions, and massive sheet flows. It is deposited in a broad basin and shallow marine environment (Abdelamak et al., 2016b). The lava delta can easily be identified by its prograding inner structure. The landwards flows (Figure 1.3) form sheets of subaerial lava that transitions into the lava delta when it reaches the escarpment. West of the landward flows, the seaward dipping reflectors can be found.

1.3.3 Seaward dipping reflectors

Seaward dipping reflectors are high-amplitude reflectors that diverge and increase in dip towards the ocean, and they are the largest volcanic constructs on earth (Buck, 2017). They are found on all volcanic passive margins and are associated with the transition from continental rifting to seafloor spreading (McDermott et al., 2018).

There are currently 2 main models for the formation of SDR's and they can be applied to different episodes of rifting (Mutter et al., 1982, Paton et al., 2017, Collier et al., 2017, McDermott et al., 2018, Morgan & Watts, 2018, Harkin et al., 2020, Gomez-Romeu et al., 2022). The volcanic faulting model ("SDR type I" on Figure 1.6) involves mantle stretching and normal faulting and is connected to the initial rifting and extension. It can therefore often be seen as the inner SDR's. It can be compared to syn-rift sedimentary growth packets in extensional basins that are not volcanic. The SDR packages are wedge-shaped and internally straight reflections terminating against a fault block that is dipping towards the land.

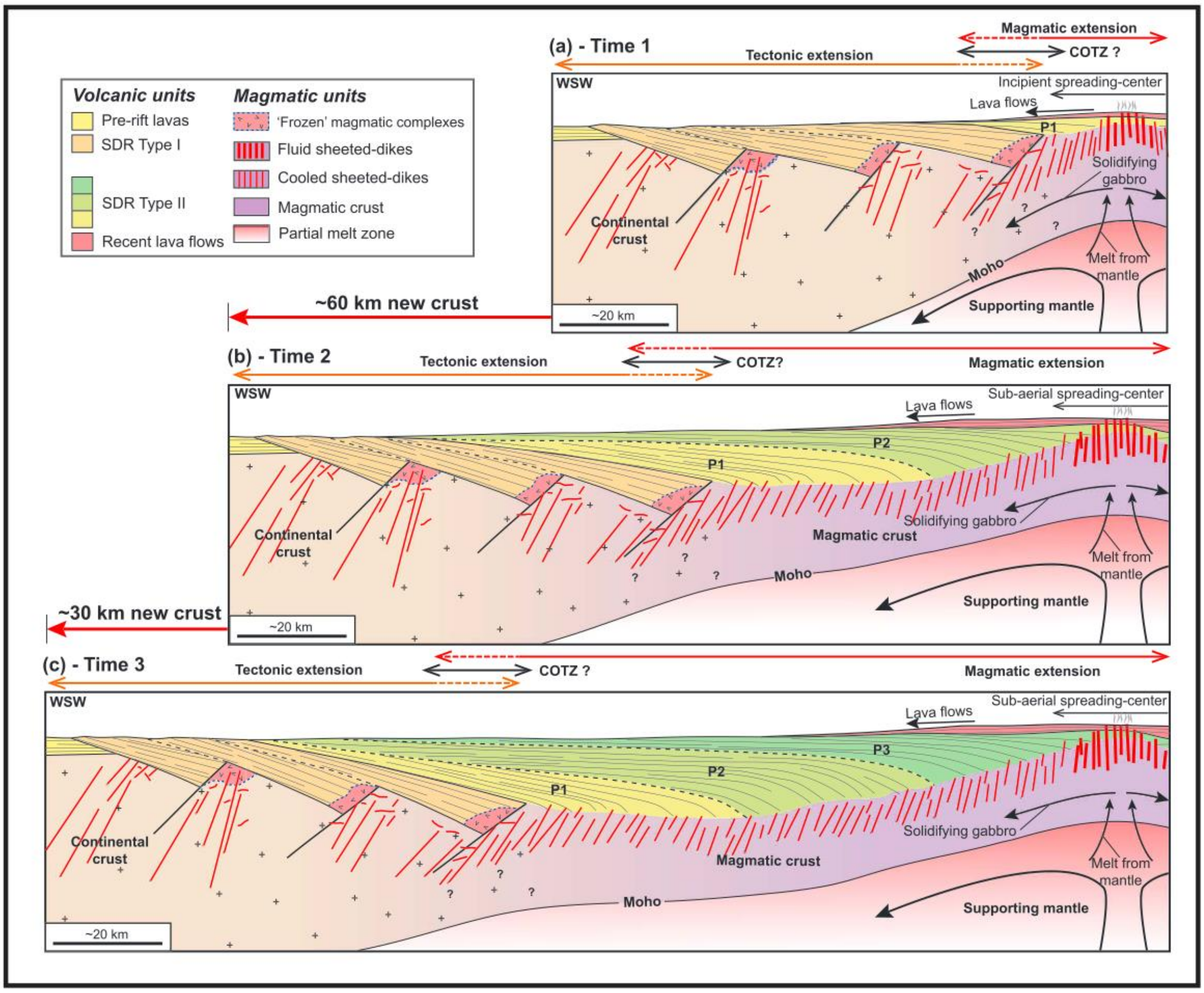

Figure 1.6. Formation of SDR's. COTZ is the Continent Ocean Transition. Modified from McDermott et al., 2018.

The accommodation space for the lava packages is thus created by the normal faults. The lavas are erupted subaerially and have a continental affinity in their composition, which means they can be found on top of continental crust (see Figure 1.4) (McDermott et al., 2018, Harkin et al., 2020).

The volcanic loading model ("SDR type II" on Figure 1.6) is connected to the crystallization of mafic dykes, causing flexure, and bending the SDR's. This is associated with a later phase in the break-up. Here, the accommodation of the lavas is made by plate spreading. They are also erupted subaerially but have an ocean-ridge composition with little continental contamination, and they are found on top of crust that resembles oceanic more than continental crust. The spreading center is kept subaerial by the new hot and buoyant crust, but as it travels it cools and begins to sink, bending it downwards. New flows continually fill the depression and acts as an additional bending force. Eldholm et al., 1989 and Gibson & Love, 1989 found that the SDR sequence on the Vøring Marginal High was formed by normal fault extension in continental crust because it consisted of subaerial, tholeiitic basalt flows with a high silica content. Xenoliths of gneiss and quartz-mica schist acted as further proof that the underlying basement was continental crust (McDermott et al., 2018; Harkin et al., 2020).

1.3.4 Large Igneous Provinces and mass extinctions

As mentioned earlier, there is a link between LIP´s, mass extinctions, and global climatic changes and many authors have sought to clarify this link (Ganino & Arndt, 2009, Kravchinsky et al., 2012, Jones et al., 2016, Ernst & Youbi, 2017, Berndt et al., 2019, Black et al., 2021). For 4 of the great mass extinctions there has been a LIP that correlates with it temporally, and the same for every minor crisis since the Permian (Jones et al., 2016). There is, however, not a LIP for every mass extinction and not a mass extinction for every LIP so the connection is not just straight forward. What we do know is that LIPS has a great climatic impact on the carbon and sulphur cycles through magmatic degassing, release from contact metamorphism, and subsequent weathering. The potential kill mechanisms could be global warming, global cooling, ocean anoxia, ocean acidification, sea-level changes, and toxic metal release (Ernst & Youbi, 2017). This connection is also not so easy to explain, because every LIP has a different effect on the climate due to different duration, chemistry, latitude, type of intruded sedimentary rock, volume, how the climate is when the LIP forms, and so on.

The most apparent climatic effect from LIP´s is the emission of greenhouse gasses from magma degassing and eruptions, but it has been shown that the impact of the degassing of sediments affected by intrusions, such as hydrothermal vent complexes (HVC´s), might have a possibly even greater impact (Ganino & Arndt., 2009, Jones et al., 2016, Bond & Sun, 2021). Hydrothermal vent complexes are pipe-like complexes formed by fracturing, transport, and eruption of hydrothermal fluids and sediments, and they are essential parts of LIP´s (Planke et al 2005). They originate from explosive release of gasses generated when sills are emplaced in volatile-rich sediments that has a low permeability (see Figure 1.7). The thermal aureole of the sill will create contact metamorphism and conductive and convective heat transfer. If there is a lot of fluids generated and the permeability of the host rock is low, the pressure will build up, and if large enough to exceed the pressure from the overburden, a HVC will be created through catastrophic failure of the overlying material (Angkasa et al., 2017).

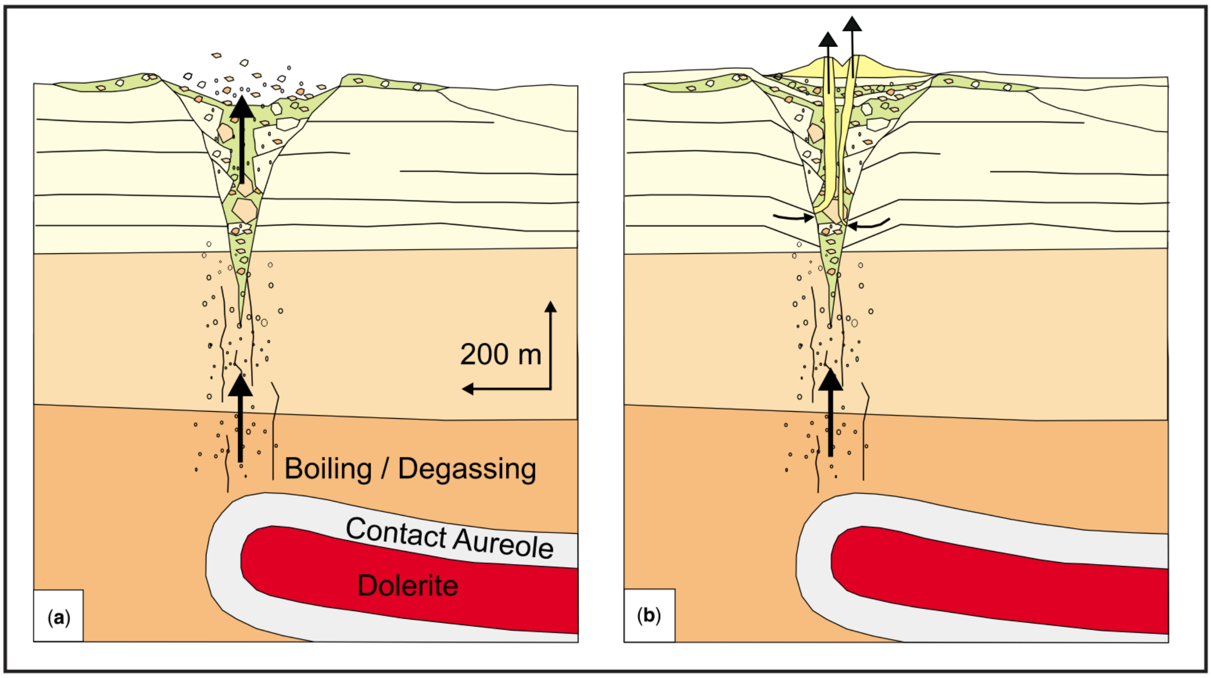

Figure 1.7. Formation of Hydrothermal Vent Complexes. In (a) the pore fluid pressure builds up because of boiling pore fluids and gas release from degassing of magma, causing the vent complex to develop as a cone-shaped structure. The first explosive events create fragmented breccias. In (b) the vent complex further develops, and now pipes of fluidized sandstone ascend through the cone-shape, meaning that the fluid pressure gradient is less critical. From Jamtveit et al., 2004.

They have been found in the Siberian Traps, Karoo and the North Atlantic Igneous Province, but since they are hard to image due to the volcanic rocks typically placed above them, they are estimated to be more widespread than we know of (Angkasa et al., 2017, Ernst & Youbi, 2017).On the Vøring Margin, there has been found 734 hydrothermal vent complexes and 2000-3000 are estimated to be present (Planke et al., 2005).

The climatic impact of an HVC depends on the composition of the host rock. When intrusions are emplaced in dolomite, evaporites, organic rich shale or coal it tends to create large quantities of greenhouse and toxic gasses but when emplaced in sandstone, basalt or granitoids the effects are negligible (Ganino & Arndt, 2009)

1.4 Previous work

Many authors have investigated the Vøring Margin and Skoll High, and several have used the same data used in this thesis. The findings of these authors will briefly be introduced here as to present the knowledge that has already been established with the data and establish a common ground zero. Planke et al., 2017 used the CVX1101 3D cube to generate remarkable results about the volcanic structures at Skoll High. They interpreted the top basalt and presented subaerial lava flows with compressional ridges and inflated lava lobes, a pitted surface explained by pseudocraters, channels proving surface water, faults, and compared them to field analogs. They also compared the escarpment morphology with active volcanic environments in Hawaii and inactive eroded escarpments in South Africa and found that they were similar, suggesting that the creation of flood basalt provinces is controlled by the same emplacement mechanisms and eruption styles as modern volcanic systems. They found the top basalt horizon to be complicated because of weathering, erosion and deposition of volcanogenic sediments. They measured the escarpment to be 1 km high with a dip of 25°-30° and stated that slumps and debris flows of volcaniclastic facies has flowed down the escarpment. An area in the SW of the data beneath the escarpment is interpreted as prevolcanic sedimentary highs. These are incised by channels which, has been overflown by lava-fed debris flows, that represent late stage eruptions on Skoll High.

Planke et al., 2023b and Lebedova-Ivanova et al., 2023 have investigated the CAGE 22-5 3D cube data and found that it is divided into a pitted domain and a faulted domain. These differences are interpreted to result from different emplacement environments. The pitted domain is formed from basalt flows flowing over a wetland environment, and the faulted surface originates from subaerial basalt flows that has subsequently been faulted. The pitted domain shows lobate structures with linear ridges that has a spacing of some 10's of meters. 270 pits was mapped with a radius from 6 to 50 meters and a mean radius of 16 meters. The depths of the pseudocraters vary from meters to a few tens of metres. The pitted basalt surface is suggested to have undergone rapid subsidence and burial under a low energy coastal environment since it has not been significantly eroded.

Kilhams et al., 2021 and Maharjan et al., 2024 have investigated the base basalt horizon over Skoll High. Kilhams interpreted the base basalt as an erosive surface, since several reflectors truncate against it from underneath, and proposed that the southwestern area of Skoll High is domed due to "a large Christmas-tree network of sills, termed a laccolith" (page 13 in Kilhams et al., 2021). Maharjan et al., 2024 measured the basalt thickness to be 200-600 m along the landward flows, over 1000 m along SDR's and the lava delta, and under 500 m along the inner flows.

Angkasa et al., 2017 used a field example from Skye Island in Scotland to prove that sills can create chimneys directly above their tips, that cut through the extensive overlying basalt sequence. They mapped several of these occurrences at the Vøring Marginal High in the CVX1101 dataset and found evidence of a shallow intrusion creating a forced fold in the sediments above. They also concluded that the facies structure and physical properties of the base basalt transition vary greatly depending on the presence of water at the onset of LIP volcanism.

Abdelamak et al., 2016a and Abdelamak et al.,2016b used over 500 2D lines to look into the entire Vøring Margin with respect to volcanic seismic facies. Abdelamak et al., 2016a defined the lower series flows underneath the base basalt (k-reflection) as "wavy to continuous subparallel reflections with an internal disrupted and hummocky shape" (page 1 in Abdelamak et al., 2016a). They represent the transition from a sedimentary amagmatic rift to a magmatic dominated rift on the Vøring Margin as well as feeder dykes for the SRD´s. Abdelamak 2016b divided the Vøring Margin into five different segments with different control factors resulting in differences in accommodation space. They found that within segment E3 containing Skoll High, the lava thickness is ranging from 300 m to 500 m in the lava delta, and the landwards flows has a thickness of less than 500 m. This is generally much less than the rest of the escarpment. This segment is also characterized by slumps, slides and delta collapse. Surface seepages were identified and connected to the development of highs in the inner flows. The highs are generally parallel to the fault system of the North Gjallar Ridge.

Furthermore, the concept of seismic volcanostratigraphy developed by Planke et al., 2000 (and Berndt et al., 2001) have laid the foundation for identifying and interpreting the different igneous facies in rifted margins and helped to provide constraints on their development.

2 Geological background

2.1 Study area

The Vøring margin is bounded by the Jan Mayen fracture zone to the south-west and the Bivrost Lineament to the north-east (Berndt et al., 2001). It includes the Trøndelag-platform to the south-west and the Vøring Basin and Vøring Marginal High towards the northwest (see Figure 2.1) (Hjelstuen et al., 2004).

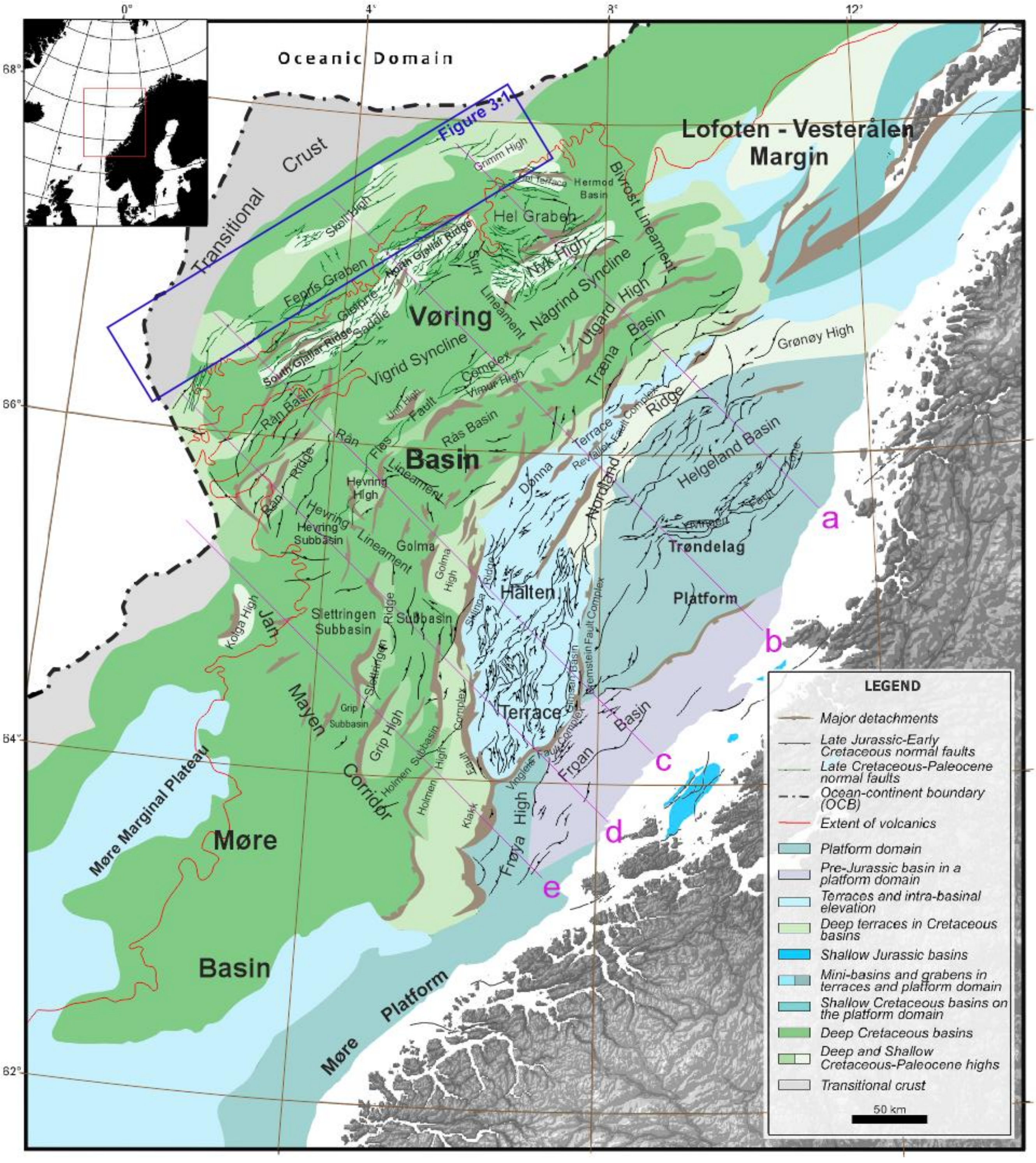

Figure 2.1. Overview map of the Vøring Margin. Modified from Zastrozhnov et al., 2020.

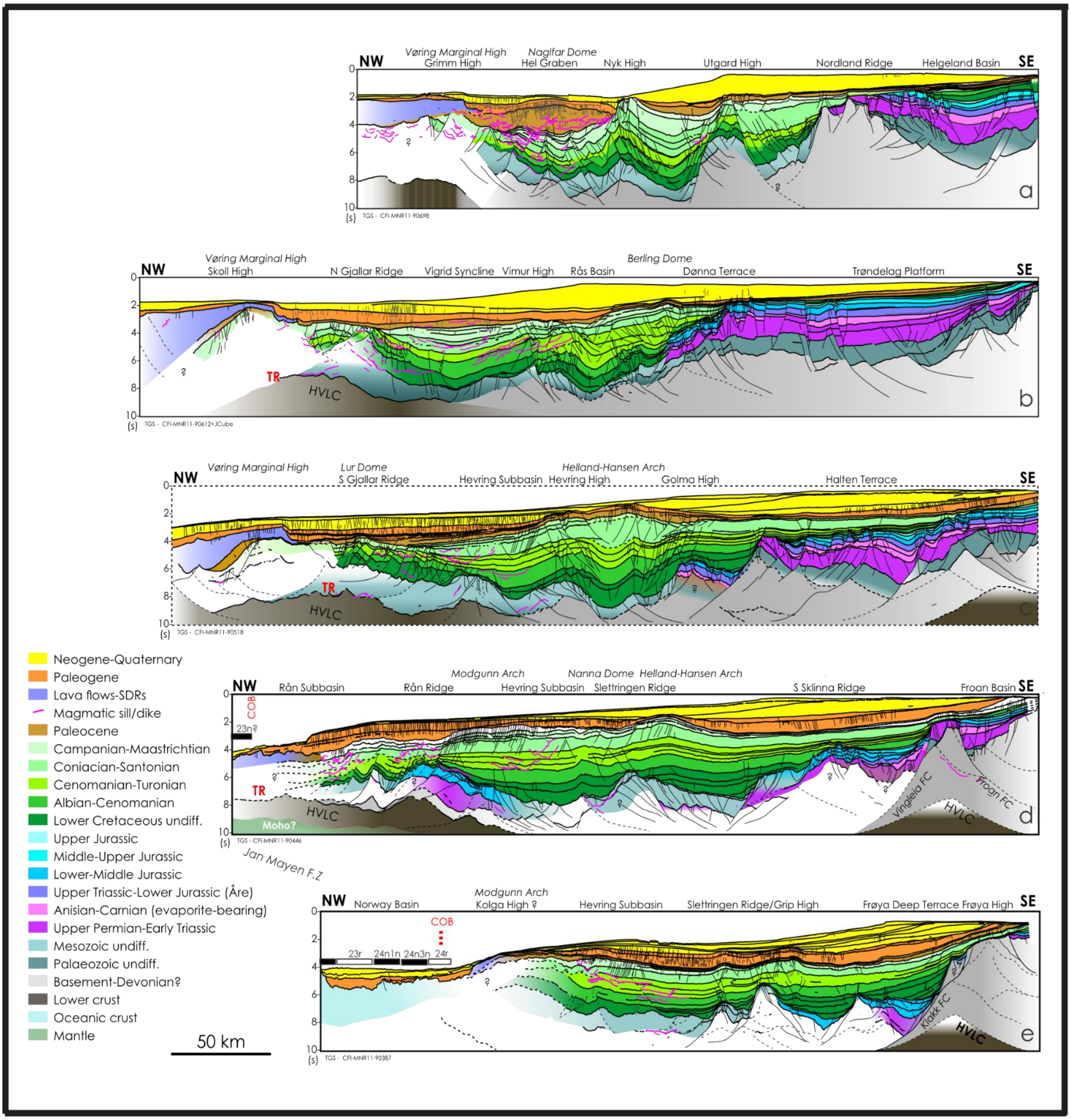

Figure 2.2. Key regional sections from the Vøring Margin. COB – Continent Ocean Boundary; HVLC – High Velocity Lower Crust; TR – T Reflection. Locations can be seen on Figure 2.1. Modified from Gernigon et al., 2021.

2.2 Evolution of the Vøring margin

2.2.1 Pre-Cretaceous

The structure of the Vøring Margin as it is observed today, is due to several extensional episodes, ultimately leading to the breakup between Greenland and Norway in Late Paleocene - Early Eocene (56 million years ago) (Skogseid et al., 1992). These extensional episodes started after the collapse of the Caledonides during Late Silurian – Early Devonian. This formed several extensional basins onshore Norway as well as regional strike-slip movements. The major regional rifting episodes are in Late Carboniferous - Early Permian, Middle Jurassic – Early Cretaceous, and Late Cretaceous – Paleocene (Ren et al., 2003, Gac et al., 2022). During Late Carboniferous – Early Permian, regional rifting and block faulting took place in most of the proto-North Atlantic Sea, forming the Froan Basin (see Figure 2.1 and 2.2). Extensional phases in this period initiated the structuring of the Nordland Ridge. Block faulting occurred in the Triassic, further developing the Froan Basin. Evaporite intervals were deposited in this period up to 400m thick. These helped create detachment surfaces for normal faults in the later rifting episodes. Growth faulting happened in late Triassic early Jurassic, largely due to the Triassic evaporite intervals. (Blystad et al., 1995, Mjelde et al., 2003)

2.2.2 Jurrassic

The area that became Halten Terrace in Late Jurassic – Early Cretaceous was faulted in Jurassic: NE trending, Early Jurassic growth faults in the eastern area that were not reactivated later, Late Jurassic faults in the southwestern area that were also not reactivated later, and faults in the northwestern area that were reactivated during Late Jurassic – Early Cretaceous. This happened during an extensional phase leading to major faulting and reactivating of older fault zones, especially on the eastern flank of the Træna basin (Blystad et al., 1995, Mjelde et al., 2003). This extensional phase is one of the three major rifting events on the Vøring Margin and the Vøring Basin was developed by regional subsidence after this event. The Fles Fault Complex which splits the Vøring Basin in two, is also developed in this period and is later reactivated in the Late Cretaceous – Paleocene rifting event (Blystad et al., 1995, Ren et al., 2003). Other elements originating from this period include the Gimsan Basin, Grip High, Helgeland Basin, Klakk Fault Complex and Slettringen

Ridge. Gimsan Basin was formed by subsidence and rapid sedimentation, Grip High was formed by faulting, Helgeland Basin was formed by normal faulting in the northwest, downwarping in the southeast, and is closely linked to the erection of the Nordland Ridge (Blystad et al., 1995). The structuring of the Nordland Ridge that started in Late Carboniferous – Early Permian culminated in uplift and erosion in late Middle Jurassic – Early Cretaceous. This was also connected to a Middle to Late Jurassic flank uplift with the Sklinna Ridge, the southwestern Froan Basin and Frøya High, developing the eastern part of the Trøndelag Platform (Blystad et al., 1995).

2.2.3 Early Cretaceous

In early Cretaceous there was a depocenter in the Någrind Syncline connected to faulting/rifting activity on the eastern flank of the Nyk high. The Nyk high had already emerged at this time, and the Utgard high was an initiating horst configuration. Another depocenter in the Golma Subbasin was connected to west-dipping detachment faults on the structural high next to it. There was no deposition in the Træna Basin yet. The Nordland Ridge was a positive feature, and it was connected to lateral subsidence in the Helgeland Basin (Zastrozhnov et al., 2018, Zastrozhnov et al., 2020). This period is also referred to as the Neocomian, and during this time the terraces, highs, and ridges to the east of the Trøndelag Platform took shape and formed a contrast to the adjacent basins. The Hel Graben developed as a part of the Vigrid Syncline, but it wasn´t before Cenomanian that it started to develop as a separate structure (Blystad et al., 1995).

2.2.4 Albian-Cenomanian

In mid Albian to mid Cenomanian there was mainly subsidence in the Vøring basin. The main depocenter was the Rås basin, which is confined to the northwest by structural highs in the Fles Fault Complex and to the southwest by the Rån Lineament. The Rån Basin was also a significant depocenter and this was due to a major west-dipping detachment/fault system. Infilling of the Ribban, Rås and Træna basins created faulting along their flanks. Minor depocenters were located southwestwards of the Northern and Southern Gjallar Ridge, Ylvingen fault zone was reactivated, and the northern part of the Vøring Margin followed the trend of Early Cretaceous. Until Cenomanian, the western margin of the Vøring Basin was confined to the present location of the Vøring Escarpment, and the eastern margin was confined by the Revfallet and Klakk Fault Complexes (Blystad et al., 1995, Zastrozhnov et al., 2018, Zastrozhnov et al., 2020).

2.2.5 Late Cretaceous

In the first half of late Cretaceous the formation of the Gjallar ridge was initiated by uplift and eastward tilting of the western Vøring Basin. This meant that the post Cenomanian sediments onlapped the Cenomanian sediments dipping to the east (see Figure 2.2), and the mirror image of this structure can be found across the Frøya high (Blystad et al., 1995). The main depocenters were the Træna Basin, the Rås Basin, and the Hevring Basin. The Træna Basin depocenter has to do with thinning subsidence moving northward from the Rås Basin in this period. Another depocenter is again present in the Någrind Syncline (Zastrozhnov et al., 2018, Zastrozhnov et al., 2020).

In the period from the middle of the late Cretaceous to Campanian, a new large depocenter formed in the Træna basin up to 6 km thick. Fault-driven tectonic subsidence stopped around Santonian, and hereafter the basin was passively infilled. The Någrind Syncline continued to accumulate sediments and the Northern Gjallar Ridge, the Hel Terrace and the Utgard High were in relatively high positions (Zastrozhnov et al., 2018, Zastrozhnov et al., 2020). After Cenomanian, the Vøring Basin was dominated by rifting, block faulting, and higher subsidence rates. This meant that faulting was mainly on the Revfallet, Bremstein, and Vingleia fault complexes on the Halten Terrace, forming the eastern flank of the Vøring Basin. On the western flank of the Vøring Basin there was faulting along the Gjallar Ridge. This meant that both the eastern and western borders of the basin moved a little eastward and now included the Halten and Dønna Terraces to the east, but did not include the area between the Gjallar ridge and the Vøring Escarpment.

The period after Cenomanian constitutes the main subsidence of Hel Graben and the Någrind Syncline, due to the Surt Lineament and boundary faults on the northwestern side of the Nyk High. The Rym Fault Zone, which is part of the Surt Lineament, was created as normal faults in the Late Cretaceous – Paleocene, and later reverse movements are related to the creation of the Naglfar Dome (Blystad et al., 1995).

From mid-Campanian to base-Paleogene, the main depocenter migrated northwestwards from the Træna and Rås Basins to the Någrind Syncline, the Vigrid Syncline, the Gleipne Saddle and a minor depocenter in the Hel Graben. The southwestern part of the Någrind

Syncline was not affected by faults, but in the northeastern part, subsidence might have been helped by reactivation of faults on the border to the Nyk High. Nyk high, North and South Gjallar Ridge, Utgard High, Hel Terrace and the Fles Fault Complex were all in a relatively high position. This is also the period in which initial regional uplift and extensional faulting started, and this continued until the final breakup (Zastrozhnov et al., 2018, Zastrozhnov et al., 2020). This is the final major regional rifting episode in the development of the Vøring Margin (Ren et al., 2003, Gac et al., 2022). In Maastrichtian to Paleocene, faults on the western side of the Gjallar Ridge were reactivated and formed Fenris Graben as well as the Gjallar Ridge. The base Tertiary unconformity that is present on Gjallar Ridge is downfaulted in the Fenris Basin and forms the floor for the Paleogene sediments (see Figure 2.2). On the ridge, the unconformity is onlapped by Paleocene, meaning that pre-tertiary sediments are transitioning into Eocene at the top of the ridge. The Nyk High obtained the present structure during the Maastrichtian – Paleocene tectonic phase, and the Halten Terrace obtained the morphology that can be seen today in the Late Cretaceous, at the same time as the Vingleia and Bremstein Fault Complexes developed. (Blystad et al., 1995). At the time of the Cretaceous-Paleocene boundary, a regional uplift is observed in the North Atlantic rift system, which is believed to represent the Iceland mantle plume interacting with the base of the lithosphere (Gernigon et al., 2003, Ren et al., 2003). This uplift and erosion meant that the Vøring Basin stopped developing, and since the eastern boundary of the basin was overstepped in the beginning of Paleocene (see Figure 2.2) (thereafter including the Trøndelag Platform), the basin is a Cretaceous basin by definition, even though it has been reworked by tertiary tectonics and deformation (Blystad et al., 1995).

2.2.6 Paleocene

During Paleocene the main depocenter migrated northwest again towards Hel Graben, the Hermod Basin and Fenris Graben, and faulting moved towards the volcanic domain. The Vigrid and Någrind Synclines were minor depocenters, not controlled by faults, but being sedimentary elements originating from the adjacent eroding highs (Zastrozhnov et al., 2018, Zastrozhnov et al., 2020). It was also in Paleocene that intrusions started in the Vøring Basin, and they grew in intensity towards the break-up. The base Tertiary horizon can be considered a rift unconformity in the outer part of the Vøring Basin. This is due to initial rifting and uplift, which caused erosion on the Vøring Basin (Eldholm et al., 1989).

The Vøring Marginal High was formed in late Paleocene by a fault due to rifting, separating the Vøring Marginal High from Fenris Graben. The escarpment structure was later enhanced by massive emplacements of flood basalts (Mjelde et al., 2003). The final breakup then happened in late Paleocene – Early Eocene. The outer Vøring Margin was uplifted and eroded in the synrift phase, and this phase is also associated by voluminous igneous activity resulting in seaward dipping reflectors, landward flows, lava deltas, inner flows, shallow intrusions, sills and hydrothermal vent complexes (see Figure 1.3) (Mjelde et al., 2003, Planke et al., 2005, Faleide et al., 2008). The rifting and extension have generally moved northwestwards together with the depocenters, until it reached the point where the final breakup happened (Zastrozhnov et al., 2018).

After the breakup, the Vøring Margin was mainly influenced by regional subsidence, because of thermal cooling and compressional events due to ridge push (Zastrozhnov et al., 2018).

2.2.7 Eocene-Holocene

At the end of early Eocene, the Vøring Plateau was still uplifted and therefore eroded, but the whole margin was part of the regionally subsiding Tertiary Marginal Basin, connected to the oceanic crust being formed in the Lofoten Basin northwest of the margin. Sediments in the Vøring Basin where transgressing westwards, and they reached the Vøring Escarpment in middle Eocene. From the middle of Eocene to middle Oligocene a major depocenter developed in the outer part of the Vøring Basin, and in the early Miocene, the whole marginal high was covered with sediments except for local highs. The Brygge Formation was deposited from Early Eocene to Early Miocene time (Rise et al., 2010). Biogenic, hemipelagic and pelagic material became more dominant as the terrigenous component at the inner margin increased. Hereafter, the margin is characterized by sedimentation and subsidence until late Miocene. A small exception to this is Mid Miocene where a minor compression phase took place causing uplift of the part of the margin closest to land, creating the Mid Miocene Unconformity. After the Mid Miocene Unconformity, the coast parallel Molo formation is deposited as a proximal event to the deep marine Kai formation from Early Miocene until Early Pliocene. In late Miocene there was a progressively larger calcareous sediment component transitioning into an alternating sequence of carbonate-rich and carbonate-poor glacial sediments in the late Pliocene. The sediments from late Pliocene and onwards belong to the Naust Formation. (Eldholm et al., 1989, Rise et al., 2010).

3 Data and methods

3.1 Seismic data

The main dataset used for this thesis is the CVX1101 3D seismic cube acquired in exploration license PL527 for Chevron Norge. It was acquired and processed by CGG Veritas. It covers an area of 2963 km^2, and has a 25 x 12,5 m inline and crossline bin size. The extent of the cube can be seen in Figure 3.1. Additionally, a high resolution 3D seismic cube was used. This data was collected on cruise CAGE 22-5 as a collaboration between the Center of Excellence for Arctic Gas Hydrates, Environment and Climate (CAGE) in Tromsø, and the Center for Earth Evolution and Dynamics (CEED) in Oslo. The data was post-processed and quality-checked by the very same centers. It covers an area of 17,8 km^2 and has a 6,25 x 6,25 m inline and crossline bin size. This cubes extent and location is also shown on Figure 3.1. A 2D line from the same cruise, that covers both well U1571, U1572 and 6704/12-1 has been used to correlate horizons between the wells (Figure 3.1 & Figure 3.2).

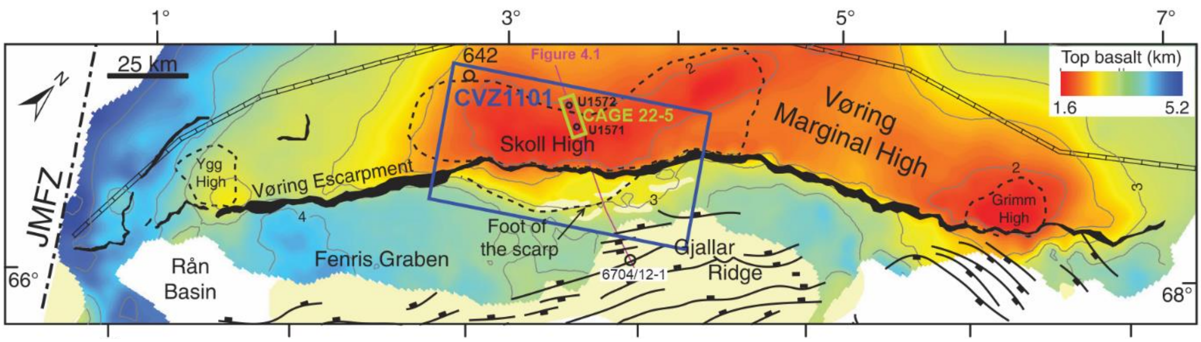

Figure 3.1. The extent and location of the two 3D cubes used in this thesis. Modified from Planke et al., 2017. The location of this figure can be seen in Figure 2.1.

3.2 Interpreting in Petrel

The Petrel 2023 software has been used to work with the data. Several volume attributes have been created. Structural smoothing of the original seismic 3D cubes was made with dip correction to aid with the picking of the top basalt. This is useful for highlighting where the larger amplitudes are, and seeing the general structures, but at the same time, details are lost, so both the original and the smoothed versions have been considered when picking the top basalt.

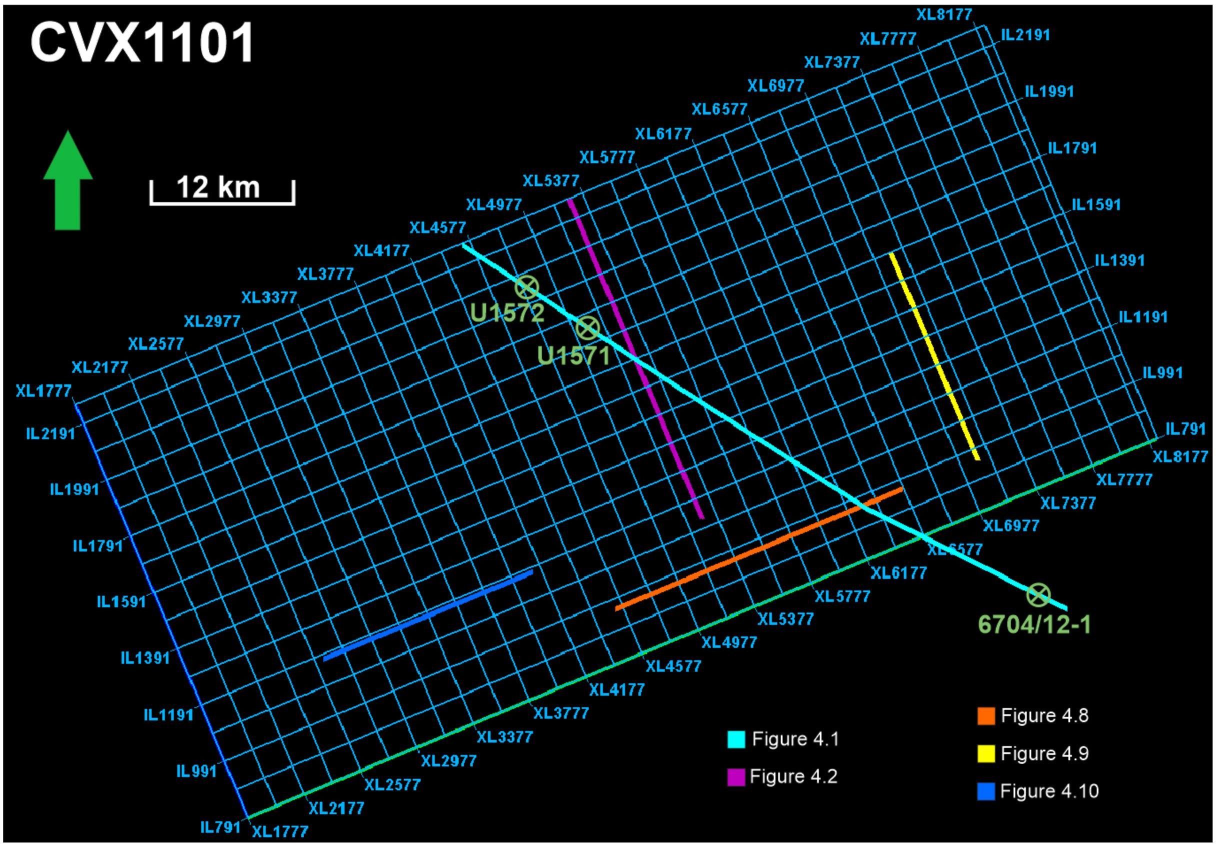

Figure 3.2. The outline of the CVX1101 3D cube showing the location of seismic lines presented in the results later as well as their respective inline and crossline number and the three wells used.

Variance cubes has been generated with dip-correction. This attribute is showcasing the horizontal discontinuities from the original seismic cube, making it useful for faults and other structures cutting vertically through the data. The variance of the smoothed version of the original cube has also been generated for better fault tracking.

RMS (root mean square) amplitude volumes has been created as the default setting: a window of 9 samples. When making the RMS amplitude volume, Petrel takes the squareroot of the sum of the amplitudes inside the given window and divides it by the number of amplitude values used, meaning it's a slightly modified mean inside each window. This attribute is good for identifying areas with high amplitudes and seeing the amplitude differences over larger areas.

An attribute volume with the cosine of the phase has been created in order to improve the interpretation of the base basalt surface. This attribute is often used with the polarity, and it is good for interpretation in poorly resolved areas. The boundaries become very sharp since the cosine function makes the output values range from -1 to 1.

Generalized Spectral Decomposition cubes has been made for both 3D seismic cubes.

Spectral decomposition is a process that uses Fourier transformation to translate the seismic signal into its constituent frequencies. This can be done by various methods and the Short Time Fourier Transform, using a fixed length wavelet, and the Continuous Wavelet Transform, using a fixed number of cycles, are some of the most common. The method used in the Petrel software is a hybrid of these two methods.

3 frequencies are needed for the spectral decomposition. These frequencies can be determined by looking at the spectral analysis of the dataset (Figure 3.3). The first three peaks in frequency are 6 Hz, 9 Hz, and 13 Hz for the CVX1101 3D cube, and 45 Hz, 85 Hz, and 125 Hz for the CAGE 22-5 3D cube. A variety of different peaks has been tested, but these turned out to be the best. From these frequencies, 3 new volumes have been generated with the “General Spectral Decomposition” function from each original seismic cube.

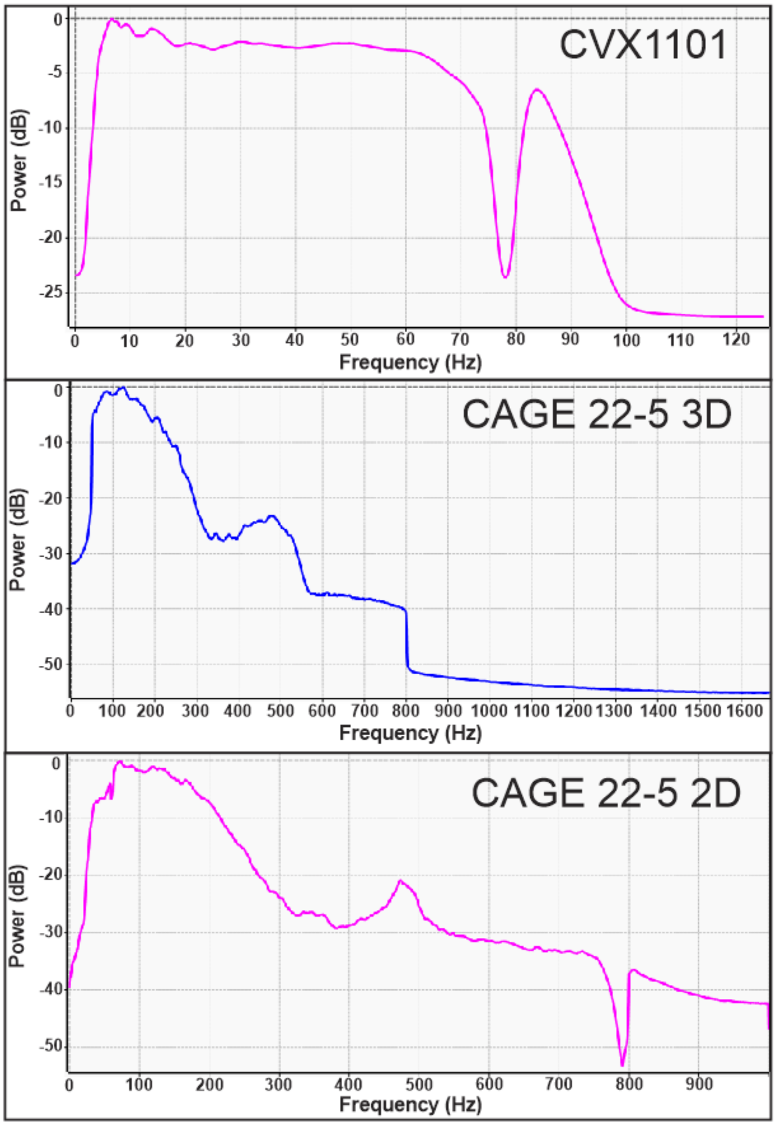

Figure 3.3. The Spectral Analysis of the two 3D seismic cubes and the 2D line used in this thesis.

When the new volumes are generated, they can be merged in the "Mixer Tool". With this tool it is possible to show the volumes together in red, green, and blue colors, such that the lowest frequency volume has red, the middle frequency has green, and the highest frequency has blue. This way a new "volume" will be made and can best be shown in a timeslice. This means that each volume coming out of the mixer is the result of three volumes from the spectral decomposition, each with a signature color.
When picking horizons in the 3D seismic cubes, the main picking tool has been the 3D autotracker. When picking an event, I have made sure to follow the autotracked parts as they were generated by the program, to make sure it did not interpret too nonchalantly. In especially difficult sections, the 2D autotracker was used on a number of in-lines and x-lines before running the autotracking. On the CAGE 22-5 3D cube for example, every 25th inline and crossline was interpreted with the 2D autotracker before using the 3D tracking to avoid confusing the autotracker in the high resolution dataset. Another utilized technique is to turn down the sensitivity of the autotracker and interpret in smaller intervals. Additionally, it has helped a great deal to autotrack on the smoothed volumes.
In difficult sections it might sometimes be tempting to use the manual interpreter or the guided 2D tracking, because this gives a sense of better control on exactly where the horizon goes. However, this has been refrained from, because these tools will often create artefacts when used in conjunction with the 3D autotracking, which is close to mandatory to use on a 3D volume because it makes the most detailed surface by far.
The main horizon that has been picked is the top basalt. The sedimentary horizons presented later, has been picked out because they were the strongest reflections onlapping the top basalt surface.
The top basalt has been interpreted every 10th in-line and x-line because it is a difficult surface to pick out precisely, and therefore autotracking on large areas is not optimal. The rest of the horizons are more continuous and have therefore only been picked every 50th x-line or so. The base basalt surface was first determined by 3D autotracking on the RMS amplitude volume. This is because the base basalt reflection is very faint, and the RMS amplitude helped to highlight it for the autotracker. Autotracking was naturally not enough since the base basalt is still hard to define even on the RMS amplitude volume, so the volume with the attribute "cosine of the phase" was used for refining the surface.
The faults were picked manually on a smoothed variance volume. The autotrack function was

used with modification in cases of very long faults. Otherwise, every 10th crossline or inline have been picked. When converting these complicated fault planes into simple planes that can be put in a stereonet, a mean of the dip angle and dip azimuth has been used.

A tool that has been very useful in imaging the data is the horizon probe. This function lets you show one or more volumes in relation to a surface. With this tool, the variance and RMS amplitude has been extracted in a 30 ms window, 15 ms over and 15 ms under the top basalt surface. Various windows have been tested, but this was the best for showing the top basalt features, and it is the same window Planke et al., 2017 used. Unfortunately, the horizon probe is not very good for showing the details of said attributes along the surface, so it has only been used to find the best interval to extract attributes from.
The last important function used is “Flatten Cube”. This deforms the data in a 3D cube such that a specific surface is aligned horizontally at a chosen Two Way Traveltime (TWT). This is useful because the cube created with the mixer function to show the spectral decomposition cannot be extracted along a surface. So instead of putting the spectral decomposition values on a surface, they have been flattened so they can be shown on a timeslice. Practically, this means flattening the original seismic volume before doing general spectral decompositions. In the case of the CAGE 22-5 data, the spectral decomposition is overlain by a volume that has gone through structural smoothing, variance has then been calculated, and in the end, the cube has been flattened. This technique along with the specific values for generating the CAGE 22-5 spectral decomposition has been taught to me by Ben Manton from Volcanic Basin Energy Research in Oslo, Norway, who used this procedure for Lebedova-Ivanova et al., 2023 on the exact same dataset.

3.3 Polarity

When defining the polarity, it is a question of what standard to use. Here, the standard of Sheriff 1996, also sometimes referred to as the SEG (Society of Exploration Geophysicists) standard is used. According to this, a positive reflection coefficient will create a peak at the layer boundary and a negative will create a trough (see Figure 3.4). One reflection that will always create a positive reflection coefficient is the seafloor reflection. This reflection has therefore been used to determine the polarity in the two 3D seismic datasets and the 2D line on Figure 3.4. It can be seen that both 3D datasets have a zero phase normal polarity, and the 2D line has a minimum phase reverse polarity according to Sheriff 1996.

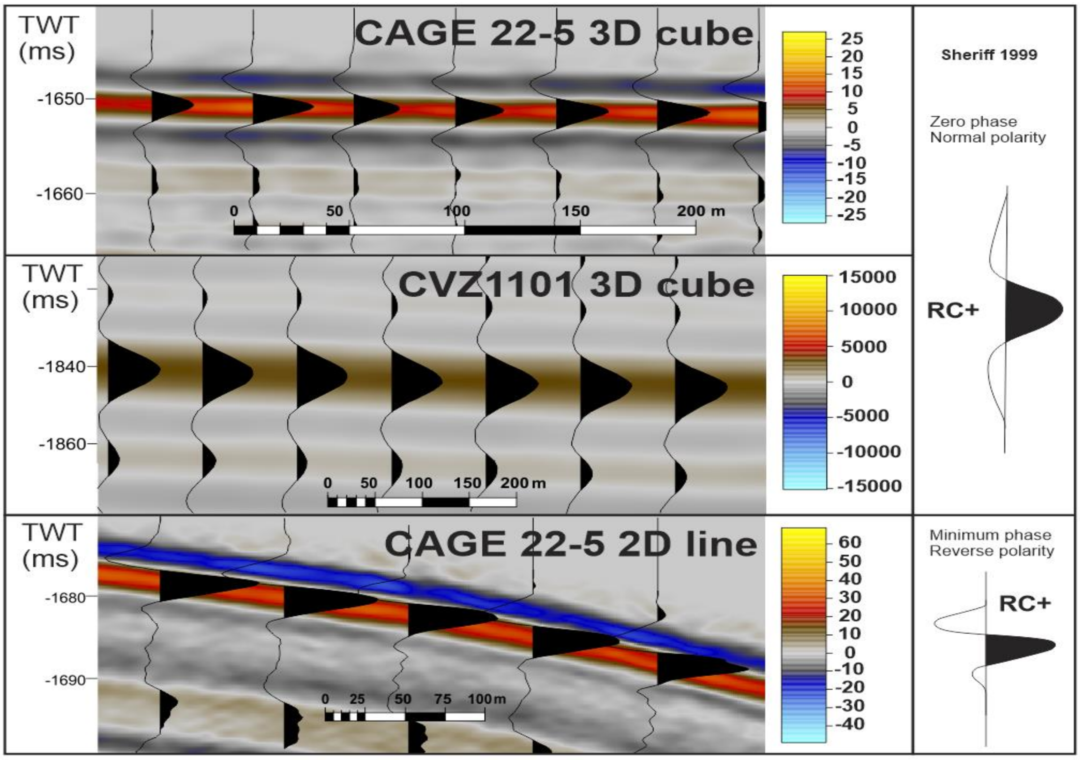

Figure 3.4. The upper section is showing a snip of the seafloor from the CAGE 22-5 dataset, the middle section is showing a snip of the seafloor from the CVX1101 dataset, and the lower section is showing a snip of the seafloor from the CAGE 22-5 2D line. The wavelets to the right are showing Sheriff 1996's version of a zero phase normal polarity and a minimum phase reverse polarity given that the reflection coefficient is positive.

3.4 Resolution

Resolution is the minimum distance two objects needs to have between them, so that they can be distinguished as separate features. It can be split into horizontal and vertical resolution and generally depends on the wavelength. The wavelength is in turn dependent on the velocity of the substrate and the frequency of the signal in the following relation:

$$\lambda = \frac{v}{f} \qquad \textit{Equation 1}$$

Where λ is the wavelength in meters, v is the velocity in $\frac{m}{s}$, and f is the frequency in Hertz. This means that the resolution will tend to decrease with depth, because the velocity will most often increase with depth, and the frequency will decrease with depth. Therefore, the wavelength will increase with depth, giving a worse resolution than in the above layers. (Badley, 1985, Brown 1999)

3.4.1 Vertical resolution

The vertical resolution is the minimum thickness a layer can have while being detected on a seismic profile. This thickness is dependent on the dominating wavelength. If the wavelength is greater than that of a layer, the seismic response wavelet from the upper boundary of the layer will interfere with the wavelet created by the lower layer. This means that the top and bottom of a layer will be separatable if the time thickness of the limestone is equal to, or greater than, half the wavelength (which would be the same as one wavelength in two-way traveltime) of the seismic wavelet (Badley (1985) (Figure 3.5). As the layer thins, the interference will increase until the time thickness of the layer is a quarter of the wavelength. Here, the interference is at its maximum, and this is called the tuning thickness. In this thickness, the layer will appear as one single strong reflection.

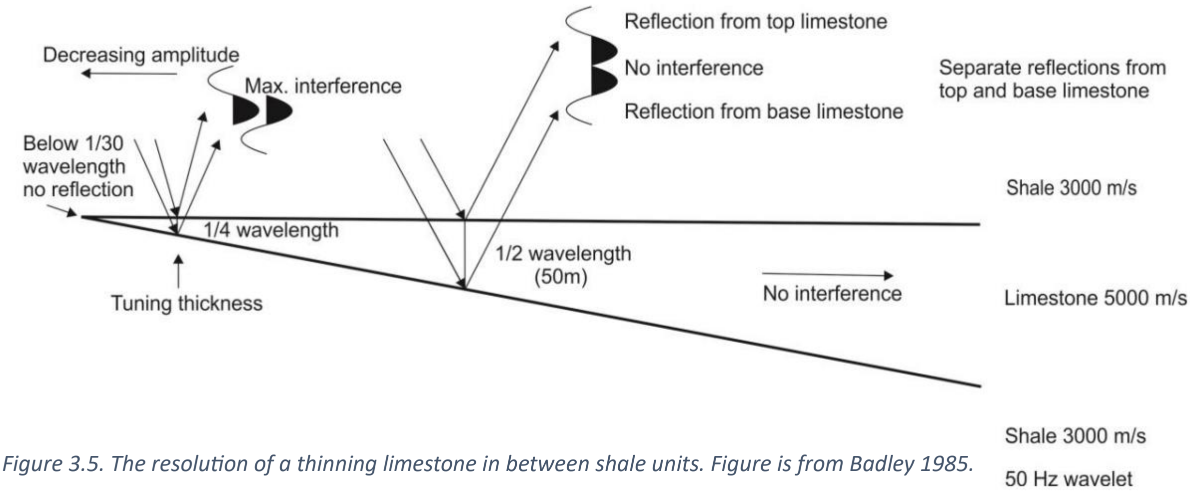

Figure 3.5. The resolution of a thinning limestone in between shale units. Figure is from Badley 1985.

The layer should theoretically be detectable down to 1/30 of the wavelength, but a fourth of the wavelength is commonly used as the vertical resolution (Equation 2) (Badley, 1985).

$$Vr = \frac{\lambda}{4} \qquad \textit{Equation 2}$$

3.4.2 Horizontal resolution

The horizontal resolution can be calculated in two ways, depending on if the data has been migrated or not. If the data has not been migrated, the resolution is determined by the Fresnel zone. This is the area of the reflector that is represented in the first quarter wavelength of the signal (see Figure 3.6).

The radius of the Fresnel zone is given by:

$$r = \frac{v}{2}\sqrt{\frac{t}{f}}$$ *Equation 3*

Where r is the radius of the Fresnel zone, v is the velocity, t is the two-way travel time, and f is the frequency. It can also be seen directly from this equation that the radius of the Fresnel zone is increasing with depth, with contributions both from the time and the velocity.

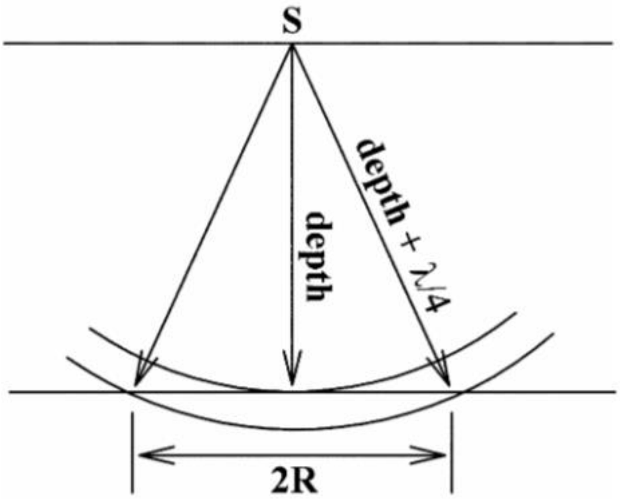

Figure 3.6. The Fresnel zone in relation to depth and wavelength. Figure is from Dewangan et al., 2007.

If the data has been migrated (which it has In this case), the horizontal resolution is given in the same way as the vertical resolution (Equation 2):

$$Hr = \frac{\lambda}{4}$$ *Equation 3*

Since the horizontal and vertical resolution is calculated the same way, I will henceforth refer to both when I mention resolution.

For an overall expression of resolution, the spectral analysis of each dataset can be examined. This is shown in Figure 3.3, and here it can be seen that the dominant frequencies are about 5-75 Hz for the CVX1101 3D cube, 50-300 Hz for the CAGE 22-5 3D cube, and 20-300 Hz for the CAGE 22-5 2D line.

If an average velocity of 1500 m/s is assumed, the general resolution can then be calculated for each dataset. This will yield a resolution between 5 m and 75 m for the CVX1101 3D cube, 1,25 m and 8 m for the CAGE 22-5 3D cube, and 1,25 m and 19 m for the CAGE 22-5 2D line.

This is of course a very unprecise calculation, but it can nonetheless be seen that the CAGE 22-5 data has a considerably better resolution than that of the bigger CVX1101 3D cube. For more precise resolutions, sonic data from wells and measured periods or frequencies from the seismic is needed. For the velocity in Table 1 and Table 2, sonic data from Saga Petroleum well 6704/12-1 and IODP wells U1571 and U1572 has been used. For the "overlying sediments" section I used an average of unit I-VI from the IODP wells (section 3.5) and the sediment package from the Saga Petroleum well 6704/12-1 down to 2300 ms TWT, which roughly corresponds to the bottom of the sediment package. The velocity of unit VII from U1572 (section 3.5) is used as the top basalt velocity, and since the bottom basalt has not been drilled, the unit VIIIb velocity (section 3.5) has been used as an approximation. The dominant frequency has been found by measuring wavelet periods and frequencies on the seismic interpretation window in Petrel with the "measuring tool" and the "spectrum tool" from the "Inspector". The inspector gives several very precise peak frequencies, and after measuring the wavelet period in the given area, the frequency that fits best have been determined. Then the limit of resolvability and the limit of detectability has been calculated, and the results are presented in Table 1 and Table 2. The chosen values for the dominant frequencies in the tables (Table 1 and Table 2) fit quite well with the peaks in the spectral analysis tool in Figure 3.3. It's hard to tell for the CVX1101 dataset since it has been very well processed, and the curve is relatively flat between 6Hz and 75 Hz, but there is a slight peak at 31 Hz.

Resolution table (λ/4)	Dominant Frequency	Overlying sediment	Top Basalt	Base Basalt
Sonic log Velocity		1550 m/s	4120 m/s	5000 m/s
CVX1101	31 Hz	12,5 m	33,2 m	40,3 m
CAGE 22-5 3D	104 Hz	3,7 m	9,9 m	12,0 m
CAGE 22-5 2D	94 Hz	4,1 m	11,0 m	13,3 m

Table 1. The resolutions of the three datasets used in this thesis calculated for 3 different surfaces. The "Overlying sediments" account for a thick succession of sediments, but they have been categorized as one, as they share characteristics when compared to the top basalt. The sonic log velocities marked with red have been estimated from the Saga Petroleum well 6704/12-1 and IODP wells U157 and U1572 (Aubert et al., 1999, Planke et al., 2023a). The dominant frequencies for each dataset have been found in Petrel with the "Measuring tool" and the "Spectrum tool" from the "Inspector" in the seismic interpretation window.

Detection table (λ/30)	Dominant Frequency	Overlying sediment	Top Basalt	Base Basalt
Sonic log Velocity		1550 m/s	4120 m/s	5000 m/s
CVX1101	31 Hz	1,7 m	4,4 m	5,4 m
CAGE 22-5 3D	104 Hz	0,5 m	1,3 m	1,6 m
CAGE 22-5 2D	94 Hz	0,5 m	1,5 m	1,8 m

Table 2. The same as Table 1, except this is showing the limit of detectability instead of the limit of resolvability.

3.5 IODP wells

4 wells were drilled on the Skoll high during the IODP expedition 396 cruise (Planke et al., 2023a): Well 1571A, 1571B, 1572A, and 1572B. They are shown on Figure 3.1. The 1571 wells are 20 m apart, and the 1572 wells are 150 m apart. Cores and wireline logs have been retrieved and based on biostratigraphy, physical properties, macroscopic observations, and microscopic analysis, 8 units are determined (Planke et al., 2023a).

Unit	Hole 1571A	Hole 1571B	Hole 1572A	Hole 1572B	Age
I	0-72,5 m	0-58,95 m	0-77-88 m	0-80 m	Quarternary
II	---	---	77,88-78,65 m	80-93,46 m	Late Miocene
III	72,50-102,71 m	58,95-97,96 m	87,33-1126,20 m	93,46-122,83 m	late Early Miocene to late Middle Miocene
IV	---	---	126,20-155,30 m	122,83-158,94 m	Late Eocene to late Early Miocene
V	102,71-11,40 m	97,96-105,52 m	155,30-174,8 m	158,94-178,71 m	middle Middle Miocene
VI	111,40-126,88 m	105,52-117,22 m	174,8-204 m	178,71-209,67 m	early Middle Eocene
VII	---	---	204-228,43 m	209,67-210,48 m	Early Eocene
VIIIa	126,88-141,43 m	117,22-128,19 m	---	210,48-222,15 m	Early Eocene or earlier
VIIIb	141,43-242,35 m	128,19-142,54 m	228,43-325,34 m	---	Early Eocene or earlier

Table 3. Depth intervals of the 8 units identified in the 4 wells on Skoll High by Planke et al., 2023a. The depths are given in core depth under the seabed, and all the information comes from Planke et al., 2023a.

The following is a short summary of the 8 lithologic units found in the 4 wells by Planke et al., 2023a.

Unit I is mainly grayish brown unconsolidated mud. It shows cyclic color variability between gray and very dark grey clay. Clasts and dropstones can be found, and rare organic matter have been found in some intervals. The unit has high bulk densities (mean 1,74 g/cm^3), high gamma ray (average 42 counts/s), and low P-wave (~1560 m/s) values. The moisture and density samples (MAD) showed an average porosity of 58%.

Unit II consists of greenish gray consolidated mud and nannofossil ooze. The transition from unit I to unit II is mainly based on an increase in consolidation but also on physical properties. In places, it shows bioturbation and fresh glass. The average P-wave velocities, bulk densities, and gamma ray values (NGR) in the unit are ~ 1500m/s, 1,49g/cm^3 , and 24 counts/s, respectively. The MAD samples shows an average porosity of 74%.

Unit III consists of greenish gray and very dark brown consolidated clay, very dark gray diatomite, and diatom ooze. The boundary between unit II and unit III is set where the sediment changes from light greenish gray nannofossil ooze to dark greenish gray well consolidated clay. The unit is bioturbated and in places parallel lamination, wavy lamination, sand layers and ash rich intervals can be found. Mean bulk density and p-wave velocities are 1,37g/cm^3 and ~ 1525m/s and the top of the unit is characterized by a sharp increase in NGR.

Unit IV consists of greenish gray radiolarian ooze interbedded with gray to black ash, and it can only be found at site U1572. The transition between unit III and unit IV is determined by a change from dark grayish brown diatomite to dark greenish gray claystone. Some intervals show parallel lamination, and bioturbation. Mean bulk densities, p-wave velocities, and NGR are 1,39g/cm^3, ~1573 m/s, and 30 counts/s respectively.

Unit V is very dark gray clay to claystone with ash beds. The transition from unit IV to unit V is marked by a gradational change from greenish gray diatom ooze with ash to very dark brown organic rich clay with thin parallel lamination. Wavy lamination, bio-siliceous intervals, and bioturbation can be found throughout the unit and sandstone intervals can be found at site U1571. The mean p-wave velocity, bulk density, and NGR of the unit are ~1565m/s, 1,33g/cm^3, and 21 counts/s, respectively. MAD samples show a mean porosity of 81%.

Unit VI is overlying the volcanic rocks in all four holes and the lithology of it varies. Well 1571A shows volcaniclastic siltstone and sandstone, well 1571B shows dark clay and sand, well 1572A shows very dark gray diatom rich siltstone with rare ash beds, and well 1572B shows dark gray radiolarian/bio-siliceous ooze with ash beds and very dark grayish brown claystone and siltstone at the bottom. The transition from unit V to unit VI is characterized by an increase in the abundance of ashes and volcaniclastics along with a change in physical properties. The bottom of the unit lying directly on top of the basalt, contains the freshwater fern Azolla massulae and glochidia, suggesting that these sediments are all latest Early Eocene in age. The mean values for P-wave velocity, bulk density, and NGR in the unit are ~1620m/s, 1,46g/cm^3, and 33 counts/s, respectively. MAD samples show a mean porosity of 73%.

Unit VII is very restricted in the wells (Table 3) and can only be found at site U1572. In hole 1572B the 1 meter thick interval is basaltic andesite. In hole 1572A, it consists of basaltic andesite transitioning downcore to massive basalt. The basaltic andesite is significantly altered with high amounts of recrystallization in clay minerals. At the very bottom of the unit, gray silt-rich gravel claystone is observed. The unit is characterized by high bulk densities (2,53 g/cm^3) and P-velocities (~4120m/s), and low NGR (11 counts/s) similar to subunit VIIIb.

Unit VIII is basalt flows and interbasalt sediments, and it is divided into two distinct subunits. Subunit VIIIa consists of hyaloclastite alternating with volcanic mudstone. Subunit VIIIb is basaltic lava flows and mudstone. It showed 11 basaltic lesser subunits and 10 sedimentary lesser subunits in well 1571A, 2 basaltic lesser subunits and 1 sedimentary lesser subunit in well 1571B, and 11 basaltic lesser subunits and 11 sedimentary lesser subunits in well 1572A. The two subunits show significantly different physical properties. VIIIa has mean values of ~1800m/s, 1,55 g/cm^3 and $\sim$68% for P-wave velocity, bulk density and porosity respectively, and looks more like the low velocity, low bulk density interbasaltic sediments than that of the basalt flow interiors in subunit VIIIb, that shows velocities of 5000 m/s, bulk densities of 2,5 g/cm^3, and a porosity of $\sim$38%.

3.6 Well 6704/12-1

Well 6704/12-1 is drilled by Saga Petroleum and they have established chronostratigraphy and divided into formations as shown in Table 4.
Underneath is a short summary of the formations in well 6704/12-1 as described by Aubert et al., 1999.
The Naust Formation is Pleistocene of age and consists of soft to very soft clay grading toward soft to firm claystones in the bottom half.
The Kai Formation is early Middle Miocene of age and consists of silica ooze with small amounts of clay. The unit is split into two segments: an upper transparent unit and a lower high reflectivity unit can be seen on the seismic, which is reflecting a density contrast at the Opal A to Opal CT transition.
The Brygge Formation has been split into 3 units based on logs and biostratigraphy. The Upper Brygge Formation is Oligocene of age and consists of silica ooze with an increasing amount of clay. The Middle Brygge Formation is Early to Middle Eocene of age and consists of clay and claystone with small amounts of sand and limestone stringers. The Lower Brygge Formation is Earliest Eocene of age and consists of the same lithology as the overlying Middle Brygge Formation.

Chronostratigraphy	Unit tops	Thickness
Pliocene - Quaternary	1377	129
Unconformity ?		
Upper Middle Miocene	1506	85
Lower Middle Miocene	1591	183
Lower Miocene	1774	86
Upper Oligocene – Lower Miocene	1860	104
Middle Oligocene	1964	206
Unconformity ?		
Middle Eocene	2170	224
Lower Eocene	2394	24
Lowermost Eocene	2418	135
Uppermost Paleocene	2553	2
Upper Paleocene	2555	1
Upper Campanian to Lower Maastrichtian	2556	317
Upper Campanian	2873	527
Middle Campanian	3400	300
Lower to Middle Campanian ?	3700	220
Lowermost Campanian	3920	162
Santonian to Campanian	4082	21
TD	4103	

Groups	Formation Tops	Depth m MD RKB	Depths m TVD RKB	Thickness (m TVD)
Nordland Group	Naust Formation Kai Formation	1377 1459	1377 1459	82 461
Hordaland Group	U. Brygge Formation M. Brygge Formation L. Brygge Formation	1920 2170 2425	1920 2170 2423	250 253 121
Rogaland Group	Tang Formation	2548	2544	9
Shetland Group	Springar Formation Nise Formation	2558 3244	2553 3238	685 >856

Table 4. Chronostratigrahy and lithostratigraphy in top depths and thicknesses of the units found in Saga Petroleum well 6704/12-1 from Aubert et al., 1999

3.7 Well logging methods

The following is a short summary based on Rider 1996 meant to give a brief introduction to the well logs presented later. Things that go for all logs are that they each have a resolution and penetration depth to be aware of, and that they can only give hints about a formation individually. It is only when used in a combination that the magic happens, and one can start to interpret truths about a formation.

3.7.1 Gamma ray log

The gamma ray log is a measure of the natural radioactivity of a formation. The radiation comes from uranium, potassium, or thorium, and it can be measured as one in a simple gamma ray log or separately in spectral gamma ray log. Shales typically have high gamma ray values, and therefore the gamma ray log is often used as a shale indicator, but this is not always the case. It can also be sensible to acid igneous rocks, organic matter, and some evaporites. Igneous basic rocks have low radioactivity and intermediate and acid type rocks have a high radioactivity. The log is often used for correlation because it is repeatable, has character, and is not affected by depth. On average, the tool measures about 20 cm vertically above and below the detector and 10 cm radially, but this varies with density. This means that each reading is an average spanning these dimensions.

3.7.2 Sonic log

The sonic log measures a formations ability to transmit sound waves. It is measured in interval transit time, which is reciprocal to the velocity, which usually varies with lithology, texture, and porosity. It is mostly used to assess porosity and as a tool to obtain interval velocities, which can be used to calibrate the log with the seismic section. The borehole compensated tool measures the p-Wave velocity and consists of two transmitter receiver groups. Each group has one transmitter, a short receiver, and a long receiver, and one of the groups are inverted. This is good because the time the wave travels in the drilling mud can then be canceled out by subtracting transit time of the short receiver from the long receiver, leaving only the transit time in the formation between the short and the long receiver. This means that the resolution is the distance between the receivers, which is typically 61 cm.

3.7.3 Density log

The density measures the bulk density of a formation, which is a mix of the solid matrix density and the density of the fluid in the pores. It is used for calculating porosity, hydrocarbon density, and acoustic impedance, but it is also useful as a lithology indicator. When used as a lithology indicator it is almost always used in conjunction with the density log. The tool works by sending out gamma rays that attenuate by Compton scattering through the formation until it gets picked up by a detector. This attenuating is dependent on the electron density, which in turn has a very close relationship to the actual density. This tool has two receivers, the same way as the sonic tool, to compensate for the borehole effects, since the gamma rays will have to travel through the drilling mud before reaching the formation. This tool is measuring while pressed against the borehole wall, which means it only takes account of one side, and that the quality of the log needs to be checked with the caliper log. The penetration depth is typically around 10 cm, and the resolution is about 60 cm for measuring true densities and 15 cm for resolving beds. Combined with the facts that this log is very dependent on borehole conditions and doesn't reach out of the invaded zone, this means that it is very good for defining bed boundaries, but less so for detecting fluids or hydrocarbons on its own.

3.7.4 Resistivity log

The resistivity log is measuring the resistance to a passing electric current in a formation, and it is measured by an induction tool. Generally, rocks and sediments are insulators, but potential fluids in their pore space are conductors. The exception to this relationship is when hydrocarbons are present in the pores, because hydrocarbons are infinitely resistive. Put simply, the resistivity depends on the resistivity of the pore fluids and the F-factor. The resistivity of the pore fluids would mostly depend on salinity and presence of hydrocarbons. The F-factor is an expression of how well the pore spaces are distributed so that a current can pass effortlessly through. In clays this gets a bit more complicated since the clay itself will also carry some of the current, but it depends greatly on the surface area available in the clay.

The tool itself is simply measuring the potential drop between two electrodes passing current between each other, which means it's important that the bore muds are conductive. If the bore muds are conductive, they are affecting the measured resistivity of the formation. This effect will be different based on the penetration depth of the chosen tool. Sometimes the resistivity is measured with different penetration depths as to get resistivity values for the flushed, invaded, and uninvaded zones expressed as shallow resistivity, medium resistivity, and true resistivity respectively. The shallow resistivity log is best for detecting vertical differences, since it has the highest resolution, but is not very good for giving true resistivities since it is very affected by the drilling mud. The true resistivity log is very good for giving the true resistivity since it is not very affected by the drilling mud, but it is not very good for detecting vertical differences since it has the lowest resolution. The resolutions vary from under 30 cm to over 3 m.

3.8 Interpreting the top basalt

When interpreting the top basalt surface, some things have been prioritized over others, and these are accounted for here. Table 5 has been used as a general guide for picking out the different facies. According to this table the top basalt is mostly disrupted and discontinuous and has a high amplitude. Therefore, it has been prioritized to always pick the high amplitudes rather than keep a smooth surface. In some places the top basalt is interfering heavily with lower reflectors, and in those instances, I have abstained from picking anything. There are a few spots where the top basalt seems to disappear. The reason for this is discussed later, and in those places I have picked the top basalt in a continuous time surface. These areas can be seen as the black areas (low RMS amplitude) in Figure 4.5 in the result chapter.

In the top basalt surface (Figure 4.4 in the result chapter), the outline of the CAGE 22-5 data seems to stand out. This is because this area has a higher resolution, and I have prioritized to have a higher resolution in this area rather than a smooth surface.

Seismic facies unit	Reflections characteristics			Volcanic facies	Depositional environment
	Shape	Boundaries	Internal		
Inner Flows	Sheet	Top: high amplitude, disrupted, rough being onlapped or concordant. Base: negative polarity often obscured	Chaotic sheet-like body of very disrupted or hummocky reflections	Massive and fragmented flows, volcanoclastics and hyaloclastics	Shallow marine deposited in broad basin
Lava Delta	Bank	Top: high amplitude or reflection truncation. Base Reflection truncation or termination	Progradational reflection configuration	Massive and fragmented basalts and volcanoclastics	Coastal
Landward Flows	Sheet	Top: high amplitude, smooth being onlapped or concordant. Base: law amplitude, disrupted	Parallel to subparallel. High-amplitude disrupted	Flood basalts	Subaerial or shallow marine flood basalts deposited on a plain or in broad basin
Inner SDR	Wedge	Top: intermediate to high amplitude, smooth with pseudoescarpment. Base: seldom defined	Divergent arcuate or sometimes a divergent-planar pattern	Flood basalts	Subaerial flood basalts deposited in subsiding structure

Table 5. Description of the different igneous seismic facies in the area. Table is from Abdelamak et al., 2016a.

3.9 Basalt volume calculation

The calculation for the volume of the basalt is a bit peculiar so I will shortly go through it here. When the calculation is done in Petrel, it gives an area, and a volume. The area is correct, but since the surfaces are in TWT, the time component of the volume needs to be converted to distance using a velocity:

$$\frac{Volume\left[\frac{m^2}{ms}\right]}{Area[m^2]} = TWT\ [ms]\ component$$

$$\frac{TWT \cdot 10^{-3}}{2} = Time\ [s]$$

$$Time[s] \cdot velocity\left[\frac{m}{s}\right] = Distance\ [m]$$

$$Distance\ [m] \cdot Area[m^2] \cdot 10^{-9} = Volume[km^3]$$

The velocity is estimated from Planke et al., 2023a. Here, four different velocities have been measured from cores of the basalt units at Skoll High, and the average value of these is 4244 m/s, so that is the value used for the velocity in the calculation above.

4 Results

This chapter consists of the main findings of this thesis and presents the work described in the previous chapter (Chapter 3). The stratigraphic correlation will be established as the first thing followed by facies interpretations. Then the top basalt will be presented being the main part of the work before moving on to details on seismic lines and faults planes. In the end of the chapter, the base basalt will be described, and a basalt volume calculation carried out.

4.1 Stratigraphic Correlation

All the interpreted stratigraphic horizons with a time-constraint have been correlated with either the IODP wells U1571 & U1572 (Table 3), the Saga Petroleum 6704/12-1 well (Table 4), or both (Figure 4.1). For the Saga Petroleum 6704/12-1 well, the correlation is direct, meaning that the well formation tops of Base Naust and Base Kai have been loaded into Petrel to be shown along with the seismic, leaving only the lateral interpretation of the horizon to be done. In the case of the IODP well U1571 & U1572 it's not so simple, since the well data has not been directly available. Because these wells are very central to the data, this has been compensated for by taking the well logs along with the interpreted stratigraphy and putting it manually on top of the seismic (Figure 4.1) (Planke et al., 2023a). Since the well logs and stratigraphic intervals are measured in meters below the seafloor and the seismic is shown in TWT, this is not a direct correlation and therefore needs to be used only indicatively. The well logs and stratigraphic intervals are stretched to fit the only two known points on the seismic: the seafloor and the top basalt. Additionally, Planke et al., 2023b made a correlation with the well data and the seismic, so this has been used as a guideline.

4.1.1 Horizons

The lithological unit I is restricted to Quarternary, and the base of it corresponds with a major negative reflective coefficient on the seismic (Figure 4.1). This seems to fit with the base of the Naust formation, which is also what is interpreted by Planke et al., 2023b.
The next horizon interpreted appears to fit with the base of lithological unit III. Unit III is Miocene of age and the base transitions into different time horizons depending on the well.

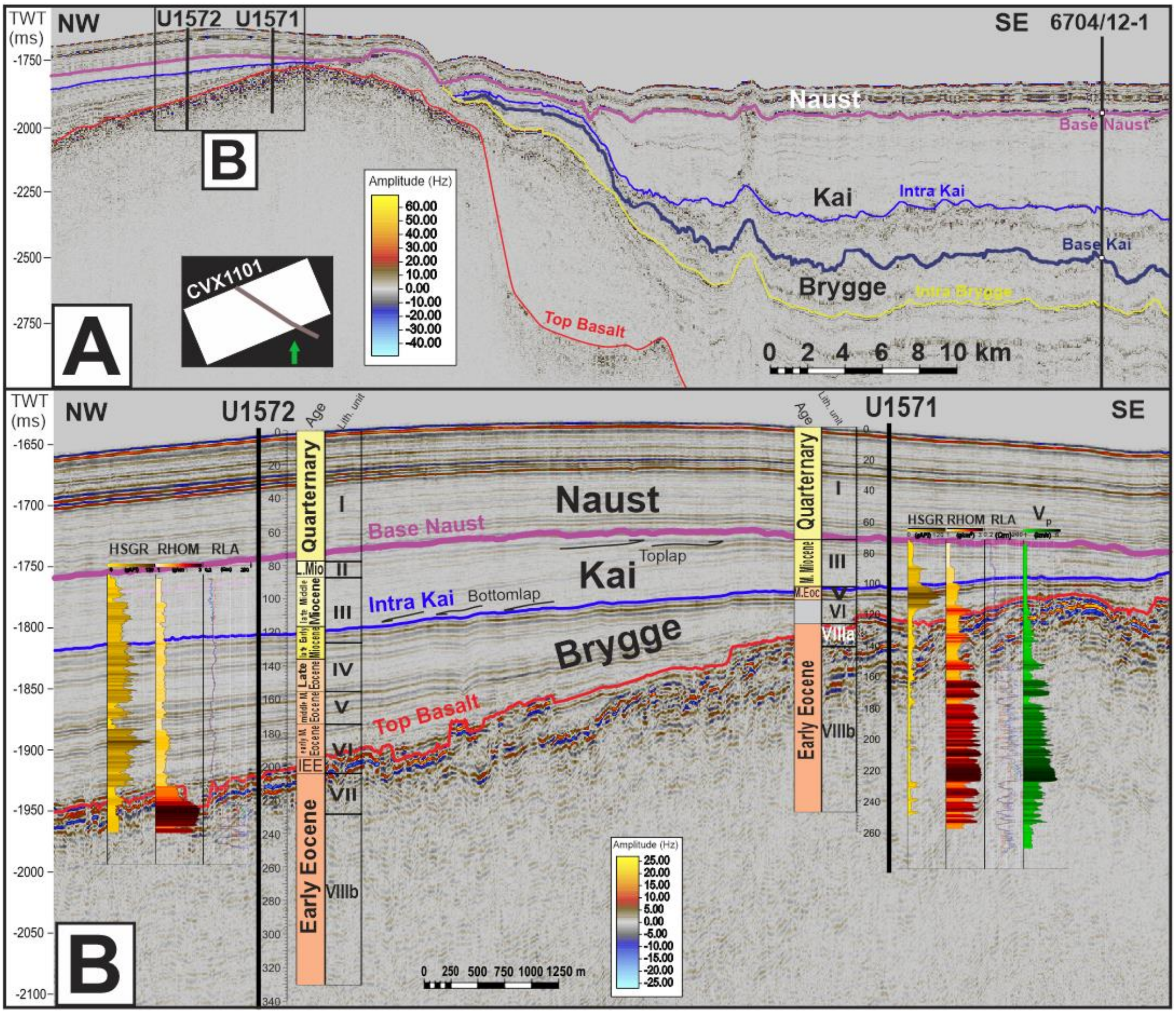

Figure 4.1. The stratigraphic correlation between IODP wells U1571 & U1572 and saga petroleum well 6704/12-1. Both profiles are from the same 2D line (CAGE 22-5 2D), which location is shown in Figure 3.1 & Figure 3.2. All the well log and stratigraphic information overlayed on the seismic are from Planke et al., 2023a. HSGR=total spectral gamma ray, RHOM=density, RLA=resistivity, and V_p=monopole p-wave velocity. The blue resistivity is shallow, the green is medium, and the red is the true resistivity.

In U1571 the horizon transitions from Middle Miocene to Middle Eocene, and in well U1572 the boundary is inside an interval of late Early Miocene age. U1572 hints that this could be a Base Kai reflection, but since the surface is continuous from well U1571, where nothing between Middle Miocene and Middle Eocene is present, the reflection is called Intra Kai. Planke et al., 2023b calls it an Oligocene-Miocene Unconformity, but that's a little too specific for the data used here. This interval of Kai is toplapping onto the Naust formation above and downlapping onto the sediments underneath. These sediments could be either Kai or Brygge, but since they exclusively consist of sediments with an age of Early Miocene and older, they are interpreted as part of the Brygge Formation.

Underneath this is the top basalt, which is easily identifiable both on the well log and the seismic. The volcanic unit has been split into upper and lower flow series, and these are unit VII and VIII respectively. Although there are plenty of reflectors below the top basalt, this boundary is hard to define laterally on the seismic. The interpreted Intra Brygge horizon is not present on either of the IODP wells, but it can be found in the Saga Petroleum well. It is not a part of the formation tops imported with the well data, but it has been interpreted because it is a prominent horizon, and it has been named Intra Brygge, because the bottom of the Brygge Formation from the well data is located below the bottom of the seismic data available.

4.1.2 Well Logs

The well logs are starting beneath the Naust Formation (Figure 4.1). The gamma ray appears relatively low down to the Brygge formation, whereafter it increases and peaks, before it decreases down to the top basalt. After reaching the top basalt it stays low except for a few positive fluctuations. All these smaller peaks seem to be connected to low density, resistivity, and velocity values. The density log is low with little variation until it reaches the top basalt. It has a small peak in the Intra Kai transition. Below the top basalt the higher values are continuously interrupted by abrupt intervals of lower density values. The resistivity and velocity logs are following the same peaks and troughs of the density log both above and under the top basalt. Aside from these similarities, the U1571 well log shows a clear transition to the basalt sequence, whereas the same transition on the U1572 well log is a bit more gradual and smaller sequences of higher gamma ray, lower density, lower resistivity and lower velocity are present.

4.2 Igneous Facies

The 4 different igneous seismic facies (SDR’s, landwards flows, lava delta, and inner flows) described in Table 5 can be identified on all crosslines in the data. An interpretation example of these facies is shown in Figure 4.2.
Most seawards are the SDR’s. They are laterally continuous and flat reflectors (ignoring their tilt), toplapping the sediments above them in a landwards direction on the highest section,

and they slightly diverge seawards. In places, the top is very rough and faulted and it has a positive reflection coefficient. The bottom is smooth and continuous with a negative reflection coefficient. The transition between the SDR's and the landwards flows is very smooth, meaning that the sharp transition on the figure is only approximal and should be viewed as a transition zone. In this zone the tilt is shifting landwards, and the layers stop diverging.

The landwards flows (Figure 4.2) are also rather linear and continuous, but towards the escarpment the interference seems to increase a lot, meaning that the layers are probably thinning or pinching out. They toplap the overlying sediments in a seaward direction, the top is faulted and discontinuous at places, and they transition directly into the lava delta.

The lava delta (Figure 4.2) is characterized by low amplitudes of chaotic structure, occasionally cut by reflectors of higher amplitude and steeper slope. The bottom has a negative reflection coefficient, and it is wavy in places. The delta front is occasionally slumped or collapsed.

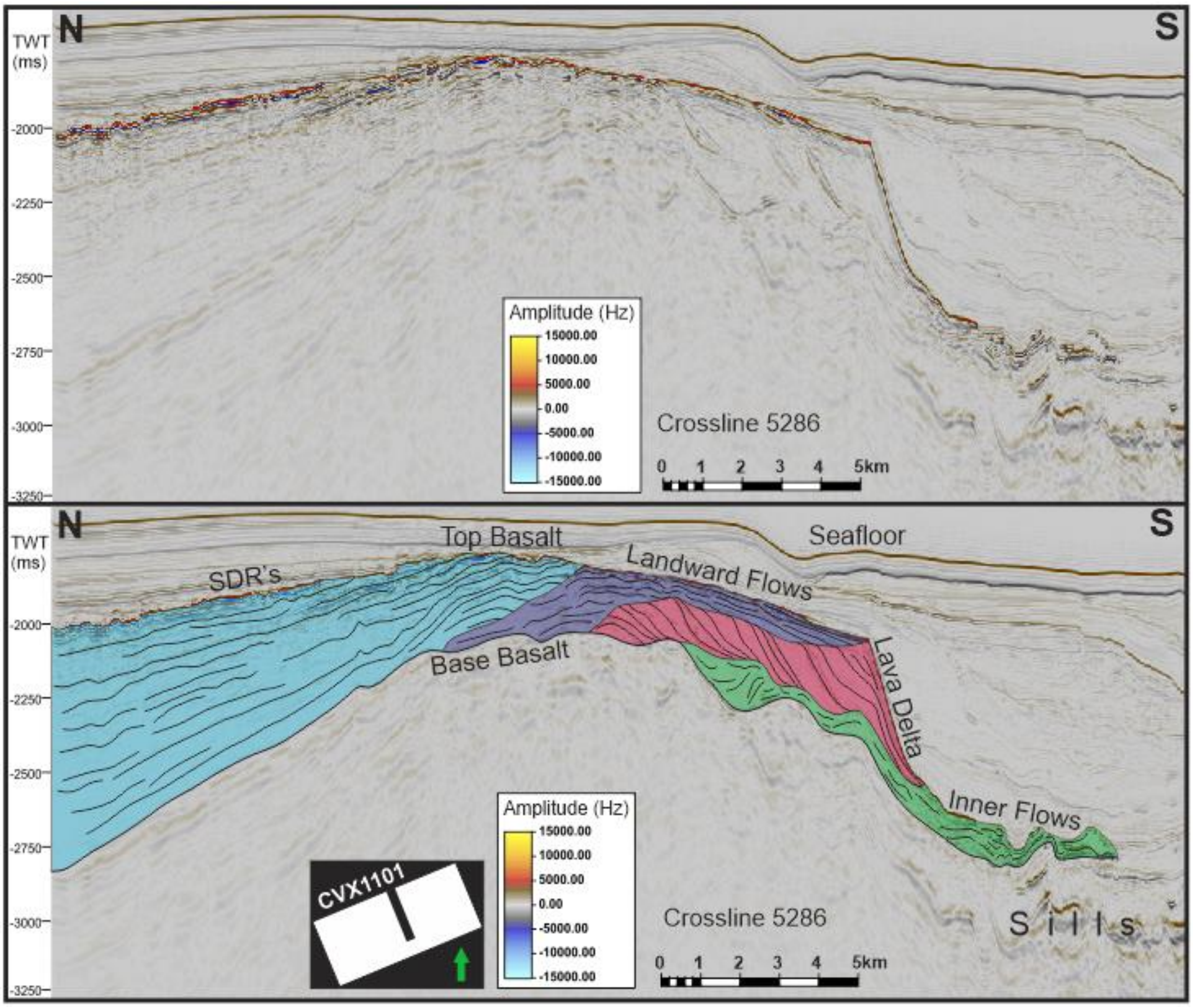

Figure 4.2. Uninterpreted (top) and interpreted (bottom) seismic profile across Skoll High (crossline 5286 from the CVX1101 3D cube in Figure 3.2) showing the interpreted different igneous seismic facies described in Table 5. The location of the profile is shown on Figure 4.4 and Figure 4.5.

The Inner flows (Figure 4.2) are chaotic, disrupted, and hummocky reflections are mainly located beneath the escarpment. The top is discontinuous, rough and has a positive reflection coefficient. The bottom has a negative reflection coefficient, but it is often very hard to identify. The inner flows form 3 major ridges which are described later.

4.2.1 Pitted surface

An area that stands out from these facies is the pitted surface (name adopted from Planke et al., 2017) shown in Figure 4.3, Figure 4.4, Figure 4.5, and Figure 4.6. The higher resolution CAGE 22-5 3D cube is reaching into this area. A spectral decomposition of this data along with seismic examples can be viewed in Figure 4.3. There seems to be two areas of different characteristics dividing the cube roughly over the middle. The western part belongs to the pitted surface, and it is plastered with pits of irregular shapes and sizes. In between the pits more continuous segments can be found. The pits have diameters from 15 m to 300 m, although most is between 30 m and 100 m. Their depth is consistently at 10-15 ms One Way Traveltime (OWT). The top basalt is disrupted by these pits, but in between pits, the reflectors are flat and continuous, some with lobate structures. Some 3-4 reflectors with strong amplitude and similar thickness can be recognized below the top basalt, before the amplitude quickly wanes and appears as faint semichaotic structures. Several sections of high amplitude can be seen on the seismic in between the pits, and they appear as bright colors on the spectral decomposition. These likely constitute lava flows according to Lebedova-Ivanova et al., 2023.

4.2.2 Faulted domain

The eastern part (Figure 4.3) looks considerably different. Both lava flows and pits seem to be gone and replaced by a faulted surface. The big faults have a displacement of up to 17 ms (OWT), but several smaller faults are apparent on the figure. Vertical features of slightly higher amplitude can be seen above the bigger faults. Between the faults, the reflectors are dipping, straight, and continuous.

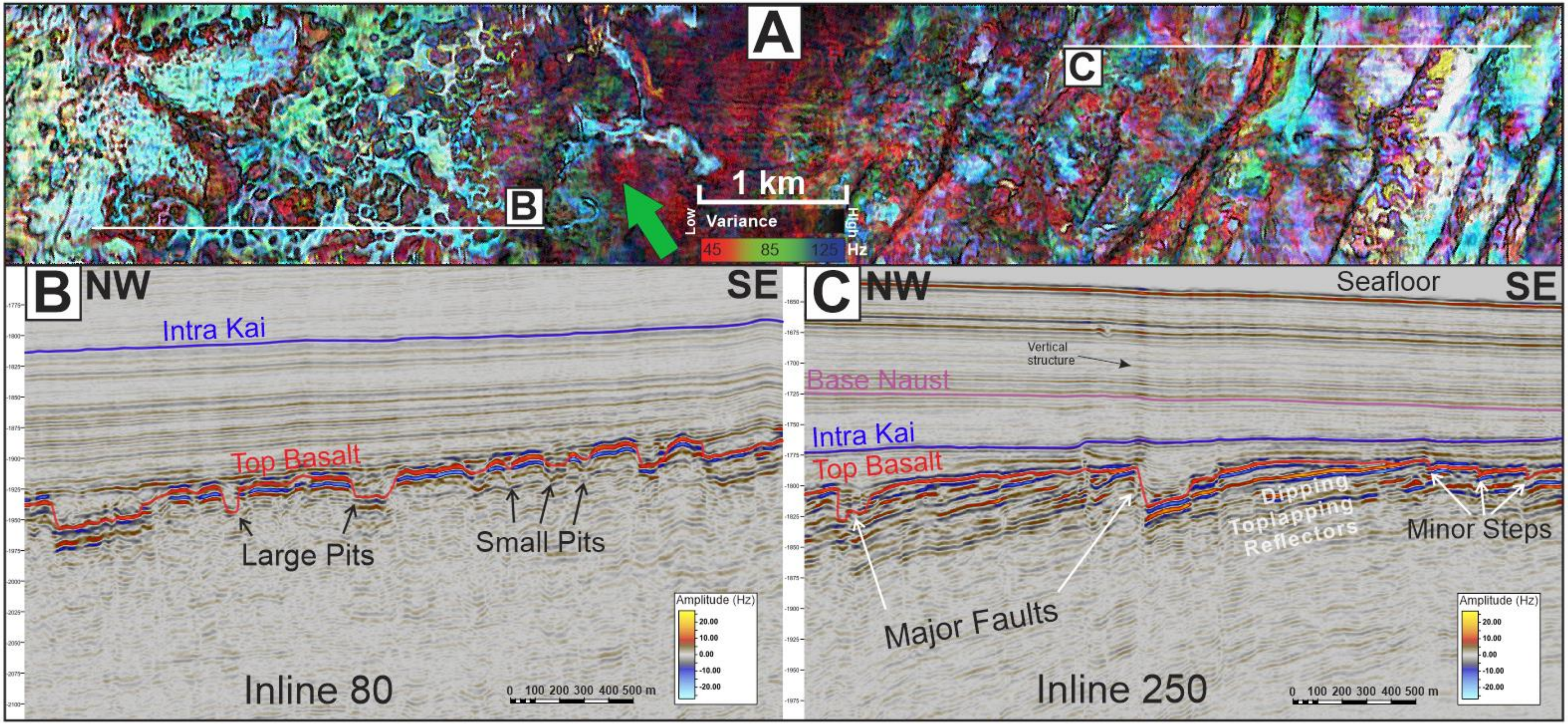

Figure 4.3. CAGE 22-5 data showing the details of the pitted surface and the faulted eastern part. A shows the spectral decomposition that was mentioned in the methods and used by Lebedova-Ivanova et al., 2023. B shows a seismic profile from the western pitted surface, and C shows a seismic profile from the eastern faulted surface.

The depth beneath the top basalt with high amplitudes are considerably higher here and typically reach a thickness of 60 ms, rather than the 30 ms observed in the western part. The top of the basalt is toplapping the sediments above towards the east.

4.3 Top Basalt

The main interpretation in this study is the top basalt shown in Figure 4.4. A first draft was created exclusively looking at the seismic data, and then a reworked version developed incorporating variance and RMS (root mean square) amplitude attributes (Figure 4.5) and GSD (General Spectral Decomposition) (Figure 4.6). Looking on the surface in TWT (Figure 4.4), an array of lineated depressions can be seen crossing the high, some being more obvious than others (denoted with blue dotted lines). The two largest of these spans most of the way from the top of the data down to the escarpment, and these are shown in the seismic inlet on 4.4A. This shows that the structures are disrupting the top basalt by cutting off the otherwise continuous layers on both sides of the features. Furthermore, it looks to be infilled later, as the reflections inside the features also terminate against its sides. These features are recognized by Planke et al., 2017 as channels cut by flowing water and based on this, the smaller features looking similar have also been interpreted as channels. The smaller channels can be quite hard to identify on the seismic because of the resolution (Table 1). Therefore, they have mostly been identified with the GSD in Figure 4.6 and then picked on the seismic afterwards.

On Figure 4.6 the channels are again highlighted. This version of the data is very good for showcasing the channels, which mostly appear as strings of darker colors compared to their immediate surroundings. In several places they are merging towards the escarpment, but they all seem to terminate before the escarpment. The line of their termination is shown on the figure, and it lies just behind the escarpment. Since the number of channels on the western end of the escarpment is very low, the line is discontinued here.

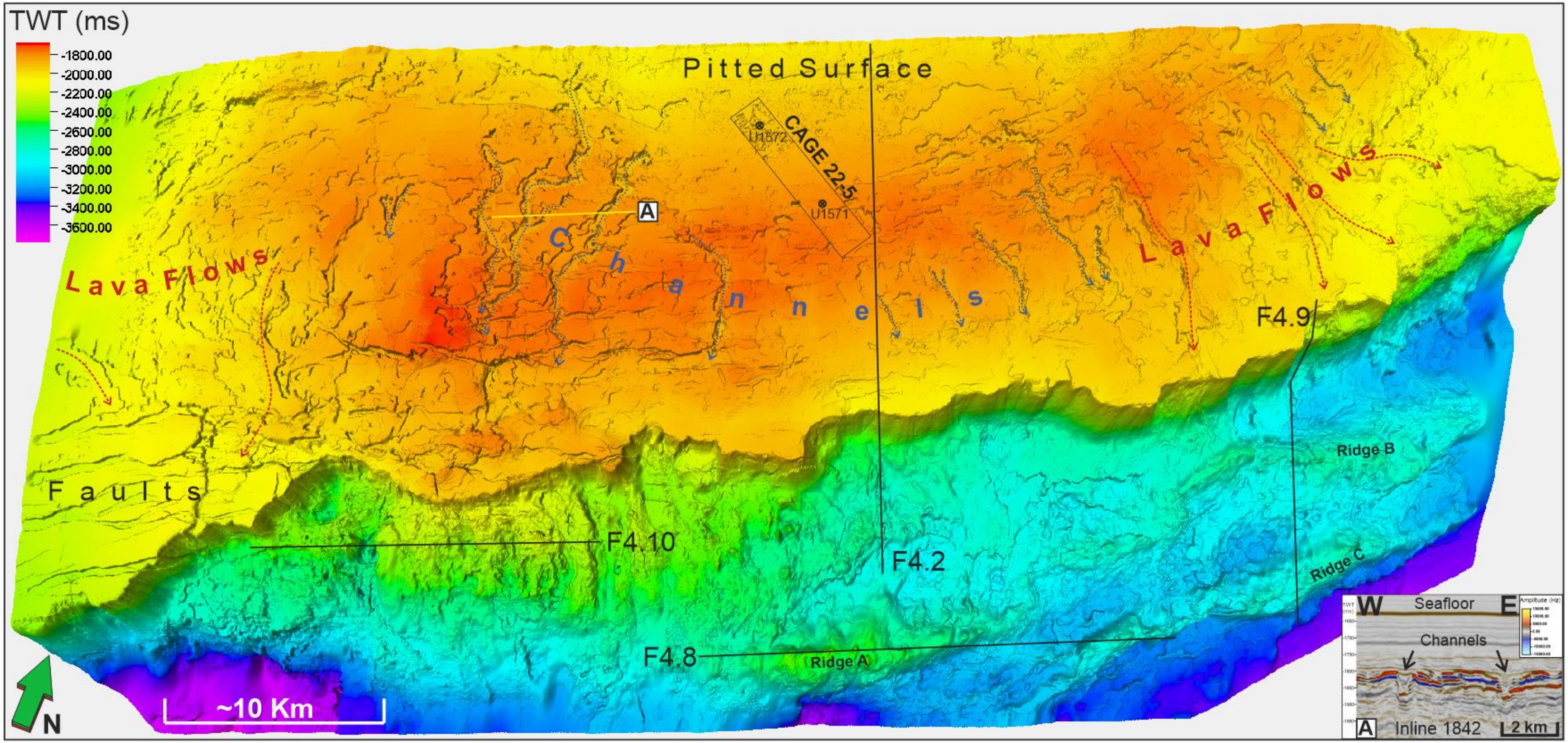

Figure 4.4. The top basalt surface (from the CVX1101 3D cube) shown in a 3D view in Petrel with a vertical exaggeration of 5. The layout of the figure is heavily inspired by Planke et al., 2017, and the names of the ridges is also from this article. F denotes the figure number reference and A is inline 1842 from the CVX1101 3D cube.

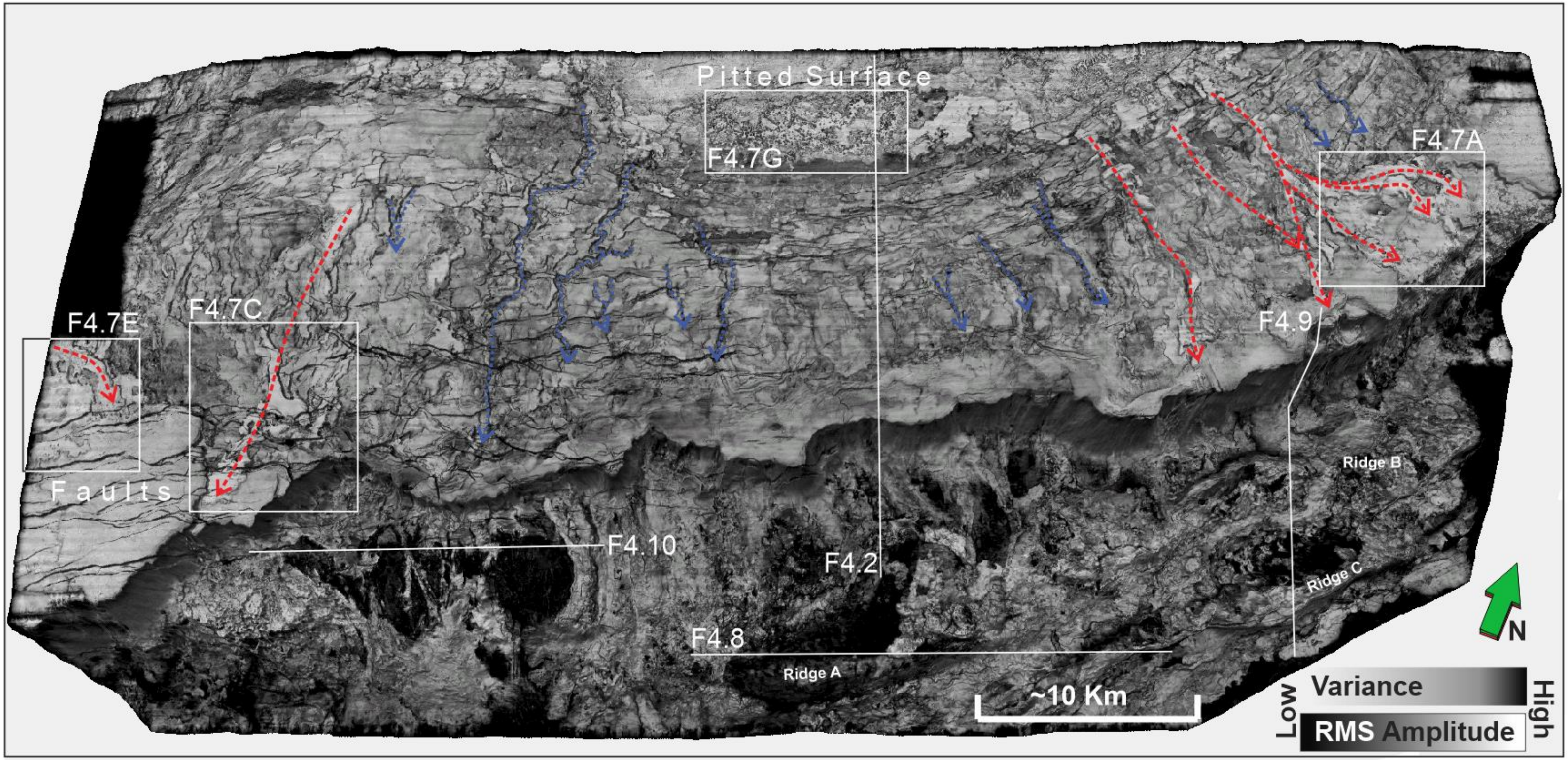

Figure 4.5. A 3D view of the top basalt (from the CVX1101 3D cube) in Petrel showing the variance and RMS amplitude attributes with a vertical exaggeration of 5. The blue llines are channels, and the red lines are lava flows, just like in Figure 4.4. The dark patches beneath the escarpment are areas of low amplitude. The colorscale of the RMS amplitude is black to white, and the scale of the variance is completely transparent to completely black. F denotes the figurenumber. This figure is heavily inspired by Planke et al., 2017.

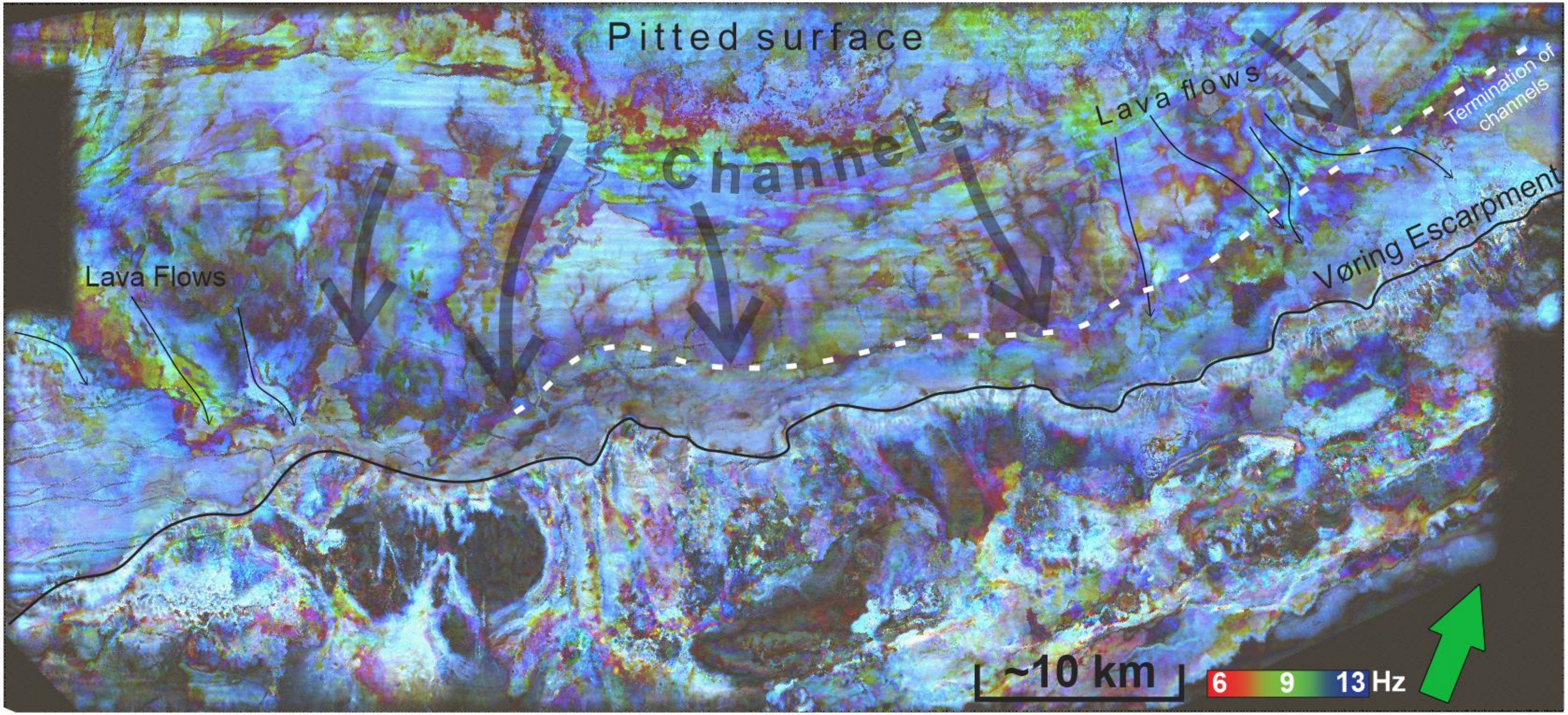

Figure 4.6. The spectral decomposition of the CVX1101 cube shown along the top basalt. The large transparent arrows show the direction of the numerous channels reaching for the escarpment. The dashed line marks the apparent termination of the channels.

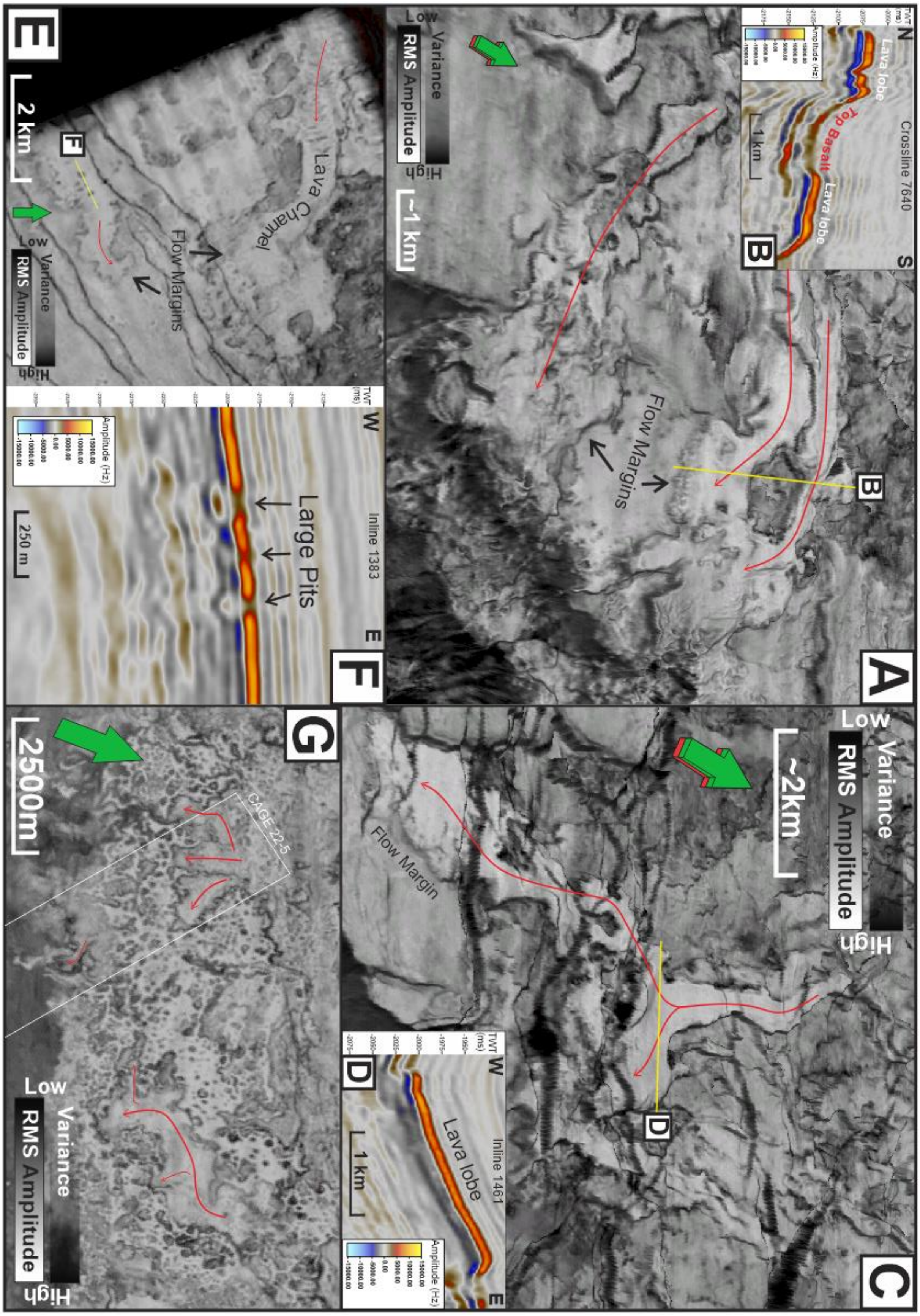

Figure 4.7. Highlights of some of the most pronounced lava flows from the variance and RMS amplitude attributes on the topbasalt surface from the CVX1101 3D cube. Locations can be seen in Figure 4.5. A and C are shown in 3D view with a vertical exaggeration of 5. B is crossline 7640, D is inline 1461, F is inline 1383, and they are all from the CVX1101 3D cube.

4.4 Flow Structures

Several lobes of high RMS amplitude can be observed in the vicinity of the escarpment in Figure 4.5. They are aligned in the same general direction as the channels, meaning somewhat perpendicular to the escarpment. They are easiest to identify with the combination of 3D effect and RMS amplitude in Figure 4.5, because their amplitude and topographic height make them stand out from their surroundings. On Figure 4.6 they are mostly depicted by bright blue colors. The major lobes are presented in Figure 4.7. These are all recognized as lava flows by Planke et al., 2017 and shall henceforth be called hereby.

Figure 4.7A shows at least 3 distinctive flows. The 2 northernmost flows look to be coherent and massive with lobate crenulated margins. They are clearly identifiable on the seismic (Figure 4.7B), where they appear as high-amplitude reflectors standing out from the top basalt around them. The reflectors under the flows seem weaker a relation to the area between the two flows. The southernmost flow is more widespread and seems to split up into minor flows. The flows are about 7 km long.

Figure 4.7C shows a big lava flow splitting up into at least 2 flows. The margins look somewhat lobate, and the top of the flow appears remarkably flat. On the seismic (Figure 4.7D) it appears as a continuous, high-amplitude reflector. Also here, the reflections directly below the flow seems weaker, and it also looks like they are interfering a lot. The flow is about 2 km across in its widest part, and it stretches for no less than 10 km.

Figure 4.7E shows a well-defined lava channel, and an additional flow coming from outside the data coverage. The lava channel is 700 m across, the visible part of it stretches for 3 km, and small outbreaks can be seen underneath it. On top of the other flow, at least 5 pits can be seen of which 3 are highlighted on the seismic in Figure 4.7F. They look to be about 50-100 m wide and up to 12 milliseconds (OWT) deep, much like the pits from section 4.2.1. (Figure 4.3).

Figure 4.7G is an overview of the pitted surface and apart from the pits, lava flows can also be identified here. The most prominent eastern flow is some 3,5 km long, 1 km wide, and the margins look mostly braided. The three smaller flows reaching into the CAGE 22-5 coverage are about 1 km long and 500 m wide.

4.5 Chimneys

Three major ridges stand out south of the escarpment on Figure 4.4. They are aligned in roughly the same direction as the faults described later and have a length of about 10-15 km. The names are adopted from Planke et al., 2017. Ridge A, B, and C all show similar features, and they are also shown in Figure 4.8 and Figure 4.9. Reflectors above them are deformed to a positive bulge or completely gone in a chaotic structure. Inside these vertical structures of disturbed sediments, several pockets of higher amplitude can be found. The layers inside the ridges are parallel to the sides of the ridges, which means they are almost vertical. It seems that all the layers above the ridges are affected, including the seafloor. The pockets with high amplitude are mainly restricted to the interval between Intra Kai and Base Naust. Significant polygonal faulting is located between the ridges from below Base Kai to above Intra Kai, further depicted by the insets of the Base Kai surface in both figures (Figure 4.8 and Figure 4.9). 4 possible minor chimneys located above the low amplitude area next to Ridge A are highlighted in Figure 4.8. They also display a deformation of the layers above, although less so than the major chimneys. They seem to be coincident with faults cutting all the way from Base Naust, so the displacements could also be explained by this fact, but this is uncertain. In both cases any fluid or gas seeking to escape towards the surface could likely utilize these features to do so.

4.6 Areas of low amplitude

On Figure 4.5, some major areas of dark color can be spotted beneath the escarpment. They are all a consequence of low RMS amplitude, and some of them seem to be connected to ridge A and C. These can be seen on the seismic in Figure 4.8. Here, there is about 6 km along the top basalt with abnormally low amplitudes, where the top basalt seems to disappear into faint reflectors. This seemingly acoustically masked area continues downward until it reaches the strong saucer shaped reflections that are characteristic for sills. The same low amplitudes are repeated for a couple of kilometers directly over Ridge A, except no masking seems to be taking place here, and the reflectors underneath seems a bit distorted and forced upwards.

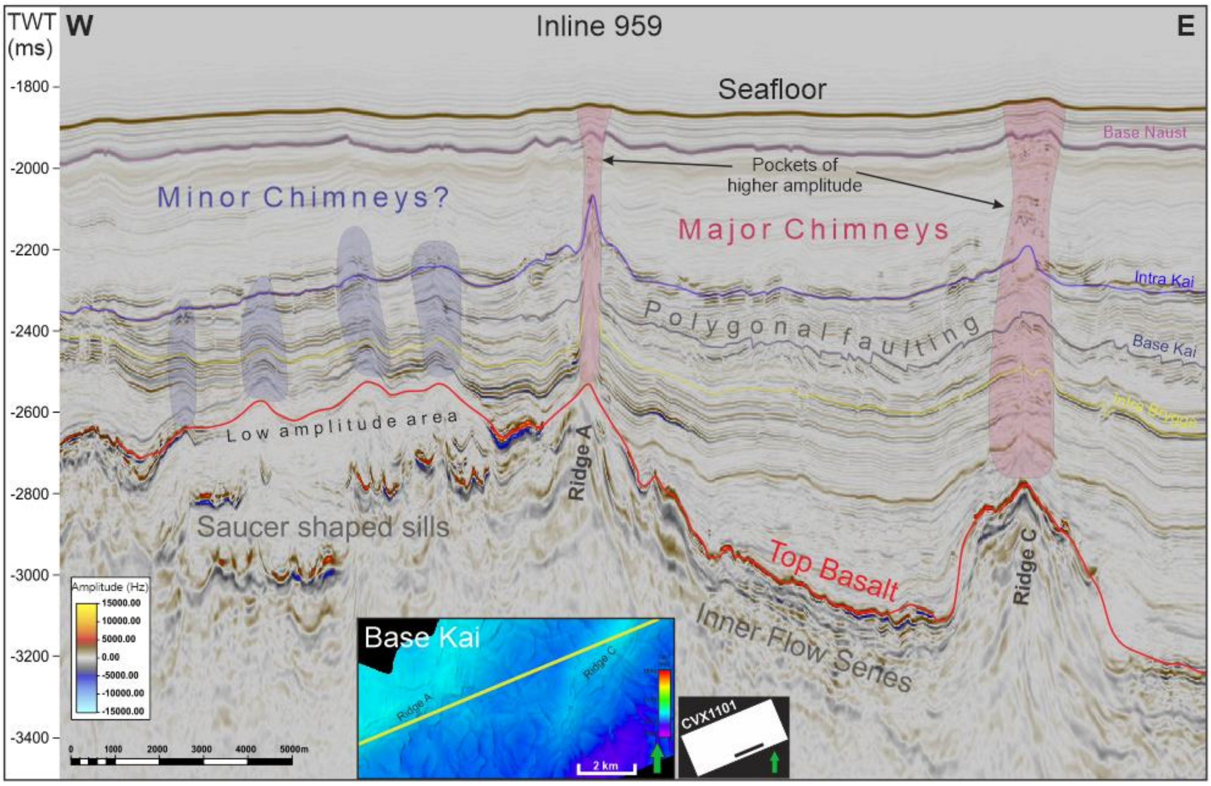

Figure 4.8. Seismic inline (Inline 959 from the CVX1101 3D cube in Figure 3.2) over ridge A and C and the area of low amplitude closest to ridge A. The inset in the bottom shows the polygonal faulting on the Base Kai surface, and the yellow line therein shows the location of the seismic profile. The location is shown on Figure 4.4 and Figure 4.5.

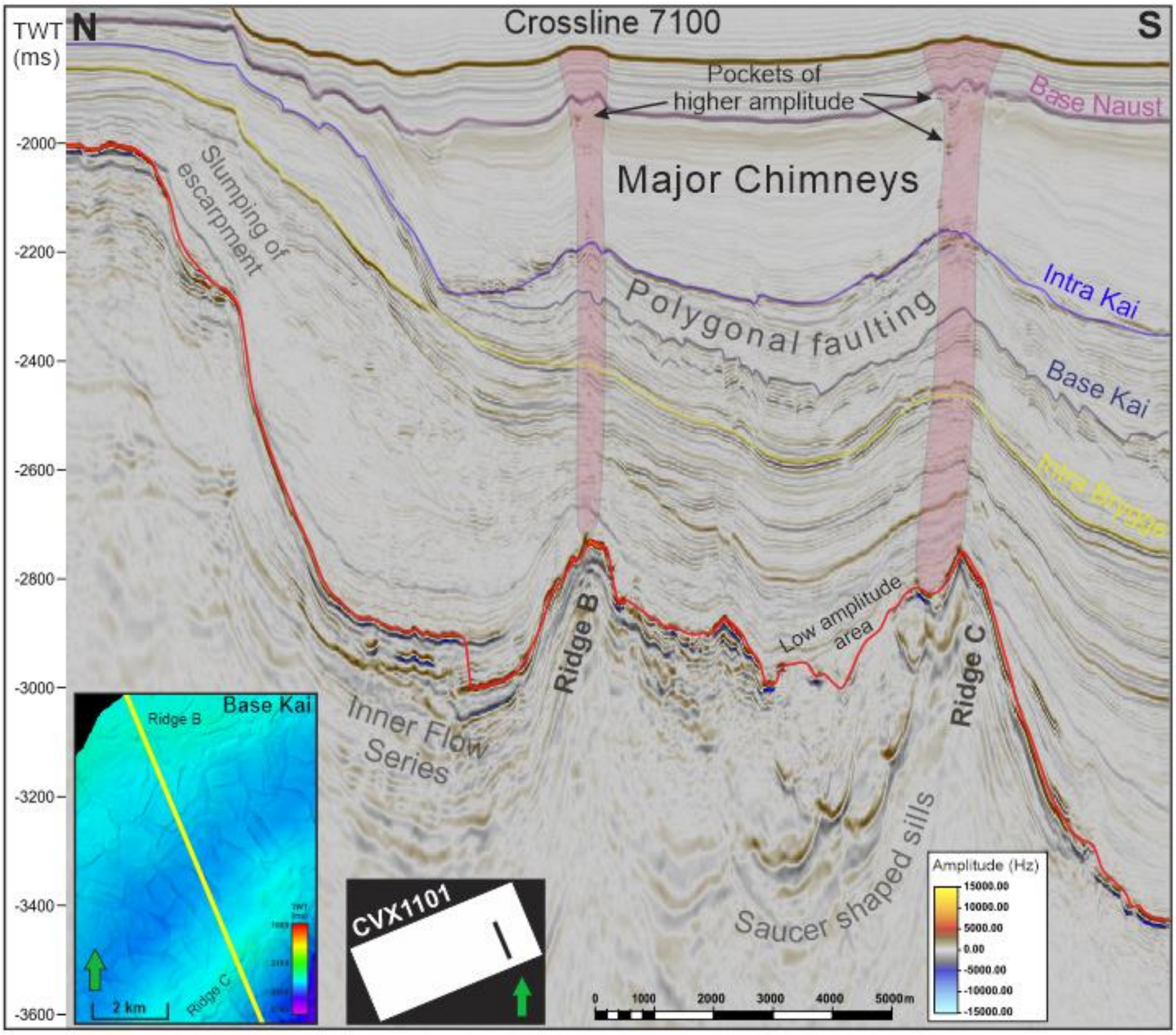

Figure 4.9. Crossline 7100 from the CVX1101 3D cube (Figure 3.2) across the Vøring Escarpment, Ridge B, and Ridge C. Location is shown on Figure 4.4 and Figure 4.5. The inset in the bottom left shows the polygonal faulting on the Base Kai surface, and the yellow line therein shows the location of the seismic profile.

In Figure 4.9, another area of low amplitude is observed next to Ridge C. Here, there is also an acoustically masked area reaching down to several saucer shaped reflections with strong amplitudes. Both cases are located in the vicinity of a ridge with a clear chimney structure.

4.6.1 Sediment window

One of the areas of low amplitude that is not in the vicinity of any of the ridges, is the one shown in Figure 4.10. On Figure 4.5 it looks like three distinctly darker areas in the southwestern part of the data beneath the escarpment. The westernmost area (Figure 4.10) has a slightly higher amplitude than the other two, and beneath it are saucer shaped reflections interpreted as sills. The middle area has distinctively low amplitudes, and beneath it are strong saucer shaped reflections also interpreted as sills. The easternmost area has the same low amplitude as the middle area, but underneath it there are no sills. The low amplitude area is ending downwards into flat continuous reflections of medium amplitude. On the seismic (Figure 4.10) it is clear that the respective areas are broken up by small segments of high amplitude. In the low amplitude areas, the positive reflection coefficient characteristic of the top basalt surface is sometimes replaced by a negative reflection coefficient. This is happening in the areas marked as trough structures on the figure (Figure 4.10), where an overlying reflector seems to cut down into underlying reflectors. The relatively flat and continuous layers beneath are thus onlapping the trough structures. Several other trough structures making up grooves perpendicular to the Vøring Escarpment can be observed on the surface in Figure 4.4 and on the seismic in Figure 4.10. These have a positive reflection coefficient, and some have the high amplitude that is so characteristic for the top basalt. Planke et al., 2017 has interpreted this area to be a sediment window with lava streams and debris flows of volcaniclastic material flowing down from the escarpment in channels between the topographic highs (section 1.4).

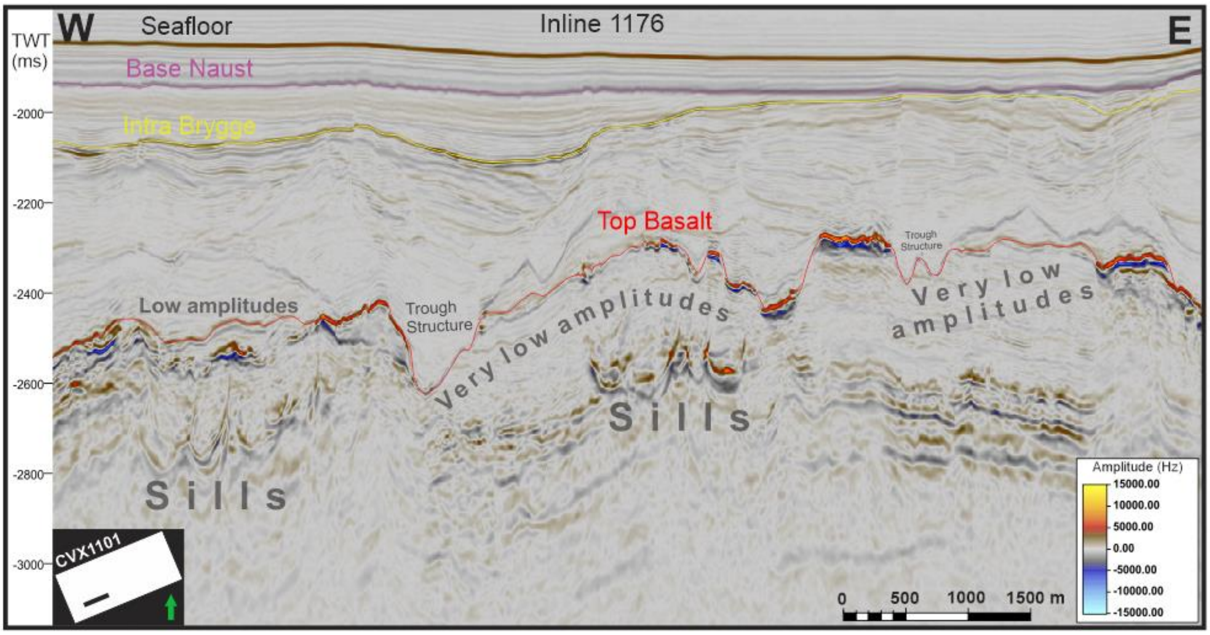

Figure 4.10. Seismic profile (Inline 1176 from the CVX1101 3D cube in Figure 3.2) across low amplitude areas beneath the escarpment. The location is shown on Figure 4.4 and Figure 4.5.

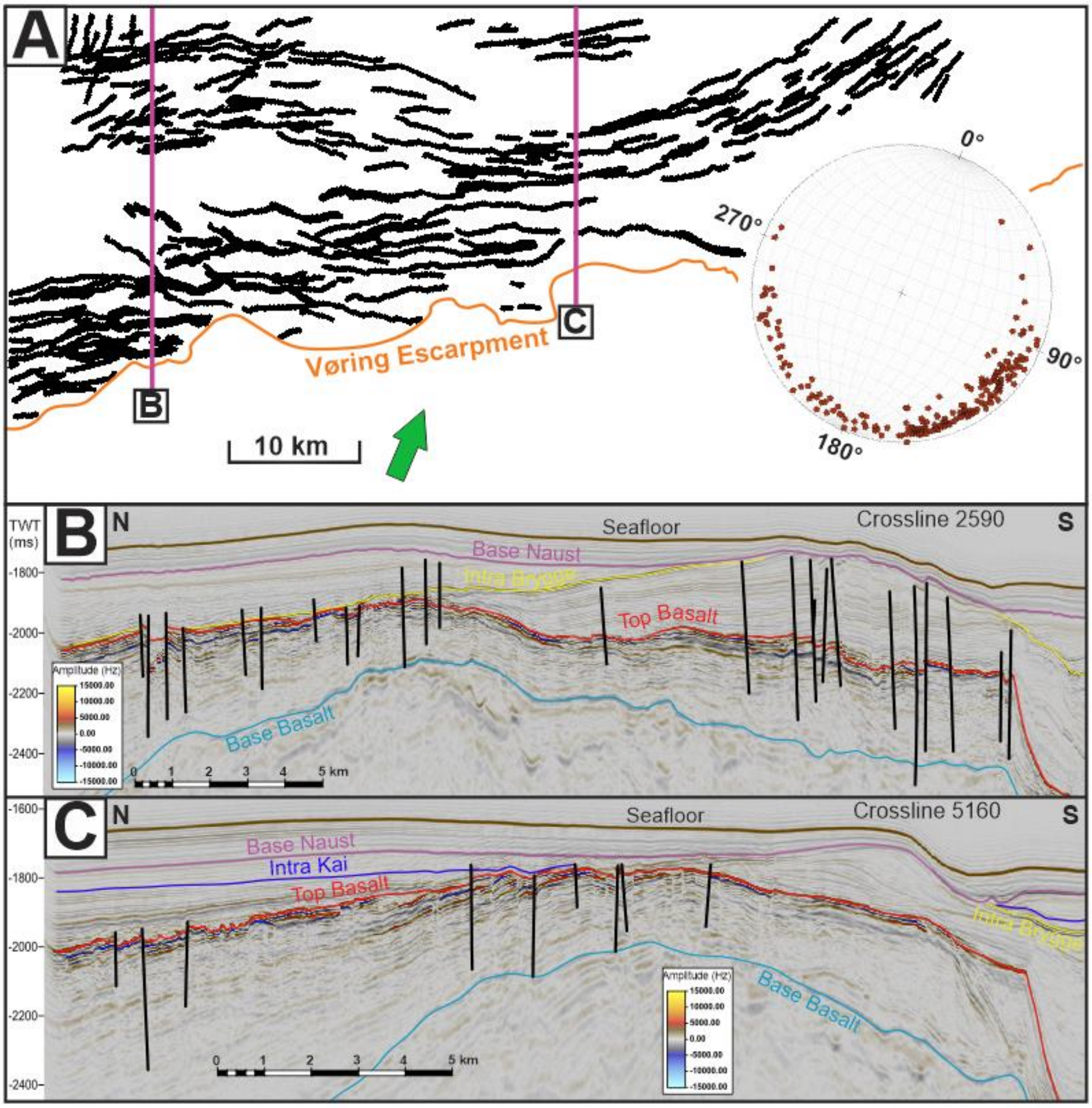

Figure 4.11. 212 manually picked fault planes crossing the Top Basalt Horizon are shown in A in a 3D view from above. The extent of A corresponds to the data coverage of the CVX1101 3D cube. The dots in the equal area stereonet are the poles to the fault planes, and the stereonet has been tilted so it aligns with the north of the faults in the figure. B is seismic crossline 2590 from the CVX1101 3D cube and C is crossline 5160 from the CVX1101 3D cube. They both showcase the faults crossing the top basalt over Skoll High.

4.7 Faults

The picked fault planes inside the CVX1101 data cube can be seen on Figure 4.11. 212 faults have been picked and they are all located north of the Vøring Margin. Only the faults crossing the Top Basalt have been picked. Although several faults in the southwestern area are continuing south of the escarpment, they are very hard to track, because there is generally much more discontinuity in this area than north of the escarpment. Almost all faults with exception of the southwestern area don’t reach much into the sediments over the top basalt, the longest reaching into the Kai Formation. The vast majority of faults are located parallel to the escarpment, which means they have a strike resembling a SW-NE direction. They have a relatively high dip, the lowest being 60 degrees, and they seem to follow the direction of the ridges underneath the escarpment. Most faults have a displacement of 5-15 ms OWT, the faulted area in the southwest (Figure 4.4 & 4.5) has displacements up to 30 ms OWT, and a few of the major faults along the escarpment reach a displacement of 50 ms OWT.

4.8 Base Basalt

The base basalt has been interpreted and the results are shown in Figure 4.12. Due to general imaging problems beneath the top basalt, the base basalt is sometimes very difficult to interpret. It has only been interpreted where it was clearly identifiable on the seismic, which is mostly north of the escarpment. This is not the same extent as the top basalt, which will be discussed later.
Figure 4.12A shows Skoll High as more or less the same positive topographic shape as can be seen on the top basalt. A faint expression of the Vøring Escarpment can be seen, but the middle part seems to have a consistent slope away from Skoll high. Where the top basalt is spanning 600 ms TWT north of the escarpment, the base basalt spans over 800 ms TWT, and Skoll High seems to be a little higher relative to the surroundings than on the top basalt. Some linear features can be seen over some parts of the high as well as close to the escarpment. These are highlighted in Figure 4.12B, and they are perpendicular to the faults that are also crossing the base basalt. These faults seem to follow the same strike as those that cut the top basalt, the difference being that there are significantly fewer faults cutting the base basalt. On the high itself, the variance surface shows mostly faults, but when

looking closer to the escarpment, it becomes a lot more chaotic. The line for this transition is approximately following the inner edge of the lava delta. Any channels as the main ones from Figure 4.4 cannot be seen on the base basalt except for a small channel-like feature in Figure 4.12C. This feature follows the trend of the main channels, but unlike any of the channels on the top basalt surface, it appears to reach all the way to the escarpment.
The area around the escarpment is generally rough and the “eggbox -network” described by Maharjan et al., 2024 is present and can be seen in Figure 4.12C.
The time thickness between the top basalt and the base basalt surfaces can be seen in Figure 4.12D, and it serves as a good indicator of the differences between the two surfaces. The faults in the south-west and the two main channels from Figure 4.4 can clearly be seen here, because they are only present on the top basalt surface. If the two surfaces were somewhat similar in the areas where these features are present, the time thickness would be constant. A lot of the faults and channels cutting the top basalt is seen on this map (Figure 4.12D), and in the top of the figure there is a large area where the time thickness is increasing seawards. Blue areas can also be spotted on the right and left side of the figure. This is important because in addition to giving a good idea of the differences between top and bottom basalt, the time thickness between these surfaces also gives a hint to the basalt thickness. It is not a direct relationship since the different velocities of the basalt and sediment layers between top and bottom are not defined continuously through the sequence. The blue areas towards the edges of the data coverage therefore suggests that the basalt thickness is increasing away from Skoll High which corresponds with Abdelamak et al., 2016b, and Planke et al., 2017. The volume of the interpreted basalts is calculated to be 1500 km^3, assuming that the average velocity of the basalt sequence is 4244 m/s and neglecting the interbasaltic sedimentary sequences (see section 3.9 for calculation). Additionally, this accounts only for the area where the base basalt is interpreted, which means it is probably an underestimation, since the top basalt can be followed much further.

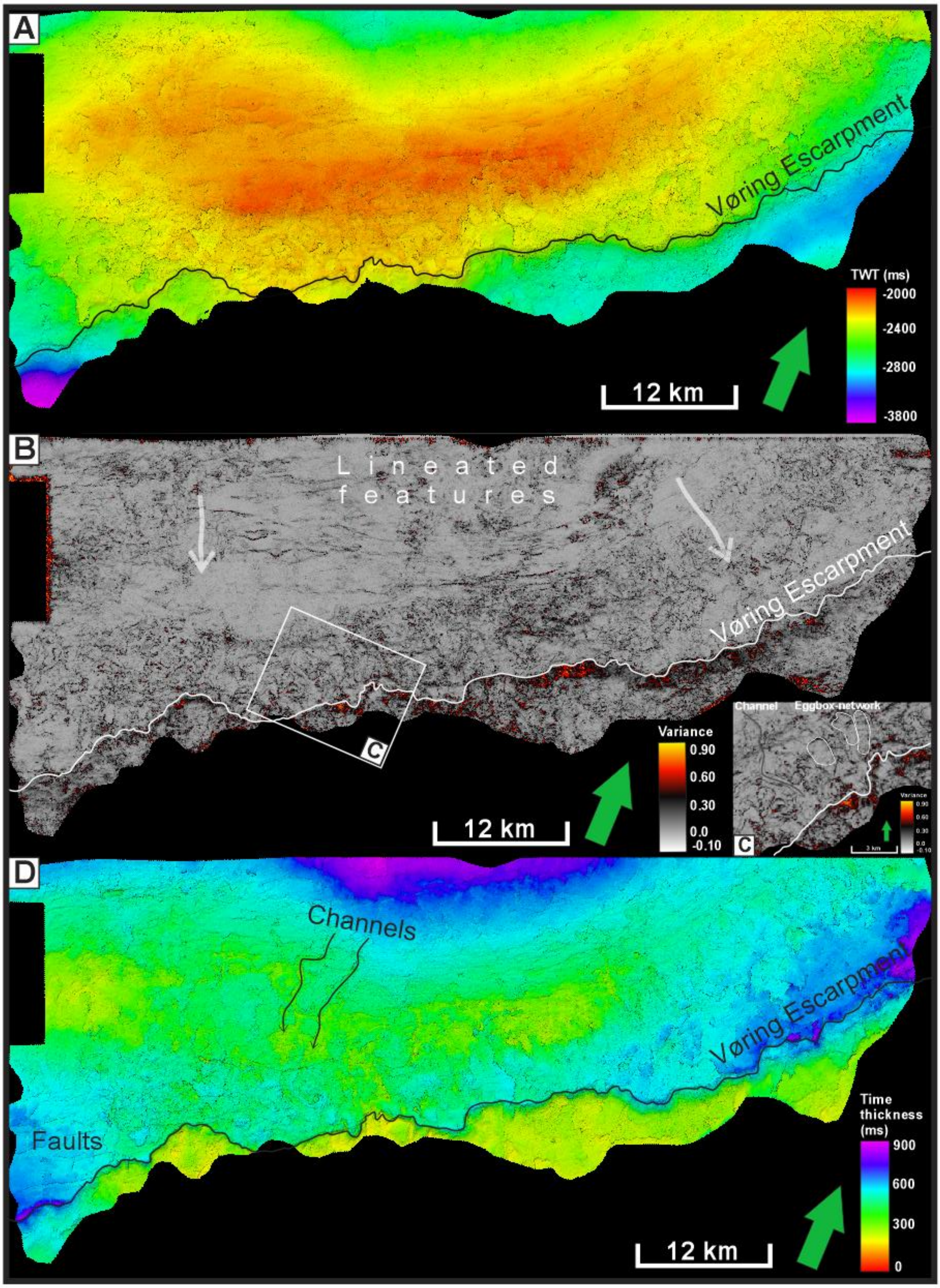

Figure 4.12. A shows the Base Basalt surface in TWT, B shows the base basalt surface with the variance attribute, C shows a highlight of the features near the escarpment, and D shows the time thickness between the top basalt and base basalt surfaces where they are both interpreted. All are shown in 2D, all are from the CVX1101 3D cube, and the line marks the Vøring Escarpment as it is on the top basalt surface.

4.9 Anomalous observations

4.9.1 Southeastern reflection

Figure 4.13 highlights a particular reflection in the southeastern corner of the CVX1101 3D cube. It mostly follows the southern edge of ridge C, but to the east, it crosses over to the other side of the ridge. On the side of the ridge where it is tilting, it has a width of about 1 km. Where it flattens in the end points it has a width of about 2 km, and it has a total length of about 25 km. On the seismic (Figure 4.13) the reflector has a strong amplitude that fades out abruptly to either side. Figure 4.13A shows that the ends of the reflection are bending upwards as they fade out in both directions, and towards the north, it seems to onlap ridge C. In 4.13B the reflection has a steeper slope and a smaller amplitude, but it still appears to onlap ridge C. In Figure 4.13C no onlap can be found since ridge C does not exist at this point. And the reflection is again flat and strong. In all three seismic sections (Figure 4.13A, Figure 4.13B, and Figure 4.13C) the reflection appears to follow the deformation of the layers above, and a faint continuation of the reflection is suggested in both directions.
This reflection is shown because it stands out with its high amplitude, restricted extent, and abrupt decrease in amplitude at its ends. It took only 1 click for the 3D autotracker tool in petrel to recognize the whole structure, meaning that has a significant amplitude and continuity throughout its extent. No other similar cases were found in the dataset or in literature.

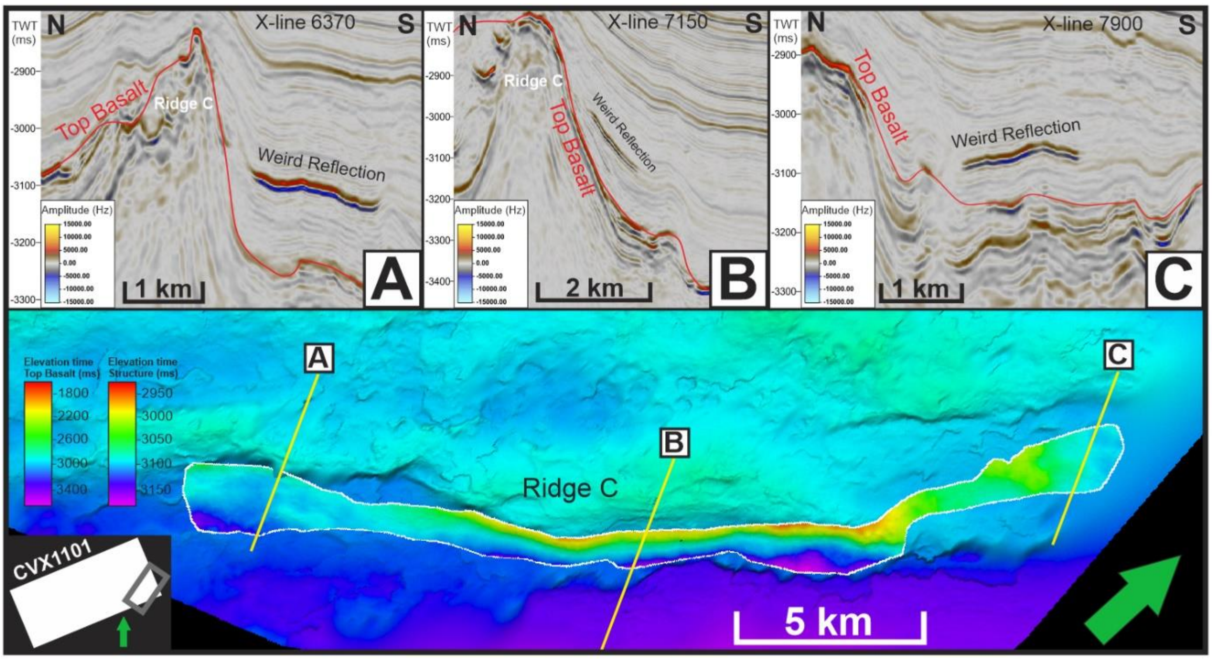

Figure 4.13. The top basalt surface in a 2D view (TWT) overlain by the surface for the reflection (TWT) highlighted in the seismic profiles A, B, and C. This figure shows the southeastern corner of the CVX1101 3D cube.

4.9.2 Northwestern reflection

Figure 4.14 highlights an area with a peculiar reflection in the northwestern corner of the CVX1101 3D cube. On the variance and RMS amplitude attribute overview map (Figure 4.14) two prominent faults cutting through the area can be observed. The darker area that the profiles cross over tells that the picked top basalt surface has a lower RMS amplitude than its surroundings. This can also be viewed on the seismic (Figure 4.14), where the picked top basalt horizon suddenly becomes very wavy, as it breaks off from the otherwise horizontal reflections, with topographic peaks following the faults. The layers above the top basalt are onlapping this wavy reflection, and in between peaks infilling looks to have taken place. On Figure 4.14A, the reflections below the top basalt in between the two faults appear discontinuous, with pockets of medium to high amplitude, and it is almost impossible to follow reflections across the faults. On Figure 4.14B the reflections below the top basalt between the faults are more continuous across the faults, and strings of medium to high amplitude are present. This reflection is peculiar because of its sudden loss of amplitude, increase in sinuosity, and the lack of similar examples in the dataset or the literature.

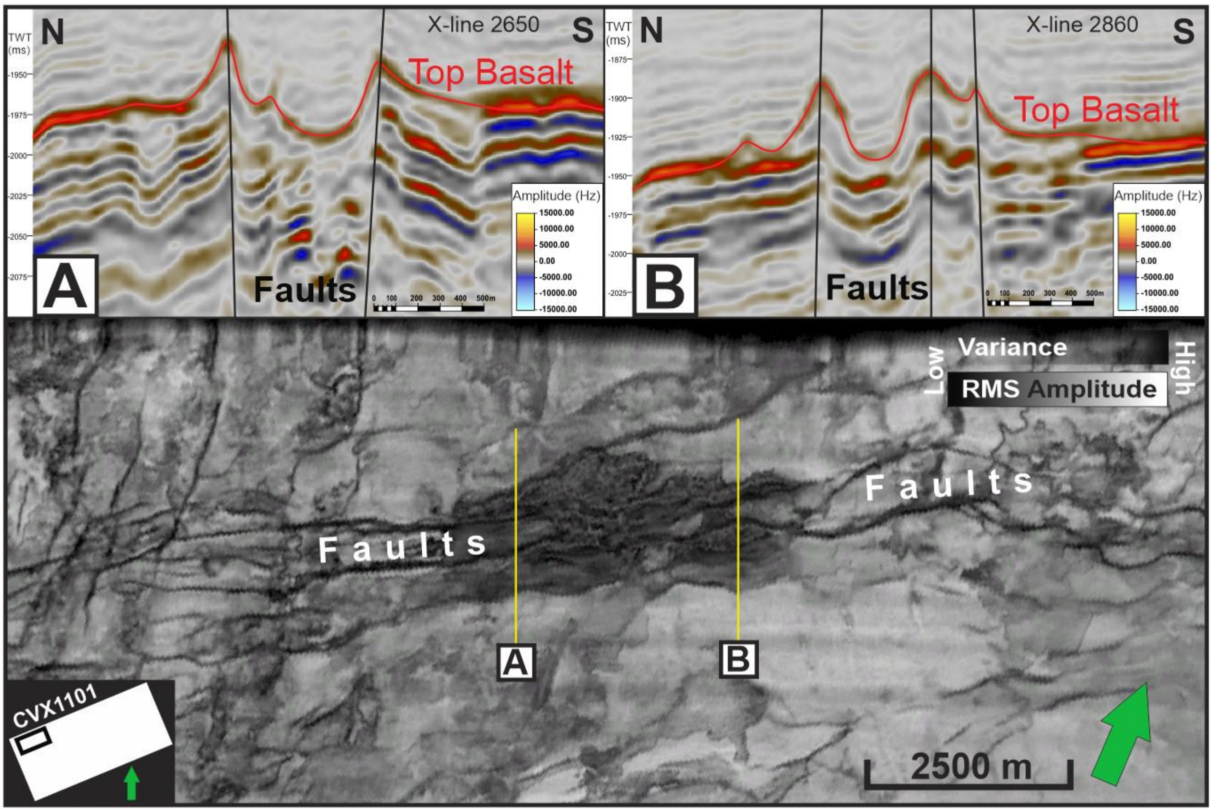

Figure 4.14. Variance and RMS amplitude attributes on the top basalt surface in a 2D view along with the seismic insets A and B highlighting the reflection that creates the dark area between the two profiles. This figure shows the northwestern corner of the CVX1101 3D cube.

5 Discussion

In this chapter, the biggest sources of error connected to the results will be addressed. Afterwards I will discuss the volcanic emplacement processes, possible release mechanisms, and the genesis of the volcanic deposits that were presented in the last chapter. This will be followed by the change undergone to these units after being deposited, and some terrestrial field analogues of the structures observed in the area. Lastly, the potential for carbon storage will be assessed, both regarding the presented results, but also the work of other authors.

5.1 Major sources of error

The most apparent source of error related to this thesis is the picking of the horizons, especially the top basalt. If an error has occurred in the top basalt, it will have consequences for the spectral decomposition of the CAGE 22-5 data (Figure 4.3), the variance and RMS amplitude attribute map of the CVX1101 data (Figure 4.5), the spectral decomposition of the CVX1101 data (Figure 4.6), the basalt thickness map (Figure 4.12D), and the basalt volume calculation (section 3.9 and 4.8). Therefore, great care has been taken when picking this particular horizon. Some places are very easy to pick, showing high amplitude and good continuity, but it's very difficult to be consistent over large areas. The top basalt is only an interpretation and an approximation to the truth, but it has been created by active decisions about how to interpret it. Major decisions made when picking the top basalt is described in section 3.8, including how the top basalt has been picked over the low amplitude areas. These areas will be discussed later, but there is no telling whether the top basalt is even present in these areas. It has been picked anyway to get a coherent surface, and because the anomalies still show up on the RMS amplitude attribute map (Figure 4.5).
Picking the overlying stratigraphic horizons was easier, and an error would cause fewer consequences, but the correlation in Figure 4.1 needs to be addressed, because it is incorrect by design. The Base Naust, Base Kai and Intra Brygge horizons interpreted from the Saga petroleum well on the southern side of the Vøring Escarpment, does not give rise to many errors, since stratigraphic boundaries are defined from the well data, and the horizons are relatively easy to follow. The correlation from the IODP well on the northern side of the

Vøring Escarpment, however, gives rise to several errors, because the well data was not directly available. Consequently, the well data has been overlain on the seismic, which is problematic, because the well data is in meters, and the seismic is in TWT. Optimally, the well data would then need to be stretched and compressed according to the sediment velocity, so it would fit with the seismic data, but since only two fixpoints (Seabed and Top Basalt) were known, this was not really a viable method. This means that the correlation for these wells is only approximate and greatly helped by the interpretations of Planke et al., 2023b (and Lebedova-Ivanova et al., 2023).

Another approximation is the basalt volume calculation from section 3.9, since it is based on an average basalt velocity from the IODP wells, and because the top basalt surface and the base basalt surface do not have the same spatial extent. The basalt velocity that was used comes from two adjacent wells (U1571 & U1572), that do not reach all the way through the basalts and might not represent the velocity of the basalt sequence. This could be improved by having a continuous velocity log through the whole basalt sequence and by knowing the basalt/interbasalt sedimentary sequence ratio through the whole sequence. The basalt volume calculation would also be improved by being able to interpret the base basalt as far as the top basalt, but this has been refrained from, since the base basalt was very difficult to interpret beneath the Vøring Escarpment in the inner facies, and so the basalt volume calculation accounts mostly for the basalts north of the escarpment. The base basalt clearly follows the morphology of the escarpment (Figure 4.12), so this waning in the amplitude of the base basalt is probably related to the increased depth south of the escarpment.

5.2 Volcanic emplacement processes

The igneous facies presented in Figure 4.2 and described in section 4.2 are representative of the data in this study and are also identified throughout the Vøring Marginal High by other authors (Planke et al., 2000, Berndt et al., 2001, Abdelamak et al., 2016b). The SDR's are presumably of "type 1" (inner SDR's) according to section 1.3.3 (Figure 1.6), Eldholm 1989, and Gibson & Love 1989, but this is hard to confirm since only a part of them is included in the data, and the termination into a landwards-tilting fault or the presence of feeder-dykes that could cement this allegation can't be identified. The fact that the SDR's are toplapping the overlying sediments towards the Vøring Escarpment could be due to erosion of the high, but it could also just be the termination of lava flows. However, since the landward flows are also toplapping the sediments above, it seems very likely that erosion of the high has contributed to the toplap. This fits well with the fact that these flows are subaerial (section 1.3.2 and 1.3.3), since it would require a very rapid burial for the high not to be eroded, and furthermore the high is known to have been eroded in Paleocene-Eocene due to uplift (section 2.2.6 and section 2.2.7). The discontinuities on the top of the SDR's and the landward flows likely represent lateral shifts in time due to either erosion, termination of lava flows, or a combination of the two.

The bottom of the lava delta is described as wavy in places (section 4.2 & Figure 4.2), and it's hard to say why this is so. It could be caused by lateral velocity differences in the overlying deposits, it could be a rough original topography at the time when the base basalt was deposited, or it could be the eggbox-network recognized by Maharjan et al., 2024 caused by soft sediment deformation after rapid deposition of several hundred meters of hyaloclastites. The observed chaotic, disrupted reflections of the inner flows (section 4.2 & Figure 4.2) are consistent with the fact that they consist of a mix of fragmented basalt, volcaniclastic rocks, pillow lavas, shallow intrusions, and massive sheet flows (Planke et al., 2017, section 1.3.2)

5.2.1 Volcanic emplacement environments

<u>Pitted Surface</u>

The pitted surface above the SDR's (shown in Figure 4.3) is an interesting area, that might be explained by several processes. The lava rise pits (Walker, 1991 and section 1.2) could fit with the observed structures (Figure 5.1). Being in the size range of tumuli and with depths the same as the thickness of the surrounding lava flow, they would presumably be resolvable in the CAGE 22-5 data in Figure 4.3 (see Table 1 for resolution table), but would likely only fit with the size of the smaller pits observed (section 4.2.1). The main concerns with this hypothesis are the abundance and connectivity of pits in Figure 4.3. It seems unlikely that a lava flow would be this sporadic, patchy, and leave so many spots in various size uncovered. This could on the other hand be explained by Boreham et al., 2018's suggestion that lava rise pits can form when encountering a small pool or a pond of water. The water in the pool would then quench the lava before evaporating, leaving a pit behind once the lava around it starts to inflate. This seems somewhat likely, especially when considering that Boreham et al., 2018 found these structures in conjunction with explosive pseudocraters (discussed later), that also form when lava interacts with water.

Another phenomenon that could explain the structures are collapse pits (Ballard et al., 1979, Hon et al., 1994, and graphic terrestrial examples by Greeley, 1974) created by withdrawal of lava, causing failure of the top of the lava flow when the lava inside is replaced by a cavity. When this happens beneath a tumulus, it will create a pit that might look like those observed in Figure 4.3. Collapse pits have been observed to span tens to hundred meters across and have depths of 10-25 m (Ballard et al., 1979), which is well within the resolution (Table 1), and also fits well with the measured size of the pits (section 4.2.1) (Figure 5.1). The main problem with this solution is the fact that even if the pits in Figure 4.3 are somewhat angular, they mostly look semicircular (Figure 4.3). If the pits are associated exclusively to collapse structures, one would expect a greater degree of elongation amongst them.

The pseudocraters described in section 1.2 represent another possible origin of the structures seen in Figure 4.3, as argued by Planke et al., 2017 and Lebedova-Ivanova et al., 2023.

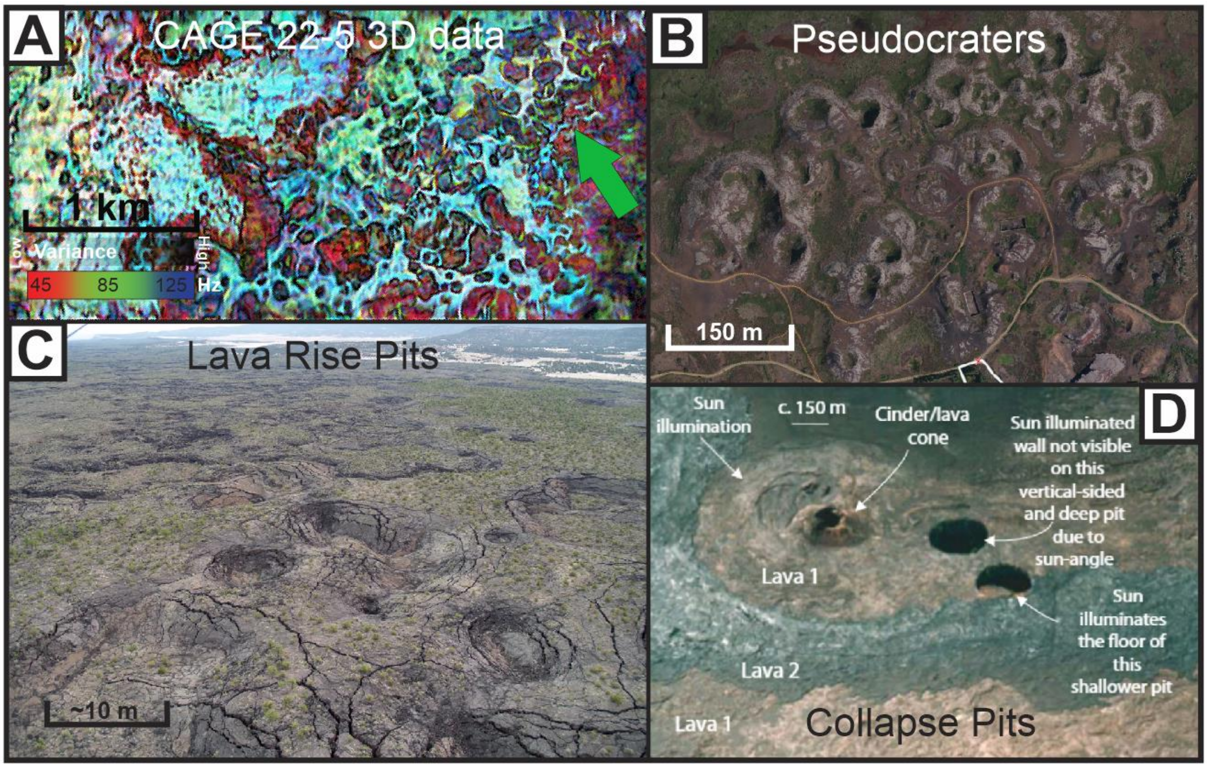

Figure 5.1. A comparison of various lava morphologies to the structures from the CAGE 22-5 data in A (also shown in Figure 4.3). B shows pseudocraters from Rauðhólar just outside of Reykjavik in Iceland. The photo is from https://map.is/base/@365496,402139,z12,0 (accessed march 2024). C displays lava rise pits on the McCarthy flow in El Malpais National Monument. Photo is taken by Larry Crumpler and can be found at https://www.nps.gov/articles/000/inflation-structures-lava-rise-plateaus-inflation-pits.htm (accessed march 2024) .D is showing Collapse pits from Kilauea on Hawaii. This picture is from Roberts et al., 2007.

The pseudocraters are resolvable in the data (Table 1), and their size (section 1.2) fit with the size of the observed structures (section 4.2.1) (Figure 5.1). If this is the case, it means that the lava was in contact with water during emplacement. This could happen in water-saturated sediments in a marine or lacustrine environment, or in in a wetland area with pools and ponds of surface water.

One detail that could determine whether pseudocraters are present, is the rim that they would have around their craters, but this is not possible to observe within the resolution here. Based on the previous arguments and the comparison in Figure 5.1, the combination of pseudocrater morphology and lava rise pits seems to fit the best with the pits presented in Figure 4.3, but it might be an interplay of several processes. The larger pits observed may be remnants of smaller lakes, quenching the lava at its shores and hindering the lava flow in the lake area. In any case, the structures are related to lava flows, and likely also to the presence of water. According to Lebedova-Ivanova et al., 2023 these lava flows can be seen in between the pits, and they show up as bright colors on the spectral decomposition in Figure 4.3. This fits well with the observed lobate structures with high amplitude (section 4.2.1 & Figure 4.3) and the formation of the pits.

Even though the well log of IODP well U1572 is not penetrating the basalt sequence by a lot (Figure 4.1), it indicates that the flows in the pitted domain are relatively massive (comparing to well logs in Nelson et al., 2009a, Millet et al., 2021, and Millet et al., 2024) and uninterrupted by sediment packages.

<u>Faulted Domain</u>

The toplap of the top basalt in the faulted domain into the sediments above, together with the fact that top basalt reflectors now tilt toward the ocean (section 4.2.2 & Figure 4.3), suggests that the facies have shifted towards SDR’s, as would be expected in this area. The apparent change in thickness of the acoustically visible part of the basalts appear to indicate, that the reflection coefficient is lower in the faulted domain than in the pitted domain. The vertical features above the big faults (section 4.2.2, Figure 4.3) might be caused by fluids or gas using the faults as a pathway to ascend towards the surface, but it is not very prominent, and there are no other indications of this in the area.

The well log for IODP well U1571 (section 4.2.1, Figure 4.1) seems to suggest thicker sedimentary packages between the basalt flows. This could indicate either less flows, more time in between the flows, or a higher deposition rate in this area. The flows between 180-210 m (Figure 4.1) looks to resemble compound flows more than massive simple flows, when comparing to well logs in Nelson et al., 2009a, Millet et al., 2021, and Millet et al., 2024. The rest of the flows look like massive simple flows, and a mix of different flow types in this well is backed up by the well report (Planke et al., 2023a)

To sum up, the pitted domain and the faulted domain have different emplacement environments because of their internal differences. The faulted domain is part of the SDR's and show a mix of simple flows and compound flows. The pitted domain that is overlying these contains massive simple flows and was likely deposited on wet and uneven terrain.

<u>Lava Flow Emplacement</u>

The origin of these flows has an origin somewhere towards the north, since they all flow southwards toward the escarpment. An example of a lava source could be the northwestern reflection described in section 4.9.2 and compared to a fissure in the rift zone on Reykjanes Peninsula in Iceland on Figure 5.2.

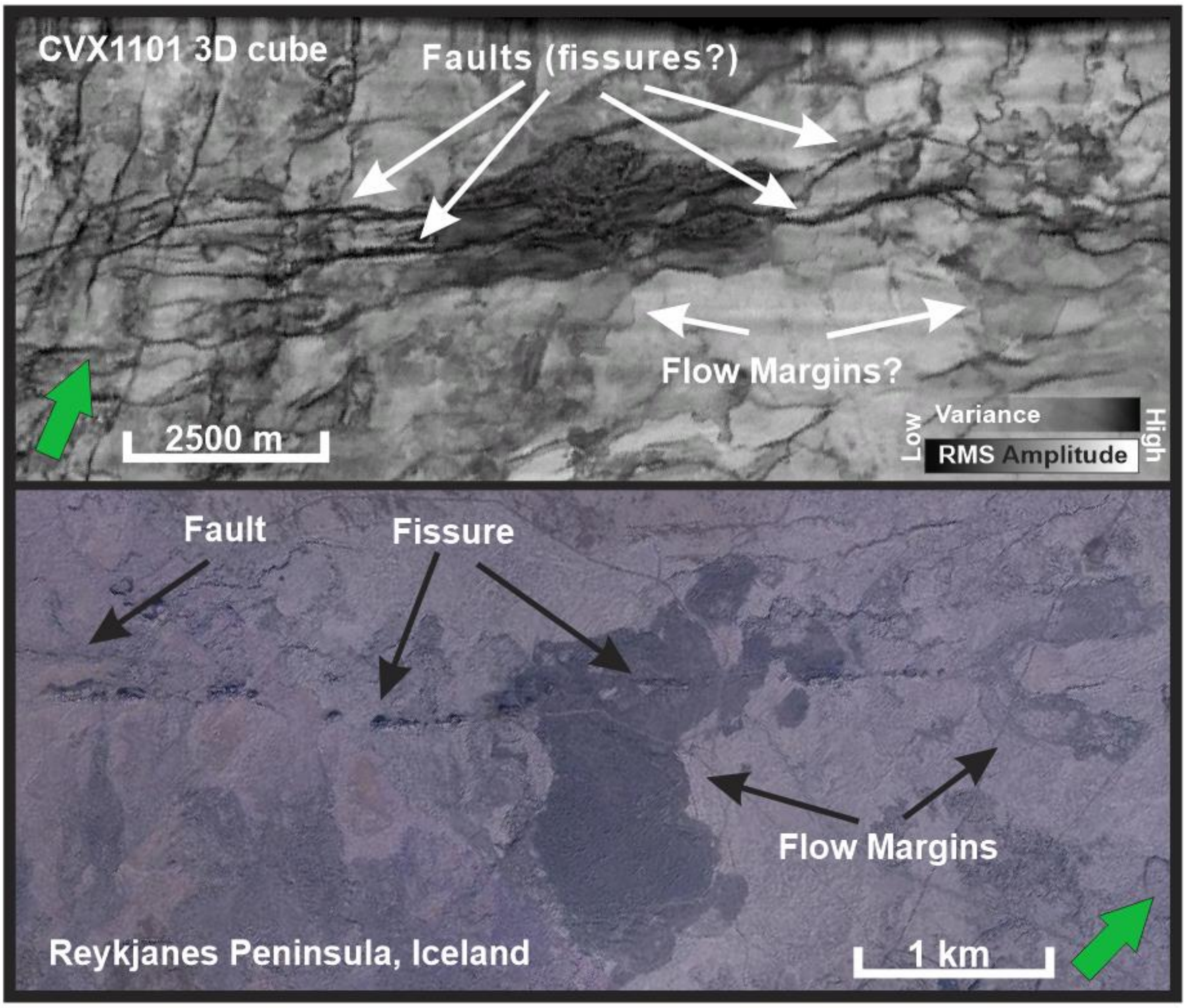

Figure 5.2. A comparison of the northwestern reflection from section 4.9.2 with a fissure from a rift zone on the Reykjanes Peninsula in Iceland. The aerial photo from Iceland can be found at https://map.is/base/@326904,377335,z9,2 (accessed march 2024).

Certain similarities such as the prominent continuous faults and the lava flow margins in the vicinity of them are noticeable. Big faults like these are abundant north of all the lava flows identified (Figure 4.5 and Figure 4.11), and it is possible that they could be fissures. The pitted surface is also located just south of several large faults like the ones in Figure 5.2, so also here the possibility of fissures is present. It is however hard to prove a direct connection between lava flows and faults, so this will remain just speculation until further data or knowledge is available.

The lava flows themselves (shown in Figure 4.7) can be compared to the flow morphologies presented in Figure 1.2 and described in section 1.2. It is tempting to say that the two northernmost flows in Figure 4.7A, the flow in Figure 4.7C, major flows from Figure 4.7G are simple tabular flows, and that the southernmost flow in 4.7A, and the flows in Figure 4.7F are compound braided flows.
This is due to the margins of the flows, their general outlook , their lateral spreading, the well log for the IODP well U1572, as well as the seismic in Figure 4.3 (using the method of Jerram et al., 2009, Nelson et al., 2009b, and Walker et al., 2022) when comparing to Figure 1.2. The factual basis for such an interpretation is however too thin to back it up. A way to determine this for sure is with continuous cores from a well, or with a Formation MicroScanner or Ultrasonic Borehole Imager as in the IODP U1571 & U1572 well report from Planke et al., 2023a.

5.3 Channels

The channels crossing the high (Figure 4.4 and Figure 4.6) are important, because they witness of a significant period of subaerial exposure, after the last lava flows were emplaced, as also argued by Planke et al., 2017. The size and distribution of this network cement the fact, that a widespread drainage system has had time to develop before the high was submerged in water. The comparison between these channels and river channels in the Columbia River Basalt Province in Figure 5.3 shows several similarities. The characteristic meandering shapes and tributary channels are present in both cases as well as a range of different channel sizes.
A few of the channels appear to reach all the way to the north side of Skoll High (Figure 4.4),

which means that when the channels were made, the high might have had a slightly different morphology than the one that can be seen today.

Another important detail is the termination of the channels shown in Figure 4.6. This line does clearly not correspond to the Vøring Escarpment which one would expect, and the fact that it does not, can be explained in several ways as I see it. It could mean that the water level was up to this line when the channels where made, or that the water level was up to this line for some time after the channels were made, eroding the furthest joints of the channels in a shallow marine environment. A transgression is known to have happened at some point since the basalts were emplaced, and it is not impossible that the water level was stable at this specific level for some time.

A channel was also found on the base basalt surface very close to the Vøring Escarpment (also described by Maharjan et al., 2024), reaching all the way to the edge. It is not as prominent as the channels on the top basalt, and it is difficult to say if it is submarine or subaerial. If it is subaerial, it corresponds to the channels observed on the top basalt, and it means that there must have been significant breaks in between lava flows at the beginning of Eocene when these flows where emplaced. If it is submarine, it might correspond to the structures around the sediment window (section 4.6.1) originating from lava and debris flows.

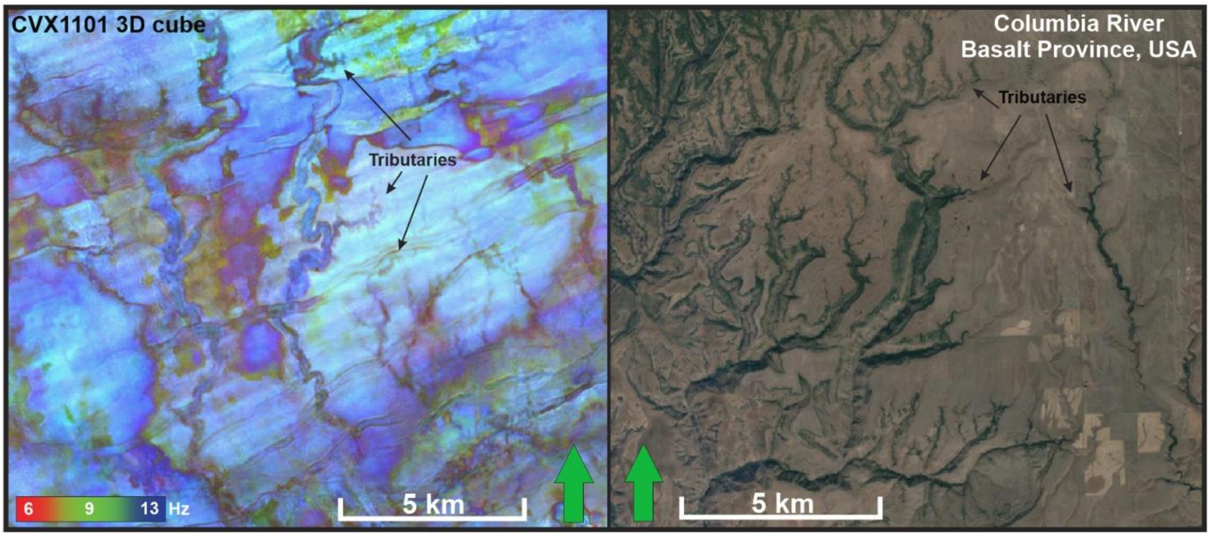

Figure 5.3. A comparison of the channels on the spectral decomposition of the top basalt from the CVX1101 3D cube with river channels from the Columbia River Basalt Province in Washington, USA, where river channels have eroded the flood basalts there. The aerial photo is from Google Earth(accessed march 2024).

5.4 Low Amplitude Areas

The low amplitude areas that can be seen in Figure 4.5, Figure 4.8, Figure 4.9, and Figure 4.10 need to be addressed, because they clearly appear as anomalies in their surroundings. An interpretation could be that invasive lavas are at play, burrowing into wet unconsolidated sediments due to their higher density, thus creating a sill-like body (Larsen & Pedersen 1990). This interpretation would fit very well with the sills that tend to underlie the low amplitude areas. This would on the other hand mean that the lava flows had sunk some 100-200 ms TWT into underlying sediments. Using a velocity of 4244 m/s (as in section 3.9) this is equivalent to a distance between 212-424 m which seems unlikely.

An additional interpretation is that the contact aureoles of the sills underneath have created hydrothermal fluids or gases that have migrated upwards and are residing around the top basalt, masking the reflections that would otherwise be visible. This fits well with both the sills placement underneath the low amplitude areas and the chimney structures (section 4.5, Figure 4.8, Figure 4.9, and section 5.5) above Ridge A, B, and C in the vicinity. The main problem with this theory is that if gas was present, there would be high amplitude reflectors at the very top of it.

A more obvious interpretation would be to say that they are formed identically to the sediment window (section 4.6.1) interpreted by Planke et al., 2017. This would mean that their high topography would make it so that either there were never any lavas covering these areas, or only very little that was later eroded. While this could be true for the area adjacent to Ridge A (Figure 4.8), the area adjacent to Ridge C does not consist of a natural high, that would make this interpretation possible. It is possible that it was a high when the lavas where emplaced, meaning that serious deformation would have occurred in connection to the formation of Ridge B and Ridge C after the top basalt was emplaced. Even though this is not impossible, it seems unlikely.

5.5 Post emplacement deformation

5.5.1 Faults

A clear sign of the deformation that has undergone the basalt sequence after emplacement is the faults that cover most of the Vøring Marginal High in the data (Figure 4.11). The faults are mostly affecting the basalt sequence, making them Paleocene - early Eocene in age. A few faults with sporadic distribution are reaching all the way into the Kai Formation, making them Miocene of age, possibly as reactivations of earlier faults. The fact that many faults have their top in the top basalt surface adds to the thesis that some of them could be fissures as mentioned in section 5.2. The Paleocene – early Eocene genesis of the faults fit well with faulting moving towards the volcanic domain in this period as described in section 2.2.6, meaning that they are related to the rifting and extension associated with the breakup of the northeast Atlantic.

5.5.2 Gas and fluid migration

Another indication of the deformation that has happened to the volcanic sequence is Ridge A, B, and C since they have clearly deformed the inner flows (Figure 4.8 and Figure 4.9). This means that they have formed either simultaneously with or after the emplacement of the volcanic sequence. Signs of fluid anomalies in the notably vertically deformed sedimentary sequence indicate that the anticlinal structures have been used by fluid migration, and the small pockets of higher amplitude within the chimneys (section 4.5, Figure 4,8 and Figure 4.9) are interpreted as either gas accumulations or methane derived authigenic carbonates. Faults crosscutting large part parts of the sedimentary sequence are present in this area, and together with the widespread polygonal faulting around the Base Kai surface between the ridges (Figure 4.8 and Figure 4.9), this might have contributed to the migration of gas and fluids. The ridges are aligned with both the fault system of the Northern Gjallar Ridge and the faults north of the Vøring Escarpment (section 5.5.1), and they could be related to either one of these systems. The migrating gas or hydrothermal fluid could be generated by sills in the sedimentary sequence (section 1.3.4 for background) underneath the basalts, as is the case for Ridge C in Figure 4.9. Sills are known to be widespread in this area (Planke et al., 2005, Angkasa et al., 2017, and section 1.4) and this would also fit well with the minor chimneys in Figure 4.8. This figure suggests that the sills generated gas or hydrothermal fluids, that migrated upwards, creating the minor chimney structures above.

5.5.3 Lava delta and bench collapse

The collapse of lava deltas is widely documented (Smellie et al., 2013, Poland & Orr, 2014, Neal & Anderson 2020, and Soule et al., 2021), and apart from signs of slumping and failure of the lava delta on the seismic, several structures resembling collapse-features can be seen on the surface of the top basalt as shown in Figure 5.4. Although the structures from the CVX1101 3D data (Figure 5.4D and Figure 5.4E) are approximately twice the size of the examples from Hawaii (Figure 5.4A, Figure 5.4B, and Figure 5.4C), they look alike in shape as well as inclination and size relative to the escarpment. Slumping and collapse has also been observed in this area by Planke et al., 2017 and Abdelamak et al., 2016b. These features could be created due to a build-up of material overstepping the angle of repose, or due to a decrease in sealevel, making the deposits “heavier”, but it seems impossible to determine which of these have impacted the Vøring Escarpment the most.

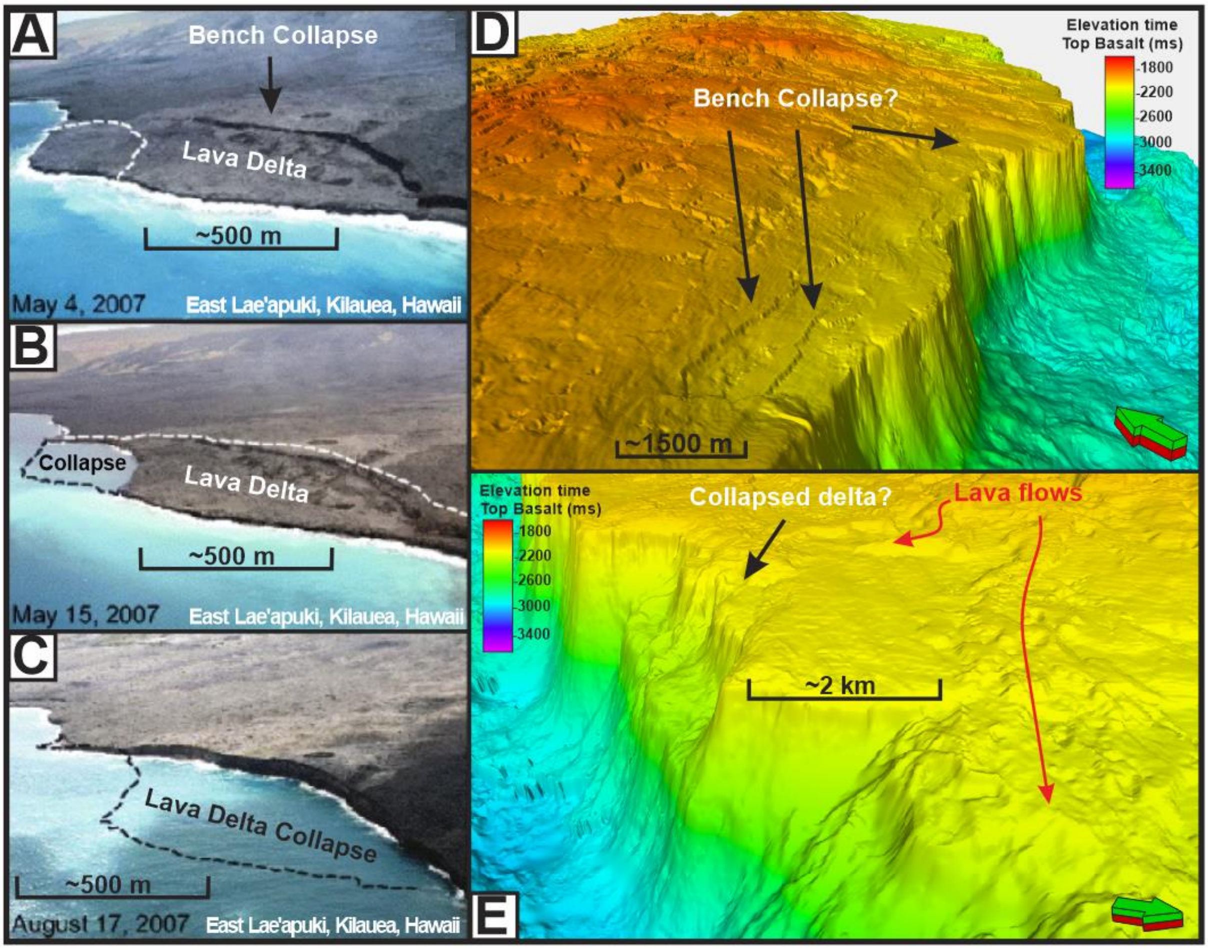

Figure 5.4. Comparison between data examples and field analogues from Hawaii of bench collapse and delta collapse. A, B and C are modified from Poland & Orr, 2014, and D and E is the top basalt surface in TWT from the CVX1101 3D cube, shown with a vertical exaggeration of 5.

5.5.3 Mysterious reflection

The last structure that has formed post emplacement of the volcanic sequence is the southeastern reflection (Figure 4.13 and section 4.9.1) whose origin is somewhat mystical. It is a post emplacement structure because it is located above the basalts. Because it is a high amplitude section in an otherwise semi-continuous reflector, it is natural to think that it might be a sill or an intrusive lava flow, but since it is later in time than the basalts, this is unlikely. Another theory is that it could be volcanic slide deposits originating from the slope of Ridge C. However, this would mean that the slope of Ridge C was not covered by sediments (as the area underneath the reflection was) by the time the slide happened, and it furthermore seems strange, that the slide deposits would be continuous to the other side of Ridge C and continue further north were the ridge is not present. If it was a mass wasting deposit, it would also fit very poorly with the very elongated shape and coherent character of the reflection. It could also be accumulated gas underneath a reflector, creating the short interval with high amplitude. This fits well with the migration structures associated with Ridge C in the vicinity, but it does not really fit with the position of the reflector. It's hard to imagine that a gas accumulation could have a tilt like the reflector has, without the gas travelling upwards towards the next obstacle. It is also possible that it is a reflector that was formed before the formation of Ridge C. This would mean the formation of Ridge C could have deformed the reflection, and possibly cut it short. This seems like the most likely theory to explain the relation between the reflection and Ridge C, but the truth remains a mystery.

5.6 Geological model

A simple and general geological model of the development the Skoll High area is proposed based on previous research, as well as the main results of this thesis (Figure 5.5)
The first stage of the model shows the time before extensive volcanism occurred, and it roughly covers late Cretaceous to late Paleocene. In this prevolcanic time, the main factor affecting the area is rifting, and regional uplift (section 2.6.6, Ren et al., 2003). This rifting results in the Vøring Escarpment (Mjelde 2003), and the uplift shallows the sediments. In addition, intrusions and sills are emplaced (Planke et al., 2005).

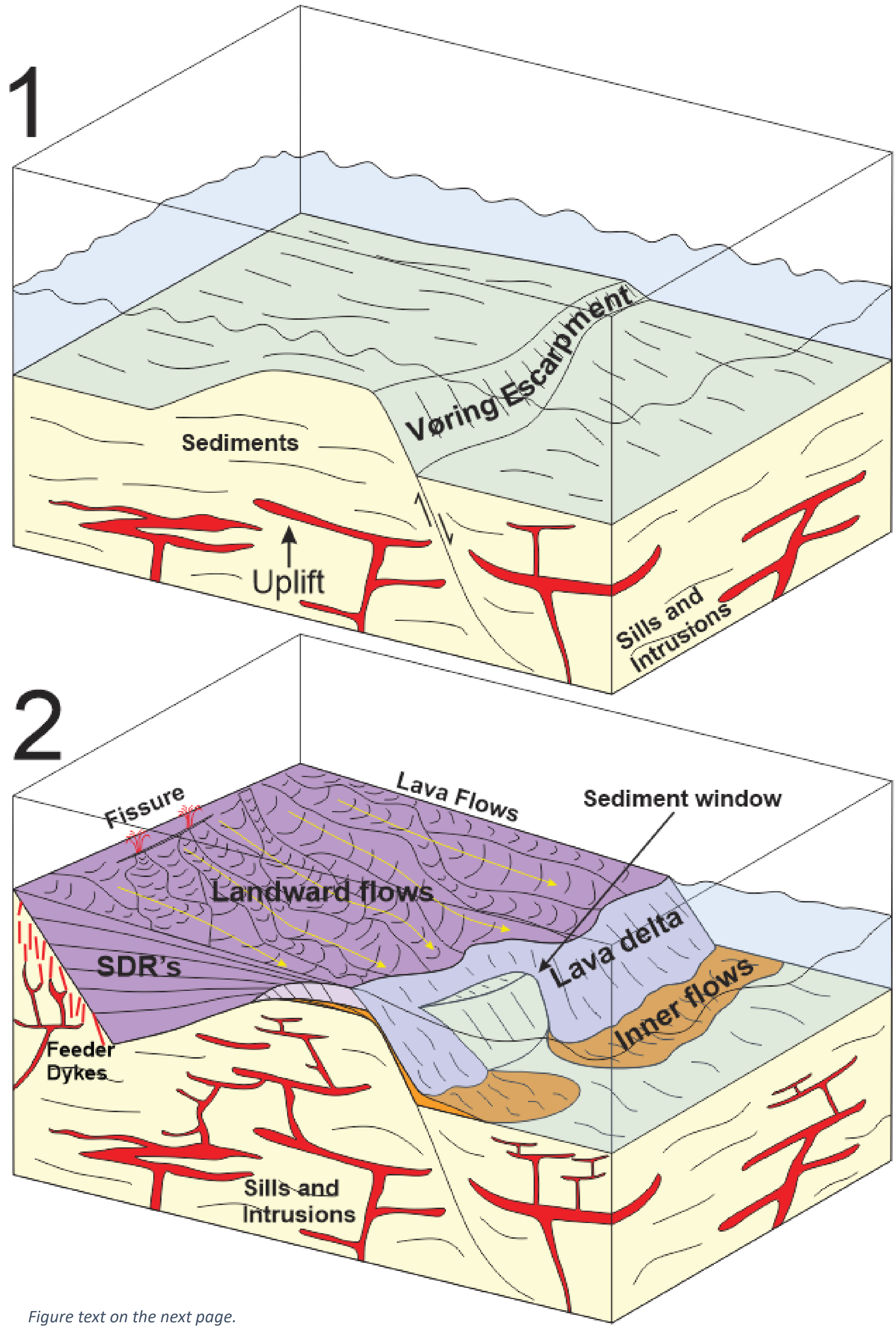

Figure text on the next page.

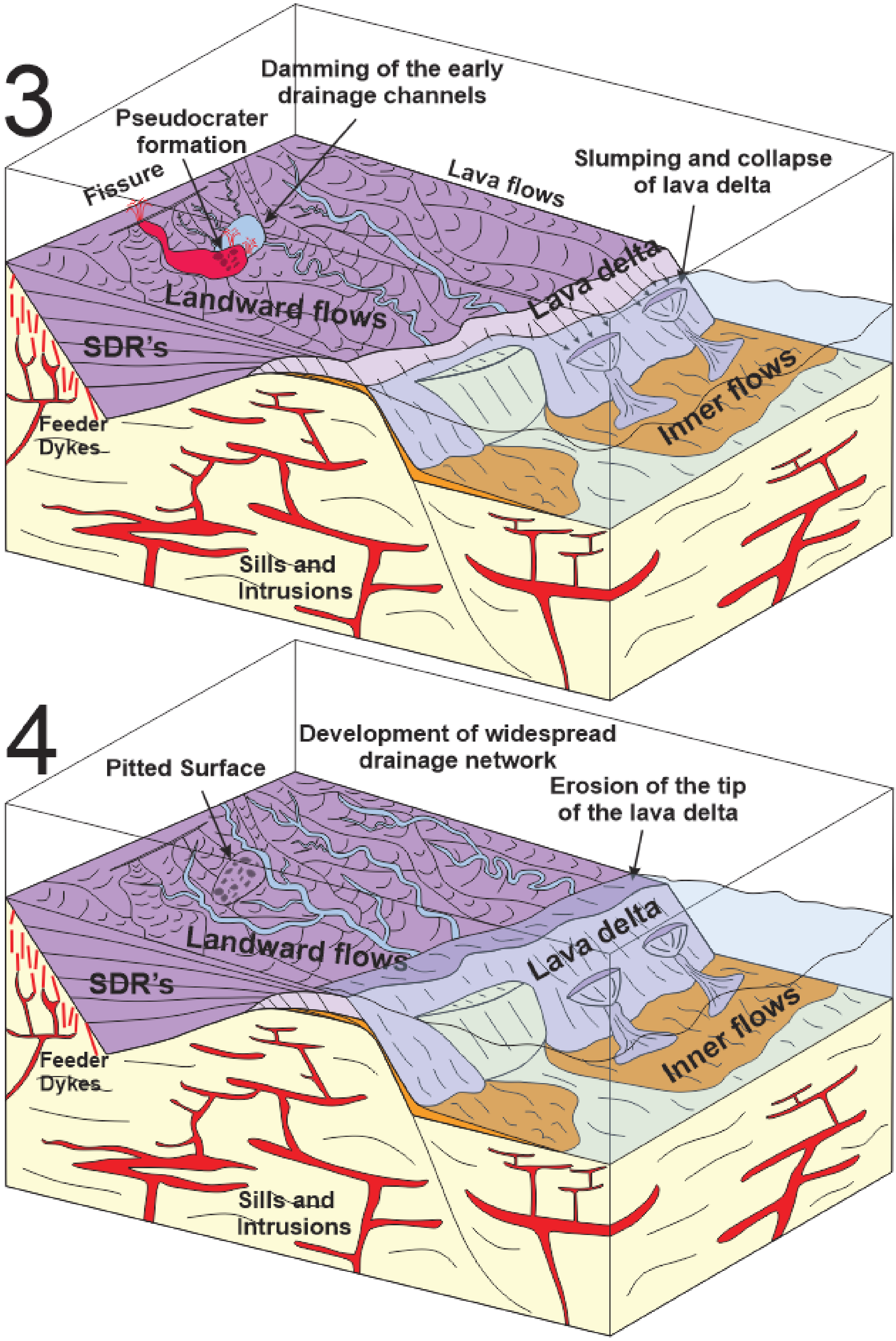

Figure 5.5. Conceptual geological model of the development of Skoll High. Design and colors inspired from Abdelamak et al., 2016a, Abdelamak et al., 2016b, and Planke et al., 2017.

The second stage of the model shows the time well into early Eocene, when Skoll High is comprising a subaerial environment dominated by flood basalt flows. Inner SDR's are created by feeder dykes and landward tilting faults, and transition into the landwards flows towards the escarpment. When these flows spill into the sea the lava is quenched, creating lava delta foresets of hyaloclastites. Beneath the lava delta, the inner flows are created by sheet flows, pillow lava and shallow intrusions (section 1.3, Planke et al., 2000, Abdelamak et al., 2016b, Planke et al., 2017). The sills and intrusions are more developed and widespread.

In the third stage, the water level is slightly lower creating slumps and collapses in the lava delta and on the slope of the escarpment (Abdelamak et al., 2016b, Planke et al., 2017, Maharjan et al., 2024). The topography on the high is not only dominated by lava flows any longer, as drainage channels are starting to develop in between periods of the waning volcanic activity. The mixing of surface water and lava flows create a pitted surface of pseudocraters, possibly due to drainage ponding (Ebinghaus et al.,2014, Boreham et al., 2018, Ebinghaus et al., 2020, Millet et al., 2022)

In the fourth stage the water level has risen to above the escarpment, flooding the outermost part of the landward flows and eroding them in a shallow marine environment (section 5.3). The drainage channels are now the dominating process affecting topography and deposition on the high, which means that a widespread network of channels develop before the high is completely submersed in water (section 5.3).

5.7 Carbon sequestration potential

The carbon sequestration potential of Skoll High is complicated to estimate, and it depends on a lot of parameters. Here, I will mainly focus on mineral storage in the basalt sequence and try to simplify the scenario as much as possible. The most obvious thing to consider when assessing the storage potential would be the storage space, which can be deduced from the porosity. Planke et al., 2023a found a porosity of 20-60% for MAD samples with unfilled vesicles in hole U1571A, and a porosity of 3-70% in hole 1572A. Furthermore, the open primary porosity in both wells was found to commonly exceed 40%. Rosenqvist et al., 2023 found indications of good primary porosities in the Faroe Islands as an analogue to potential NAIP storage sites, and Planke, 1994 found that most flow crusts in ODP 642E displayed open porosity, suggesting that intervals of high porosity can be found on the marginal high. If one assumes a mean porosity of 15% and a supercritical CO_2 density of 300 kg/m^3 (Kelemen et al., 2019), and puts it together with the basalt volume calculation of 1500 km^3 (section 4.8), this gives a storage space of 225 km^3, equivalent to 67,5 Gt of CO_2. For reference, the CO_2 emission in 2018 was 40 Gt, and we must remove 10 Gt CO_2/year from the atmosphere by 2050, if we want to stay below the 2° goal (IPCC, 2018, Kelemen et al., 2019, and section 1.1). The calculation that gives a storage of 67,5 Gt of CO_2 on Skoll High is, however, the simplest calculation that can be made, and therefore it can be used only as a preliminary estimation about the actual storage potential. A mean porosity of 15% might be optimistic and is probably more representative for the intervals that might be used for storage, however large that fraction might be. All the porosity can't be used either, as the system would clog before reaching zero porosity. In fact, there are many factors complicating the estimation of CO_2 storage potential, and these relate to: primary porosity and permeability, intraflow porosity and permeability variations, porosity and permeability variations between flows, types of lava flows (AA, Pahoehoe, simple, compound), thickness of flows, lateral extent of flows, reservoir architecture, core crust ratio, thickness and distribution of interbasalt volcaniclastic sediment packages, mineralogy of the basalt (chemical environment), precipitation of other minerals than carbonates, alteration of the basalts, fracture and fault distribution, and injection site physical properties such as pressure, temperature, water saturation, and PH values (Danqing et al., 2019, Raza et al., 2022, Albertz et al., 2023, Delerce et al., 2023, Sun et al., 2023, and Millet et al., 2024). All these factors would each help to sophisticate my simple storage calculation and make it more realistic. It is not easy to collect information about all these complicating factors, and not all of them are necessarily needed to make a realistic assessment of the storage potential. The next step in my view would be to obtain knowledge about the 3D structure of the basalt sequence, along with representative values of porosity and permeability for separate intervals, which would mean that reservoirs that has the physical storage capacities could be identified and further investigated for the suitability for CO_2 injection. This could be achieved with more wells and high-resolution 3D seismic data.

Several studies (Kirkpatrick, 1973, Mavko & Nur, 1997, Rintoul & Torquato, 1997) have shown that a minimum porosity threshold of about 30% is required for percolation to take place in a material with randomly dispersed spherical pores (in this case vesicular basalt), and McGrail et al., 2006 stated that a flow thickness > 10 m and a minimum porosity of 15% would be needed for CO_2 injection into basalts (section 1.1). Considering the previously mentioned porosities and flow thicknesses from the IODP wells (Planke et al., 2023a) and the Faroe Islands Basalt Group (Rosenqvist et al., 2023) these conditions can be found on Skoll High, although they are rare, and their distribution and continuity is uncertain. Rosenqvist et al., 2024, on the other hand, makes the argument that even though the flow crusts with > 10 m thickness and 15% porosity are rare, the connectivity of single flow crusts might magnify the reservoir, and make a system where McGrail's 10 m thickness threshold is no longer applicable.

Another thing is that if the CO_2 is injected in a gaseous phase instead of in a supercritical state, seals will need to be present above the injection interval to keep the gas from escaping, and giving it time to mineralize. Rosenqvist et al., 2023 and Rosenqvist et al., 2024 argued that packages of simple flows, each with thicknesses of about 25 m, are present in the Faroe Island Basalts, and that they would work as seals, and Planke et al., 2021c argued that the sedimentary sequence above the basalt sequence would also work as a seal in case of eventual leakage, so a lack of seals would not be a problem.

Conclusively, a lot of things can be suggested and hinted at from the current data available, but the facts are that more data about potential reservoir sites, and knowledge about how CO_2 behaves when injected into basalts (on a microscale and in the long term) is needed for industrial scale injection to begin (Raza et al., 2022 and Sun et al., 2023).

6 Conclusion

3D seismic data and well data have been used to determine the origin and emplacement mechanisms of the basaltic sequence on Skoll High. This has been done with focus on the top basalt and intrabasalt structures, as well as the stratigraphic setting and postemplacement structures.

- Based on the approach of volcanostratigraphy developed by Planke et al., 2000 and Berndt et al., 2001, the SDR's, landward flows, lava delta, and inner flow units that are so characteristic for volcanic rifted margins, have been interpreted in the study area.
- A pitted surface is shown, and it is most likely consisting of pseudocraters that are interpreted to originate from contact between surface water and lava flows.
- A possible fissure has been showcased and compared to a field example in Iceland.
- A widespread network of drainage channels has been visualized and proves a significant period with volcanic hiatus and subaerial exposure before Skoll high was covered by the sea.
- Clear evidence of gas or fluid migration is present in the area, and several chimney structures possibly connected to underlying sills have been imaged. Their origin is placed simultaneously with or after the emplacement of the volcanic sequence.
- Evidence of bench collapse and lava delta collapse on the escarpment have been presented and compared to field examples from Hawaii.

Based on these results and previous studies, a geological model for Skoll high is proposed describing 4 stages: 1 Uplift, intrusions, sill emplacement, and the creation of the Vøring escarpment due to rifting, 2 emplacement of SDR's, landwards flows, inner flows, and the creation of a lava delta, 3 regression, collapse of lava delta, pseudocrater formation due to mixing of surface water and lava flows, 4 trangression, erosion of the high, and formation of a widespread drainage network.
The assessment of the storage potential for CO_2 sequestration on Skoll High has resulted in a preliminary estimate of 67,5 Gt of CO_2 worth of storage space. This is however a very simple calculation, and it needs further evaluation with regards to more data and knowledge about how CO_2 behaves when injected into basalt sequences to approach a more realistic estimate.

References

Abdelmalak, M. M., Faleide, J. I., Planke, S., Gernigon, L., Zastrozhnov, D., Shephard, G. E., & Myklebust, R. (2017). The T-Reflection and the Deep Crustal Structure of the Vøring Margin, Offshore mid-Norway. *Tectonics*, *36*(11), 2497-2523. https://doi.org/https://doi.org/10.1002/2017TC004617

Abdelmalak, M. M., Meyer, R., Planke, S., Faleide, J. I., Gernigon, L., Frieling, J., Sluijs, A., Reichart, G. J., Zastrozhnov, D., Theissen-Krah, S., Said, A., & Myklebust, R. (2016). Pre-breakup magmatism on the Vøring Margin: Insight from new sub-basalt imaging and results from Ocean Drilling Program Hole 642E. *Tectonophysics*, *675*, 258-274. https://doi.org/https://doi.org/10.1016/j.tecto.2016.02.037

Abdelmalak, M. M., Planke, S., Faleide, J. I., Jerram, D. A., Zastrozhnov, D., Eide, S., & Myklebust, R. (2016). The development of volcanic sequences at rifted margins: New insights from the structure and morphology of the Vøring Escarpment, mid-Norwegian Margin. *Journal of Geophysical Research: Solid Earth*, *121*(7), 5212-5236. https://doi.org/https://doi.org/10.1002/2015JB012788

Albertz, M., Stewart, S. A., & Goteti, R. (2023). Perspectives on geologic carbon storage [Review]. *Frontiers in Energy Research*, *10*. https://doi.org/10.3389/fenrg.2022.1071735

Ali, J. R., Fitton, J. G., & Herzberg, C. (2010). Emeishan large igneous province (SW China) and the mantle-plume up-doming hypothesis. *Journal of the Geological Society*, *167*(5), 953-959. https://doi.org/doi:10.1144/0016-76492009-129

Angkasa, S. S., Jerram, D. A., Millett, J. M., Svensen, H. H., Planke, S., Taylor, R. A., Schofield, N., & Howell, J. (2017). Mafic intrusions, hydrothermal venting, and the basalt-sediment transition: Linking onshore and offshore examples from the North Atlantic igneous province. *Interpretation*, *5*(3), SK83-SK101. https://doi.org/10.1190/int-2016-0162.1

Aubert, K., Elseth, T., Ellevset, H., Sandvik, J., Bakøy, P., Skottlien, E. (1999). Final Well Report 6704/12-1 from Saga Petroleum. 47-55

Badley, M. E. (1985). Practical Seismic Interpretation. International Human Resources Development Corporation. https://books.google.no/books?id=42rxAAAAMAAJ. 265

Ball, M., Pinkerton, H., & Harris, A. J. L. (2008). Surface cooling, advection and the development of different surface textures on active lavas on Kilauea, Hawai'i. *Journal of Volcanology and Geothermal Research*, *173*(1), 148-156. https://doi.org/https://doi.org/10.1016/j.jvolgeores.2008.01.004

Ballard, R. D., Holcomb, R. T., & van Andel, T. H. (1979). The Galapagos Rift at 86° W: 3. Sheet flows, collapse pits, and lava lakes of the Rift Valley. *Journal of Geophysical Research: Solid Earth*, *84*(B10), 5407-5422. https://doi.org/https://doi.org/10.1029/JB084iB10p05407

Berndt, C., Planke, S., Alvestad, E., Tsikalas, F., & Rasmussen, T. (2001). Seismic volcanostratigraphy of the Norwegian Margin: Constraints on tectonomagmatic break-up processes. *Journal of the Geological Society*, *158*, 413-426. https://doi.org/10.1144/jgs.158.3.413

Berndt, C., Planke, S., Teagle, D., Huismans, R., Torsvik, T., Frieling, J., Jones, M. T., Jerram, D. A., Tegner, C., Faleide, J. I., Coxall, H., & Hong, W. L. (2019). Northeast Atlantic breakup volcanism and consequences for Paleogene climate change – MagellanPlus Workshop report. *Sci. Dril.*, *26*, 69-85. https://doi.org/10.5194/sd-26-69-2019

Black, B. A., Karlstrom, L., & Mather, T. A. (2021). The life cycle of large igneous provinces. *Nature Reviews Earth & Environment*, *2*(12), 840-857. https://doi.org/10.1038/s43017-021-00221-4

Blystad, P, Brekke, H., Færseth, R. B., Larsen, B. T., Skogseid, J., & Tørudbakken, B., (1995). Structural elements of the Norwegian Continental Shelf. Part II: The Norwegian Sea region, *Bull., 9*, Norwegian Petroleum Directorate, Stavanger.

Boreham, F., Cashman, K., Rust, A., & Höskuldsson, Á. (2018). Linking lava flow morphology, water availability and rootless cone formation on the Younger Laxá Lava, NE Iceland. *Journal of Volcanology and Geothermal Research*, *364*, 1-19. https://doi.org/https://doi.org/10.1016/j.jvolgeores.2018.08.019

Bosman, A., Casalbore, D., Romagnoli, C., & Chiocci, F. L. (2014). Formation of an 'a'ā lava delta: insights from time-lapse multibeam bathymetry and direct observations during the Stromboli 2007 eruption. *Bulletin of Volcanology*, *76*(7), 838. https://doi.org/10.1007/s00445-014-0838-2

Brown, A. R. (1999). Interpretation of Three-Dimensional Seismic Data. *American Association of Petroleum Geologists and the Society of Exploration Geophysics*. 233-307. https://doi.org/10.1306/m4271346

Bryan, S. E., & Ernst, R. E. (2008). Revised definition of Large Igneous Provinces (LIPs). *Earth-Science Reviews*, *86*(1), 175-202. https://doi.org/https://doi.org/10.1016/j.earscirev.2007.08.008

Bryan, S. E., Peate, I. U., Peate, D. W., Self, S., Jerram, D. A., Mawby, M. R., Marsh, J. S., & Miller, J. A. (2010). The largest volcanic eruptions on Earth. *Earth-Science Reviews*, *102*(3), 207-229. https://doi.org/https://doi.org/10.1016/j.earscirev.2010.07.001

Buck, W. R. (2017). The role of magmatic loads and rift jumps in generating seaward dipping reflectors on volcanic rifted margins. *Earth and Planetary Science Letters*, *466*, 62-69. https://doi.org/https://doi.org/10.1016/j.epsl.2017.02.041

Campbell, I. H. (2005). Large Igneous Provinces and the Mantle Plume Hypothesis. *Elements*, *1*(5), 265-269. https://doi.org/10.2113/gselements.1.5.265

Coffin, M. F., & Eldholm, O. (1994). Large igneous provinces: Crustal structure, dimensions, and external consequences. *Reviews of Geophysics*, *32*(1), 1-36. https://doi.org/https://doi.org/10.1029/93RG02508

Collier, J. S., McDermott, C., Warner, G., Gyori, N., Schnabel, M., McDermott, K., & Horn, B. W. (2017). New constraints on the age and style of continental breakup in the South Atlantic from magnetic anomaly data. *Earth and Planetary Science Letters*, *477*, 27-40. https://doi.org/https://doi.org/10.1016/j.epsl.2017.08.007

Danqing, L., Ramesh, A., Yilian, L., & Sen, Y. (2019). Reactive transport modeling of mineral carbonation in unaltered and altered basalts during CO2 sequestration. *International Journal* *of Greenhouse Gas Control*, *85*, 109-120. https://doi.org/https://doi.org/10.1016/j.ijggc.2019.04.006

Delerce, S., Heřmanská, M., Bénézeth, P., Schott, J., & Oelkers, E. H. (2023). Experimental determination of the reactivity of basalts as a function of their degree of alteration. *Geochimica et Cosmochimica Acta*, *360*, 106-121. https://doi.org/https://doi.org/10.1016/j.gca.2023.09.007

Dewangan, P., Ramprasad, T., & Ramana, M. (2007). Finite difference modelling of scattered hydrates and its implications in gas-hydrate exploration. *Current Science*, *93*.

Ebinghaus, A., Hartley, A. J., Jolley, D. W., Hole, M., & Millett, J. (2014). Lava–Sediment Interaction and Drainage-System Development In A Large Igneous Province: Columbia River Flood Basalt Province, Washington State, U.S.A. *Journal of Sedimentary Research*, *84*(11), 1041-1063. https://doi.org/10.2110/jsr.2014.85

Ebinghaus, A., Taylor, R., Barker, A., Hartley, A. J., Jolley, D. W., & Hole, M. J. (2020). Development of inter-lava drainage systems in LIPs: The Columbia River Flood Basalt Province (U.S.A.) as a case study. *Journal of Sedimentary Research*, *90*(10), 1346-1369. https://doi.org/10.2110/jsr.2020.64

Eidesgaard, Ó. R., Boldreel, L. O., Schovsbo, N. H., & Ólavsdóttir, J. (2023). Hydrocarbon-bearing volcanic lava deltas as potential reservoirs: A case study from the North Atlantic Igneous Province, Faroe-Shetland Basin. *AAPG Bulletin*, *107*(10), 1753-1779. https://doi.org/10.1306/06272321031

Eldholm, O., Thiede, J., & Taylor, E. (1989). Evolution of the Vøring Volcanic Margin. *Proc., scientific results, ODP, Leg 104, Norwegian Sea*, *104*, 1033-1065. https://doi.org/10.2973/odp.proc.sr.104.191.1989

Ernst, R. E. (2014a). Introduction, definition, and general characteristics. In *Large Igneous* Provinces (pp. 1-39). chapter, Cambridge: Cambridge University Press.

Ernst, R. E. (2014b). Assessing the origin of LIPs. In *Large Igneous* Provinces (pp. 459-498). chapter, Cambridge: Cambridge University Press.

Ernst, R. E. (2014c). Plumbing system of LIPs. In *Large Igneous* Provinces (pp. 111-153). chapter, Cambridge: Cambridge University Press.

Ernst, R. E., Liikane, D. A., Jowitt, S. M., Buchan, K. L., & Blanchard, J. A. (2019). A new plumbing system framework for mantle plume-related continental Large Igneous Provinces and their mafic-ultramafic intrusions. *Journal of Volcanology and Geothermal Research*, *384*, 75-84. https://doi.org/https://doi.org/10.1016/j.jvolgeores.2019.07.007

Ernst, R. E., & Youbi, N. (2017). How Large Igneous Provinces affect global climate, sometimes cause mass extinctions, and represent natural markers in the geological record. *Palaeogeography, Palaeoclimatology, Palaeoecology*, *478*, 30-52. https://doi.org/https://doi.org/10.1016/j.palaeo.2017.03.014

Bond, D. P. G. & Sun, Y. (2021) Global Warming and Mass Extinctions Associated with Large Igneous Province Volcanism. In Ernst, R. E., Dickson, A. J., Bekker, A. (2021). Large Igneous Provinces –

A Driver of Global Environmental and Biotic Changes. *American Geophysics Union, Wiley, Geophysical Monograpph 255, First Edition*.

Fagents, S., & Thordarson, T. (2007). Rootless volcanic cones in Iceland and on Mars. *The Geology of Mars: Evidence from Earth-Based Analog*.

Faleide, J. I., Tsikalas, F., Breivik, A., Mjelde, R., Ritzmann, O., Engen, O., Wilson, J., & Eldholm, O. (2008). Structure and evolution of the continental margin off Norway and the Barents Sea. *Episodes*, *31*, 82-91. https://doi.org/10.18814/epiiugs/2008/v31i1/012

Foulger, G. R., Doré, T., Emeleus, C. H., Franke, D., Geoffroy, L., Gernigon, L., Hey, R., Holdsworth, R. E., Hole, M., Höskuldsson, Á., Julian, B., Kusznir, N., Martinez, F., McCaffrey, K. J. W., Natland, J. H., Peace, A. L., Petersen, K., Schiffer, C., Stephenson, R., & Stoker, M. (2020). The Iceland Microcontinent and a continental Greenland-Iceland-Faroe Ridge. *Earth-Science Reviews*, *206*, 102926. https://doi.org/https://doi.org/10.1016/j.earscirev.2019.102926

Gac, S., Abdelmalak, M. M., Faleide, J. I., Schmid, Daniel W., & Zastrozhnov, D. (2022). Basin modelling of a complex rift system: The Northern Vøring Volcanic Margin case example. *Basin Research*, *34*(2), 702-726. https://doi.org/https://doi.org/10.1111/bre.12637

Ganino, C., & Arndt, N. T. (2009). Climate changes caused by degassing of sediments during the emplacement of large igneous provinces. *Geology*, *37*(4), 323-326. https://doi.org/10.1130/g25325a.1

Gernigon, L., Blischke, A., Nasuti, A., & Sand, M. (2015). Conjugate volcanic rifted margins, seafloor spreading, and microcontinent: Insights from new high-resolution aeromagnetic surveys in the Norway Basin. *Tectonics*, *34*(5), 907-933. https://doi.org/https://doi.org/10.1002/2014TC003717

Gernigon, L., Ringenbach, J.-C., Planke, S., Le Gall, B., & Jonquet-KolstO, H. (2003). Extension, crustal structure and magmatism at the outer V??ring Basin, Norwegian Margin. *Journal of The Geological Society - J GEOL SOC*, *160*, 197-208. https://doi.org/10.1144/0016-764902-055

Gernigon, L., Zastrozhnov, D., Planke, S., Manton, B., Abdelmalak, M. M., Olesen, O., Maharjan, D., Faleide, J. I., & Myklebust, R. (2021). A digital compilation of structural and magmatic elements of the Mid-Norwegian continental margin (version 1.0). *Norwegian Journal of Geology*. https://doi.org/10.17850/njg101-3-2

Gibson, I., & Love, D. (1989). A Listric Fault Model for the Formation of the Dipping Reflectors Penetrated during the Drilling of Hole 642E, ODP Leg 104. https://doi.org/10.2973/odp.proc.sr.104.195.1989

Gislason, S., & Oelkers, E. (2014). Carbon Storage in Basalt. *Science (New York, N.Y.)*, *344*, 373-374. https://doi.org/10.1126/science.1250828

Gómez-Romeu, J., Kusznir, N., Ducoux, M., Jammes, S., Ball, P., Calassou, S., & Masini, E. (2022). Formation of SDRs-Ocean transition at magma-rich rifted margins: Significance of a mantle seismic reflector at the western Demerara margin. *Tectonophysics*, *845*, 229624. https://doi.org/https://doi.org/10.1016/j.tecto.2022.229624

Greeley, R., Clara, U. o. S., Center, A. R., & Observatory, H. V. (1974). *Guidebook to the Hawaiian Planetology Conference*. NASA/Ames Research Center. 54 https://books.google.no/books?id=4nASAQAAIAAJ

Gregg, T. K. P. (2017). Patterns and processes: Subaerial lava flow morphologies: A review. *Journal of Volcanology and Geothermal Research*, *342*, 3-12. https://doi.org/https://doi.org/10.1016/j.jvolgeores.2017.04.022

Gregg, T. K. P., Fink, J. H., & Griffiths, R. W. (1998). Formation of multiple fold generations on lava flow surfaces: Influence of strain rate, cooling rate, and lava composition. *Journal of Volcanology and Geothermal Research*, *80*(3), 281-292. https://doi.org/https://doi.org/10.1016/S0377-0273(97)00048-6

Hallworth, M. A., Huppert, H. E., & Sparks, R. S. J., (1987). A laboratory simulation of basaltic lava flows. *Modern Geology*. 11, 93-107.

Hamilton, C., Fagents, S., & Thordarson, T. (2010). Explosive lava-water interactions II: Self-organization processes among volcanic rootless eruption sites in the 1783-1784 Laki lava flow, Iceland. *Bulletin of Volcanology*, *72*, 469-485. https://doi.org/10.1007/s00445-009-0331-5

Harkin, C., Kusznir, N., Roberts, A., Manatschal, G., & Horn, B. (2020). Origin, composition and relative timing of seaward dipping reflectors on the Pelotas rifted margin. *Marine and Petroleum Geology*, *114*, 104235. https://doi.org/https://doi.org/10.1016/j.marpetgeo.2020.104235

Hjelstuen, B. O., Sejrup, H. P., Haflidason, H., Nygård, A., Berstad, I. M., & Knorr, G. (2004). Late Quaternary seismic stratigraphy and geological development of the south Vøring margin, Norwegian Sea. *Quaternary Science Reviews*, *23*(16), 1847-1865. https://doi.org/https://doi.org/10.1016/j.quascirev.2004.03.005

Hon, K., Kauahikaua, J., Denlinger, R., & Mackay, K. (1994). Emplacement and inflation of pahoehoe sheet flows: Observations and measurements of active lava flows on Kilauea Volcano, Hawaii. *Geological Society of America Bulletin - GEOL SOC AMER BULL*, *106*, 351-370. https://doi.org/10.1130/0016-7606(1994)106<0351:EAIOPS>2.3.CO;2

IPCC Special Report (2018). *Global warming of 1.5°C*. Available online at https://www.ipcc.ch/sr15/

Jamtveit, B., Svensen, H., Podladchikov, Y. Y., & Planke, S. (2004). Hydrothermal vent complexes associated with sill intrusions in sedimentary basins. *Geological Society, London, Special Publications*, *234*(1), 233-241. https://doi.org/doi:10.1144/GSL.SP.2004.234.01.15

Jerram, D., Single, R., Hobbs, R., & Nelson, C. (2009). Understanding the offshore flood basalt sequence using onshore volcanic facies analogues: An example from the Faroe-Shetland basin. *Geological Magazine*, *146*. https://doi.org/10.1017/S0016756809005974

Jones, A. P., Price, G. D., Price, N. J., DeCarli, P. S., & Clegg, R. A. (2002). Impact induced melting and the development of large igneous provinces. *Earth and Planetary Science Letters*, *202*(3), 551-561. https://doi.org/https://doi.org/10.1016/S0012-821X(02)00824-5

Jones, M. T., Jerram, D. A., Svensen, H. H., & Grove, C. (2016). The effects of large igneous provinces on the global carbon and sulphur cycles. *Palaeogeography, Palaeoclimatology, Palaeoecology*, *441*, 4-21. https://doi.org/https://doi.org/10.1016/j.palaeo.2015.06.042

Kelemen, P., Benson, S. M., Pilorgé, H., Psarras, P., & Wilcox, J. (2019). An Overview of the Status and Challenges of CO2 Storage in Minerals and Geological Formations [Review]. *Frontiers in Climate*, *1*. https://doi.org/10.3389/fclim.2019.00009

Kilhams, B., Chedburn, L., Schofield, N., Lunde, I. L., Romain, H., Jolley, D., & Eide, C. H. (2021). The spatial distribution of igneous centres along the Norwegian Atlantic Margin (Møre and Vøring) and their relationship to magmatic plumbing systems. *Journal of the Geological Society*, *178*(5), jgs2020-2192. https://doi.org/doi:10.1144/jgs2020-192

Kirkpatrick, S. (1973). Percolation and Conduction. *Reviews of Modern Physics*, *45*, 574-588.

Kravchinsky, V. A. (2012). Paleozoic large igneous provinces of Northern Eurasia: Correlation with mass extinction events. *Global and Planetary Change*, *86-87*, 31-36. https://doi.org/https://doi.org/10.1016/j.gloplacha.2012.01.007

Larsen, L. M., & Pedersen, A. K. (1990). Volcanic marker horizons in the Maligât Formation on Disko and Nûgssuaq, and implications for the development of the southern part of the West Greenland basin in the early Tertiary. *Rapport Grønlands Geologiske Undersøgelse*, *148*, 65-73. https://doi.org/10.34194/rapggu.v148.8122

Lebedeva-Ivanova, N., Planke, S., Millett, J. M., Bünz, S., Binde, C. M., Manton, B., Zastrozhnov, D., Berndt, C., Jolley, D. W., and Brinkhuis, H.: Terrestrial Early Eocene Volcanic Paleoenvironment of the Skoll High, Mid-Norwegian Margin, Based on New High-Resolution 3D Seismic Geomorphology, EGU General Assembly 2023, Vienna, Austria, 24–28 Apr 2023, EGU23-17396, https://doi.org/10.5194/egusphere-egu23-17396, 2023.

Liu, J., Xia, Q.-K., Kuritani, T., Hanski, E., & Yu, H.-R. (2017). Mantle hydration and the role of water in the generation of large igneous provinces. *Nature Communications*, *8*(1), 1824. https://doi.org/10.1038/s41467-017-01940-3

Lu, G., & Huismans, R. (2021). Melt volume at Atlantic volcanic rifted margins controlled by depth-dependent extension and mantle temperature. *Nature Communications*, *12*. https://doi.org/10.1038/s41467-021-23981-5

Maharjan, D., Planke, S., Bellwald, B., Millett, J. M., Abdelmalak, M. M., Manton, B., Zastrozhnov, D., Jerram, D. A., & Myklebust, R. (2024). Rapid loading and deformation of soft sediments during emplacement of a lava delta in the Vøring Basin, Mid-Norwegian Margin. *Geological Society, London, Special Publications*, *547*(1), SP547-2023-2043. https://doi.org/doi:10.1144/SP547-2023-43

Matter, J., Stute, M., Snæbjörnsdóttir, S. Ó., Oelkers, E., Gislason, S., Aradottir, E., Sigfusson, B., Gunnarsson, I., Sigurdardottir, H., Gunnlaugsson, E., Axelsson, G., Alfredsson, H., Wolff-Boenisch, D., Mesfin, K., F. Reguera, D., Hall, J., Dideriksen, K., & Broecker, W. (2016). Rapid carbon mineralization for permanent disposal of anthropogenic carbon dioxide emissions. *Science*, *352*. https://doi.org/10.1126/science.aad8132

Matter, J. M., Broecker, W. S., Gislason, S. R., Gunnlaugsson, E., Oelkers, E. H., Stute, M., Sigurdardóttir, H., Stefansson, A., Alfreðsson, H. A., Aradóttir, E. S., Axelsson, G., Sigfússon, B.,

& Wolff-Boenisch, D. (2011). The CarbFix Pilot Project–Storing carbon dioxide in basalt. *Energy Procedia*, *4*, 5579-5585. https://doi.org/https://doi.org/10.1016/j.egypro.2011.02.546

Mavko, G., & Nur, A. (1997). The effect of a percolation threshold in the Kozeny-Carman relation. *Geophysics*, *62*(5), 1480-1482. https://doi.org/10.1190/1.1444251

McDermott, C., Lonergan, L., Collier, J. S., McDermott, K. G., & Bellingham, P. (2018). Characterization of Seaward-Dipping Reflectors Along the South American Atlantic Margin and Implications for Continental Breakup. *Tectonics*, *37*(9), 3303-3327. https://doi.org/https://doi.org/10.1029/2017TC004923

McGrail, B. P., Schaef, H. T., Ho, A. M., Chien, Y.-J., Dooley, J. J., & Davidson, C. L. (2006). Potential for carbon dioxide sequestration in flood basalts. *Journal of Geophysical Research: Solid Earth*, *111*(B12). https://doi.org/https://doi.org/10.1029/2005JB004169

McGrail, B. P., Spane, F. A., Sullivan, E. C., Bacon, D. H., & Hund, G. (2011). The Wallula basalt sequestration pilot project. *Energy Procedia*, *4*, 5653-5660. https://doi.org/https://doi.org/10.1016/j.egypro.2011.02.557

Millett, J. M., Hole, M. J., Jolley, D. W., Schofield, N., & Campbell, E. (2016). Frontier exploration and the North Atlantic Igneous Province: new insights from a 2.6 km offshore volcanic sequence in the NE Faroe–Shetland Basin. *Journal of the Geological Society*, *173*(2), 320-336. https://doi.org/doi:10.1144/jgs2015-069

Millett, J. M., Jerram, D. A., Manton, B., Planke, S., Ablard, P., Wallis, D., Hole, M. J., Brandsen, H., Jolley, D. W., & Dennehy, C. (2021). The Rosebank Field, NE Atlantic: Volcanic characterisation of an inter-lava hydrocarbon discovery. *Basin Research*, *33*(6), 2883-2913. https://doi.org/https://doi.org/10.1111/bre.12585

Millett, J. M., Manton, B. M., Zastrozhnov, D., Planke, S., Maharjan, D., Bellwald, B., Gernigon, L., Faleide, J. I., Jolley, D. W., Walker, F., Abdelmalak, M. M., Jerram, D. A., Myklebust, R., Kjølhamar, B. E., Halliday, J., & Birch-Hawkins, A. (2022). Basin structure and prospectivity of the NE Atlantic volcanic rifted margin: cross-border examples from the Faroe–Shetland, Møre and Southern Vøring basins. In D. Chiarella, S. G. Archer, J. A. Howell, C. A. L. Jackson, H. Kombrink, & S. Patruno (Eds.), *Cross-Border Themes in Petroleum Geology II: Atlantic Margin and Barents Sea* (pp. 0). Geological Society of London. https://doi.org/10.1144/sp495-2019-12

Millett, J. M., Rossetti, L., Bischoff, A., Rossetti, M., Rosenqvist, M. P., Avseth, P., Hole, M. J., Pierdominici, S., Healy, D., Jerram, D. A., & Planke, S. (2024). Lava flow-hosted reservoirs: a review. *Geological Society, London, Special Publications*, *547*(1), SP547-2023-2102. https://doi.org/doi:10.1144/SP547-2023-102

Mjelde, R., Shimamura, H., Kanazawa, T., Kodaira, S., Raum, T., & Shiobara, H. (2003). Crustal lineaments, distribution of lower crustal intrusives and structural evolution of the Vøring Margin, NE Atlantic; new insight from wide-angle seismic models. *Tectonophysics*, *369*(3), 199-218. https://doi.org/https://doi.org/10.1016/S0040-1951(03)00199-9

Morgan, R., & Watts, A. (2018). Seismic and gravity constraints on flexural models for the origin of seaward dipping reflectors. *Geophysical Journal International*, *214*(3), 2073-2083. https://doi.org/10.1093/gji/ggy243

Mutter, J. C., Buck, W. R., & Zehnder, C. M. (1988). Convective partial melting: 1. A model for the formation of thick basaltic sequences during the initiation of spreading. *Journal of Geophysical Research: Solid Earth*, *93*(B2), 1031-1048. https://doi.org/https://doi.org/10.1029/JB093iB02p01031

Mutter, J. C., Talwani, M., & Stoffa, P. L. (1982). Origin of seaward-dipping reflectors in oceanic crust off the Norwegian margin by "subaerial sea-floor spreading". *Geology*, *10*(7), 353-357. https://doi.org/10.1130/0091-7613(1982)10<353:Oosrio>2.0.Co;2

Neal, C., & Anderson, K. (2020). *Preliminary analyses of volcanic hazards at Kīlauea Volcano, Hawai'i, 2017–2018*. U.S. Geological Survey Open File Report. https://doi.org/10.3133/ofr20201002

Nelson, C. E., Jerram, D. A., & Hobbs, R. W. (2009a). Flood basalt facies from borehole data: implications for prospectivity and volcanology in volcanic rifted margins. *Petroleum Geoscience*, *15*(4), 313-324. https://doi.org/doi:10.1144/1354-079309-842

Nelson, C., Jerram, D., Single, R., & Hobbs, R. W. (2009b). Understanding the facies architecture of flood basalts and volcanic rifted margins and its effect on geophysical properties. *Faroe Islands Exploration Conference: Proceedings of the 2nd Conference, Annales Societatis Scientarium Faroensis, supplementum*, 83-103.

Németh, K., & Moufti, M. R. (2023). Lava Flow Hazard and Its Implication in Geopark Development for the Active Harrat Khaybar Intracontinental Monogenetic Volcanic Field, Saudi Arabia. *Land*, *12*(3), 705. https://www.mdpi.com/2073-445X/12/3/705

Noguchi, R., Höskuldsson, Á., & Kurita, K. (2016). Detailed topographical, distributional, and material analyses of rootless cones in Myvatn, Iceland. *Journal of Volcanology and Geothermal Research*, *318*, 89-102. https://doi.org/https://doi.org/10.1016/j.jvolgeores.2016.03.020

Oelkers, E. H., Gislason, S. R., & Matter, J. (2008). Mineral Carbonation of CO2. *Elements*, *4*(5), 333-337. https://doi.org/10.2113/gselements.4.5.333

Ottesen, D., Rise, L., Andersen, Bugge, T., & Eidvin, T. (2009). Geological evolution of the Norwegian continental shelf between 61°N and 68°N during the last 3 million years. *Norwegian Journal of Geology*, *89*, 251-265.

Paton, D., Pindell, J., McDermott, K., Bellingham, P., & Horn, B. (2017). Evolution of seaward-dipping reflectors at the onset of oceanic crust formation at volcanic passive margins: Insights from the South Atlantic. *Geology*, *45*. https://doi.org/10.1130/G38706.1

Peron-Pinvidic, G., & Osmundsen, P. T. (2018). The Mid Norwegian - NE Greenland conjugate margins: Rifting evolution, margin segmentation, and breakup. *Marine and Petroleum Geology*, *98*, 162-184. https://doi.org/https://doi.org/10.1016/j.marpetgeo.2018.08.011

Planke, S. (1994). Geophysical response of flood basalts from analysis of wire line logs: Ocean Drilling Program Site 642, Vøring volcanic margin. *Journal of Geophysical Research: Solid Earth*, *99*(B5), 9279-9296. https://doi.org/https://doi.org/10.1029/94JB00496

Planke, S., Symonds, P., Alvestad, E., & Skogseid, J. (2000). Seismic volcano-stratigraphy of large-volume basalt extrusive complexes on rifted margins. *Journal of Geophysical Research*, *105*, 19335-19352. https://doi.org/10.1029/1999JB900005

Planke, S., Rasmussen, T., Rey, S., & Myklebust, R. (2005). Seismic characteristics and distribution of volcanic intrusions and hydrothermal complexes in the Vøring and Møre Basins. *Petroleum Geology of Northwest Europe: Proceedings of the Conference*, *6*. https://doi.org/10.1144/0060833

Planke, S., Millett, J. M., Maharjan, D., Jerram, D. A., Abdelmalak, M. M., Groth, A., Hoffmann, J., Berndt, C., & Myklebust, R. (2017). Igneous seismic geomorphology of buried lava fields and coastal escarpments on the Vøring volcanic rifted margin. *Interpretation*, *5*(3), SK161-SK177. https://doi.org/10.1190/int-2016-0164.1

Planke, S., Berndt, C., Alvarez Zarikian, C.A., and the Expedition 396 Scientists, (2021a). *Expedition 396 Preliminary Report: Mid-Norwegian Continental Margin Magmatism*. International Ocean Discovery Program. https://doi.org/10.14379/iodp.pr.396.2022

Planke, S., Berndt, C., and Alvarez Zarikian, C.A., (2021b). Expedition 396 Scientific Prospectus: Mid-Norwegian Continental Margin Magmatism. International Ocean Discovery Program. https://doi.org/10.14379/iodp.sp.396.2021

Planke, S., Bellwald, B., Millett, J., Planke, E. E. E., Zastrozhnov, D., Carlevaris, P., Rosenqvist, M., Jerram, D., Schmid, D. W., Berndt, C., Kjølhamar, B., & Myklebust, R. (2021c). *Permanent Carbon Sequestration Potential in Offshore Basalt Sequences on the NW European Continental Margins*

Planke, S., Berndt, C., Alvarez Zarikian, C.A., Agarwal, A., Andrews, G.D.M., Betlem, P., Bhattacharya, J., Brinkhuis, H., Chatterjee, S., Christopoulou, M., Clementi, V.J., Ferré, E.C., Filina, I.Y., Frieling, J., Guo, P., Harper, D.T., Jones, M.T., Lambart, S., Longman, J., Millett, J.M., Mohn, G., Nakaoka, R., Scherer, R.P., Tegner, C., Varela, N., Wang, M., Xu, W., and Yager, S.L., (2023a). Sites U1571 and U1572. In Planke, S., Berndt, C., Alvarez Zarikian, C.A., and the Expedition 396 Scientists, Mid-Norwegian Margin Magmatism and Paleoclimate Implications. Proceedings of the International Ocean Discovery Program, 396: College Station, TX (International Ocean Discovery Program). https://doi.org/10.14379/iodp.proc.396.107.2023

Planke, S., Lebedova-Ivanova, S., Bunz, S., Binde, C., Berndt, C., Faleide, J. I., Huismans, R., Zastrozhnov, D., Manton, B., Stokke, H., Betlem, P., Millet, J. (2023b). High Resolution core-log-seismic inregration and igneous seismic geomorphology of IODP Expedition 396 sites on the mid-Norwegian margin. *Near Surface Geoscience'23, Conference and Exhibition*.

Poland, M. P., & Orr, T. R. (2014). Identifying hazards associated with lava deltas. *Bulletin of Volcanology*, *76*(12), 880. https://doi.org/10.1007/s00445-014-0880-0

Raza, A., Glatz, G., Gholami, R., Mahmoud, M., & Alafnan, S. (2022). Carbon mineralization and geological storage of CO2 in basalt: Mechanisms and technical challenges. *Earth-Science Reviews*, *229*, 104036. https://doi.org/https://doi.org/10.1016/j.earscirev.2022.104036

Ren, S., Faleide, J. I., Eldholm, O., Skogseid, J., & Gradstein, F. (2003). Late Cretaceous–Paleocene tectonic development of the NW Vøring Basin. *Marine and Petroleum Geology*, *20*(2), 177-206. https://doi.org/https://doi.org/10.1016/S0264-8172(03)00005-9

Ren, S., Skogseid, J., & Eldholm, O. (1998). Late Cretaceous-Paleocene extension on the Vøring Volcanic Margin. *Marine Geophysical Researches*, *20*(4), 343-369. https://doi.org/10.1023/A:1004554217069

Reynolds, P., Brown, R., Thordarson, T., Llewellin, E., & Fielding, K. (2015). Rootless cone eruption processes informed by dissected tephra deposits and conduits. *Bulletin of Volcanology*, *77*, 1-17. https://doi.org/10.1007/s00445-015-0958-3

Rider, M. H. (1996). *The Geological Interpretation of Well Logs*. Whittles Publishing. 42-131. https://books.google.no/books?id=mt2UAAAACAAJ

Rintoul, M. D., & Torquato, S. (1997). Reconstruction of the Structure of Dispersions. *Journal of Colloid and Interface Science*, *186*(2), 467-476. https://doi.org/https://doi.org/10.1006/jcis.1996.4675

Rise, L., Chand, S., Hjelstuen, B. O., Haflidason, H., & Bøe, R. (2010). Late Cenozoic geological development of the south Vøring margin, mid-Norway. *Marine and Petroleum Geology*, *27*(9), 1789-1803. https://doi.org/https://doi.org/10.1016/j.marpetgeo.2010.09.001

Roberts, G., Crawford, I., Peacock, D., Vetterlein, J., Parfitt, E., & Bishop, L. (2007). Possible evidence for on-going volcanism on Mars as suggested by thin, elliptical sheets of low-albedo particulate material around pits and fissures close to Cerberus Fossae. *Earth, Moon and Planets*, *101*, 1-16. https://doi.org/10.1007/s11038-007-9140-z

Rosenqvist, M. P., Meakins, M. W. J., Planke, S., Millett, J. M., Kjøll, H. J., Voigt, M. J., & Jamtveit, B. (2023). Reservoir properties and reactivity of the Faroe Islands Basalt Group: Investigating the potential for CO2 storage in the North Atlantic Igneous Province. *International Journal of Greenhouse Gas Control*, *123*, 103838. https://doi.org/https://doi.org/10.1016/j.ijggc.2023.103838

Rosenqvist, M. P., Millett, J. M., Planke, S., Johannesen, R. M., Passey, S. R., Sørensen, E. V., Vosgerau, H., & Jamtveit, B. (2024). The architecture of basalt reservoirs in the North Atlantic Igneous Province with implications for basalt carbon sequestration. *Geological Society, London, Special Publications*, *547*(1), SP547-2023-2096. https://doi.org/doi:10.1144/SP547-2023-96

Saunders, A. D. (2005). Large Igneous Provinces: Origin and Environmental Consequences. *Elements*, *1*(5), 259-263. https://doi.org/10.2113/gselements.1.5.259

Sheriff, R., & Geldart, L. (1996). Exploration Seismology. In (Vol. 18). https://doi.org/10.1017/CBO9781139168359

Single, R., & Jerram, D. (2004). The 3D facies architecture of flood basalt provinces and their internal heterogeneity: Examples from the Palaeogene Skye Lava Field. *Journal of The Geological Society - J GEOL SOC*, *161*, 911-926. https://doi.org/10.1144/0016-764903-136

Skilling, I. (2002). Basaltic pahoehoe lava-fed deltas: Large-scale characteristics, clast generation, emplacement processes and environmental discrimination. *Geological Society, London, Special Publications*, *202*, 91-113. https://doi.org/10.1144/GSL.SP.2002.202.01.06

Skogseid, J., Pedersen, T., Eldholm, O., & Larsen, B. T. (1992). Tectonism and magmatism during NE Atlantic continental break-up: the Vøring Margin. *Geological Society, London, Special Publications*, *68*(1), 305-320. https://doi.org/doi:10.1144/GSL.SP.1992.068.01.19

Smellie, J., Wilch, T., & Rocchi, S. (2013). ʻAʻa¯ lava-fed deltas: A new reference tool in paleoenvironmental studies. *Geology*, *41*, 403-406. https://doi.org/10.1130/G33631.1

Snæbjörnsdóttir, S. Ó., Wiese, F., Fridriksson, T., Ármansson, H., Einarsson, G. M., & Gislason, S. R. (2014). CO2 storage potential of basaltic rocks in Iceland and the oceanic ridges. *Energy Procedia*, *63*, 4585-4600. https://doi.org/https://doi.org/10.1016/j.egypro.2014.11.491

Soule, S. A., Zoeller, M., & Parcheta, C. (2021). Submarine lava deltas of the 2018 eruption of Kīlauea volcano. *Bulletin of Volcanology*, *83*(4), 23. https://doi.org/10.1007/s00445-020-01424-1

Storey, B., Vaughan, A., & Riley, T. (2013). The links between large igneous provinces, continental break-up and environmental change: Evidence reviewed from Antarctica. *Earth and Environmental Science Transactions of the Royal Society of Edinburgh*, *104*. https://doi.org/10.1017/S175569101300011X

Sun, L., Liu, Y., Cheng, Z., Jiang, L., Lv, P., & Song, Y. (2023). Review on Multiscale CO2 Mineralization and Geological Storage: Mechanisms, Characterization, Modeling, Applications and Perspectives. *Energy \& Fuels*, *37*(19), 14512-14537. https://doi.org/10.1021/acs.energyfuels.3c01830

Svensen, H. H., Jerram, D. A., Polozov, A. G., Planke, S., Neal, C. R., Augland, L. E., & Emeleus, H. C. (2019). Thinking about LIPs: A brief history of ideas in Large igneous province research. *Tectonophysics*, *760*, 229-251. https://doi.org/https://doi.org/10.1016/j.tecto.2018.12.008

Walker, F., Schofield, N., Millett, J., Jolley, D., Hole, M., & Stewart, M. (2022). Paleogene volcanic rocks in the northern Faroe–Shetland Basin and Møre Marginal High: understanding lava field stratigraphy. *Geological Society, London, Special Publications*, *495*(1), 199-235. https://doi.org/doi:10.1144/SP495-2019-13

Walker, G. P. L. (1971). Compound and simple lava flows and flood basalts. *Bulletin Volcanologique*, *35*(3), 579-590. https://doi.org/10.1007/BF02596829

Walker, G. P. L. (1991). Structure, and origin by injection of lava under surface crust, of tumuli, "lava rises", "lava-rise pits", and "lava-inflation clefts" in Hawaii. *Bulletin of Volcanology*, *53*(7), 546-558. https://doi.org/10.1007/BF00298155

Wright, K. A., Davies, R. J., Jerram, D. A., Morris, J., & Fletcher, R. (2012). Application of seismic and sequence stratigraphic concepts to a lava-fed delta system in the Faroe-Shetland Basin, UK and Faroes. *Basin Research*, *24*(1), 91-106. https://doi.org/https://doi.org/10.1111/j.1365-2117.2011.00513.x

Yang, J., Cawood, P. A., Montañez, I. P., Condon, D. J., Du, Y., Yan, J.-X., Yan, S., & Yuan, D. (2020). Enhanced continental weathering and large igneous province induced climate warming at the Permo-Carboniferous transition. *Earth and Planetary Science Letters*, *534*, 116074. https://doi.org/https://doi.org/10.1016/j.epsl.2020.116074

Zastrozhnov, D., Gernigon, L., Gogin, I., Abdelmalak, M. M., Planke, S., Faleide, J. I., Eide, S., & Myklebust, R. (2018). Cretaceous-Paleocene Evolution and Crustal Structure of the Northern

Vøring Margin (Offshore Mid-Norway): Results from Integrated Geological and Geophysical Study. *Tectonics*, *37*. https://doi.org/10.1002/2017TC004655

Zastrozhnov, D., Gernigon, L., Gogin, I., Planke, S., Abdelmalak, M. M., Polteau, S., Faleide, J. I., Manton, B., & Myklebust, R. (2020). Regional structure and polyphased Cretaceous-Paleocene rift and basin development of the mid-Norwegian volcanic passive margin. *Marine and Petroleum Geology*, *115*, 104269. https://doi.org/https://doi.org/10.1016/j.marpetgeo.2020.104269